A high-resolution physical-biogeochemical model for marine resource applications in the Northern Indian Ocean (MOM6-COBALT-IND12 v1.0)

Enhui Liao[1], Laure Resplandy[2], Fan Yang[2], Yangyang Zhao[2], Sam Ditkovsky[3], Manon Malsang[4], Jenna Pearson[5], Andrew C. Ross[6], Robert Hallberg[6], and Charles Stock[6]

[1]School of Oceanography, Shanghai Jiao Tong University, Shanghai, China
[2]Department of Geosciences and High Meadows Environmental Institute, Princeton University, Princeton, NJ, USA
[3]Program in Atmospheric and Oceanic Sciences, Sayre Hall, Princeton University, Princeton, NJ, USA
[4]Laboratoire d'Océanographie et du Climat Expérimentations et Approches Numériques (LOCEAN), Institut Pierre-Simon Laplace (IPSL), Sorbonne Université, Paris, France
[5]Climatematch Academy, Neuromatch Inc., USA
[6]NOAA OAR Geophysical Fluid Dynamics Laboratory, Princeton, NJ, USA

Correspondence: Laure Resplandy (laurer@princeton.edu); Enhui Liao (ehliao@sjtu.edu.cn)

Abstract. We introduce and evaluate the regional ocean model MOM6-COBALT-IND12 version 1 coupling the MOM6 ocean dynamics model to the Carbon, Ocean Biogeochemistry and Lower Trophics (COBALT) biogeochemical model at a horizontal resolution of 1/12°. The model covers the northern Indian Ocean (~~north of 8~~from 8.6°S to the northern continental boundaries), central to the livelihoods and economies of countries that comprise about one-third of the world's population. We demonstrate that the model effectively captures the key physical and biogeochemical basin-scale features related to seasonal monsoon reversal, interannual Indian Ocean Dipole and multi-decadal variability, as well as intraseasonal and fine-scale variability (e.g., eddies and planetary waves), which are all essential for accurately simulating patterns of coastal upwelling, primary productivity, temperature, salinity, and oxygen levels. Well represented features include the timing and amplitude of the monsoonal blooms triggered by summer coastal upwelling and winter mixing, the strong contrast between the high evaporation / high salinity Arabian Sea and high precipitation / high runoff / low salinity Bay of Bengal, the seasonality of the Great Whirl gyre and coastal Kelvin upwelling/downwelling waves, as well as the physical and biogeochemical patterns associated with intraseasonal and interannual variability. Quantitatively, the model exhibits relatively small biases, as reflected by root mean square error (RMSE) values in key variables: sea surface temperature (0.25–0.3 °C), mixed layer depth (7–8.09 m), sea level anomaly (0.02 m), sea surface salinity (0.53-0.71 psu), vertical chlorophyll (0.03-0.3 mg m^{-3}), subsurface temperature (0.33 °C), and subsurface salinity (0.07 psu). A major model bias (16 μmol kg^{-1} of oxygen) is the larger oxygen minimum zone simulated in the Bay of Bengal, a common challenge of ocean and Earth system models in this region. This bias was partly mitigated by improving the representation of the export and burial of organic detritus to the deep ocean (e.g., sinking speed, riverine lithogenic material inputs that protect organic material and burial fraction), and water-column denitrification (e.g., nitrate-based respiration at higher oxygen levels) using observational constraints. These results indicate that the regional

MOM6-COBALT-IND12 v1.0 model is well suited for physical and biogeochemical studies on timescales ranging from weeks to decades, in addition to supporting marine resource applications and management in the northern Indian Ocean.

1 Introduction

The northern Indian Ocean (from 8.6°S to the northern continental boundaries and 32°E to 114°E) is central to the livelihood and economy of about one third of the Earth's population which ~~live~~ lives in its littoral countries (e.g., India, Indonesia, Pakistan, ~~Bengladesh~~Bangladesh, Tanzania, Myanmar, Malaysia, Kenya, and Yemen) and provides valuable resources via the "blue economy"~~(e.g., fishery, aquaculture, marine tourism, Roy, 2019)~~, such as fishery, aquaculture, and marine tourism (Roy, 2019). A major challenge to understand and anticipate the response of Indian Ocean ecosystems is to account for the full range of spatio-temporal variability and human-driven changes that control the climatic and environmental conditions defining the habitat, success and survival of these ecosystems (Phillips et al., 2021; Pinsky et al., 2013; Deutsch et al., 2015). On seasonal and interannual time-scales, the Indian monsoon and the Indian Ocean Dipole (IOD) control the ocean circulation and regulate temperature (Schott and McCreary, 2001; Saji et al., 1999; Beal et al., 2013), oxygen levels (Resplandy et al., 2012; Vallivattathillam et al., 2017; Pearson et al., 2022; Al Azhar et al., 2017) and primary productivity (Barber et al., 2001; Gauns et al., 2005; Prakash and Ramesh, 2007; Lévy et al., 2007; Kumar et al., 2010; Wiggert et al., 2009; Resplandy et al., 2011; Currie et al., 2013; Sarma and Dalabehera, 2019), with implications ~~on~~ for the spatial and temporal distribution of species that are commercially valuable such as tuna, and key to local food security such as small pelagic ~~fishes~~ fish (e.g., Jebri et al., 2020; Wang et al., 2023).

On decadal and multi-decadal timescales, the Indian Ocean has undergone rapid warming, with an increase in sea surface temperature ~~that increased~~ (SST) by about 1°C since the 1950s (Roxy et al., 2020), a decline in primary productivity (Sunanda et al., 2023; Sridevi et al., 2023; Gregg and Rousseaux, 2019; Dalpadado et al., 2021), and a significant loss in oxygen in the Arabian Sea and Bay of Bengal (Banse et al., 2014; Piontkovski and Al-Oufi, 2015; Queste et al., 2018; Rixen et al., 2019a; Naqvi, 2019; Löscher, 2021; Lachkar et al., 2023) as well as in the water masses supplying oxygen to the Indian Ocean (Helm et al., 2011; Ito et al., 2017; Naqvi, 2021; Ditkovsky et al., 2023). Warming, decline in primary productivity, and oxygen loss are projected to continue in the Indian Ocean unless greenhouse gas emissions are rapidly curtailed (Bopp et al., 2013; Kwiatkowski et al., 2017, 2020; Roxy et al., 2020; Lachkar et al., 2018, 2019; Lévy et al., 2022; Ditkovsky et al., 2023; Sharma et al., 2023). Warming is also expected to weaken the monsoon despite a potential increase in extreme rainfall events (e.g., Sooraj et al., 2015; Singh et al., 2019; Roxy et al., 2020). This could modify the supply of ~~fresh water~~ freshwater and nutrients to coastal waters, and increase the frequency of extreme positive IOD events (Roxy et al., 2020; Cai et al., 2021), which are known to induce weather extremes (Cai et al., 2021), promote primary productivity in the eastern tropical Indian Ocean (e.g., Wiggert et al., 2009; Currie et al., 2013) and lead to low coastal oxygen levels (coastal hypoxia) in the eastern Bay of Bengal (Pearson et al., 2022). Projections from Coupled Model Intercomparison Project (CMIP) models suggest substantial shifts in net primary production and sharp declines in pH in the coming decades, highlighting the northern Indian Ocean's particular vulnerability to climate change (Sunanda et al., 2021, 2023). Observations indicate that these changes have already impacted ecosystems

in the Indian Ocean. For instance, do Rosário Gomes et al. (2008) found that the dominant phytoplankton group during the winter bloom in the Arabian Sea shifted from diatom to dinoflagellate in recent decades in response to warming and oxygen loss, with potentially large implications for the functioning of this ecosystem. In coastal areas, the effect of natural variability associated with the seasonal monsoon and interannual IOD combines with global warming and anthropogenic activities (waste waters, urbanization, fertilizers etc.) leading to coastal hypoxic events and in extreme cases to massive mortality events with implications for coastal fisheries and aquaculture (low oxygen levels, Naqvi et al., 2009; Naqvi, 2021, 2022; Pearson et al., 2022).

Models are ~~a powerful tool to explore~~ powerful tools for exploring the Indian Ocean's response to climate variability and anthropogenic changes, ~~identify~~ identifying the processes at play, and ~~assess~~ assessing the impacts on biogeochemistry and ecosystems ~~(e.g., Sengupta et al., 2001; Rahaman et al., 2014; Lachkar et al., 2018, 2019; Resplandy et al., 2011, 2012; Schmidt et al., 20~~(e.g., Sengupta et al., 2001; Rahaman et al., 2014; Lachkar et al., 2018, 2019; Resplandy et al., 2011, 2012; Schmidt et al., 2021; Ditkovsk. Yet, global ocean and Earth system models are plagued by strong biases in the circulation and biogeochemical dynamics in the Indian Ocean (Séférian et al., 2020; Rixen et al., 2020; Li et al., 2016). In particular, global models tend to misrepresent the circulation that regulates the exchanges between the Indian Ocean and the Pacific Ocean (i.e., the Indonesian throughflow), the overflows from marginal seas ~~(Red Sea and Persian Gulf, Lachkar et al., 2019; Schmidt et al., 2021; Ditkovsky et al., 2023)~~(Red Sea and P, as well as the mesoscale features (eddies and filaments) key to the ocean circulation, biological production, and the supply of nutrients and oxygen in the Indian Ocean (e.g., Wirth et al., 2002; Resplandy et al., 2011, 2012; Nuncio and Kumar, 2012; Vic et al., 2014; Lachkar et al., 2016; Greaser et al., 2020; Vinayachandran et al., 2021). These shortcomings of global models strongly limit our ability to evaluate the biogeochemical and ecosystem response to climate variability and change. It is with these applications in mind that we ~~developed~~ configured, customised and validated the regional Indian Ocean simulation ~~presented here~~ based on the Modular Ocean Model 6 (MOM6, Adcroft et al., 2019) coupled with the Carbon, Ocean, Biogeochemistry, and Lower Trophics module version 2.0 (COBALTv2, Stock et al., 2014, 2020). The model configuration, called MOM6-COBALT-IND12 version 1 (or MOM6-COBALT-IND12 v1.0), covers the northern Indian Ocean at a horizontal resolution of 1/12° and is designed for ~~physical, biogeochemical~~ physical-biogeochemical studies as well as applications to ecosystems, marine resources and management (Figure 1).

In the following sections, we first present the model physical and biogeochemical configuration (section 2) and the data and metrics used to assess the model (section 3). We then evaluate key monsoon-driven seasonal patterns (section 4), ocean interior ventilation and oxygen minimum zones (OMZs) distribution (section 5), as well as intraseasonal and interannual variability (sections 6 and 7) simulated in the model. Finally, we discuss the main strengths and limitations of the model configuration (section 8).

2 Regional Indian Ocean configuration

In this section, we describe the regional model configuration MOM6-COBALT-IND12 v1.0 (called MOM6-COBALT-IND12 in the following), which couples an ~~ocean physical~~ physical ocean model with a biogeochemical module.

2.1 Physical ocean model configuration

The Indian Ocean regional model is based on the Geophysical Fluid Dynamics Laboratory (GFDL) ocean-ice model ~~Modular Ocean Model 6 (MOM6, Adcroft et al., 2019)~~MOM6 (Adcroft et al., 2019). In the horizontal, the model uses an Arakawa ~~C grid~~ C-grid (Arakawa and Lamb, 1977). The regional configuration MOM6-COBALT-IND12 covers the Arabian Sea and Bay of Bengal and extends to the equatorial Indian Ocean ending south of Java with one open boundary (32°E to 114°E and 8.6°S to 30.3°N~~,~~; Figure 1). The horizontal resolution is 1/12° (~~486 by 984~~ 486×984 tracer points on the horizontal), with the horizontal grid spacing varying from 9.2 km at the equator to 7.3 km at 30°N. This resolution resolves the first baroclinic radius of deformation with at least 2 grid points and is smaller than the third baroclinic radius of deformation (~~$R_3 =$~~ $R_3 \geq$ 13 km) everywhere in the domain except in the Persian Gulf and on the coastal shelf along the eastern Arabian Sea (Chelton et al., 1998; Hallberg, 2013). MOM6-COBALT-IND12 is therefore considered an 'eddy resolving' model for the region with a rectilinear and orthogonal grid (32°E to 114°E and 8.6°S to 30.3°N).

~~On~~ In the vertical, the model includes ~~75~~ a 75-layer hybrid z*-isopycnal coordinate system with a z* ~~coordinate~~ layers near the surface (about 2 m thick in the upper 20 m in the tropical Indian Ocean) and ~~a~~ modified potential density ~~coordinate below (identical to the hybrid z*-isopycnal developped in Adcroft et al., 2019, see Figure 2)~~layers below (identical to the hybrid z*-isopycnal co . The model bathymetry was generated using the General Bathymetric Chart of the Oceans version 2020 ~~(2020, 2020)~~ (GEBCO; Weatherall et al., 2015) by averaging the GEBCO bathymetry (provided at a resolution of 15 ~~arc-second intervals in~~ arcsec) over each grid cell. The depths of the channel connecting the Red Sea bottom waters and the Arabian Sea (region in 12.5-14.2°N, 42.375-43.375°E) are set to 220 m to allow the outflow. The shallowest bathymetry in the model is 4 m. The model is integrated in time using a split explicit method ~~(Runge-Kutta second order, Hallberg and Adcroft, 2009)~~ (Runge-Kutta second-order scheme; Hallberg and Adcroft, 2009). The baroclinic ~~time step~~ time-step is 600 seconds and the thermodynamic and biogeochemical time-step are ~~set to~~ 1800 seconds (Table 1). Using an 18-node setup with 40 cores per node, which distributes the 486 x 984 model grid across available processing units, the model can run one year of simulation in about 16 hours of wall clock time (this includes the output of extensive diagnostics).

The configuration of subgrid-scale parameterizations used in MOM6-COBALT-IND12 are based on that of the GFDL Ocean Model version 4 ~~(OM4, Adcroft et al., 2019)~~(OM4; Adcroft et al., 2019). We use a background kinematic viscosity and a background diapycnal diffusivity of ~~$1.5 \times 10^{-5}\,\mathrm{m^2 s^{-1}}$~~ $1.5 \times 10^{-5}\,\mathrm{m^2\,s^{-1}}$ (Table 1). As in OM4, viscosity beyond background levels is evaluated as the maximum of a Smagorinsky and resolution-dependent biharmonic viscosity (Griffies and Hallberg, 2000). Additional mixing is represented by planetary boundary layer mixing (Reichl and Hallberg, 2018; Reichl and Li, 2019), shear mixing (Jackson et al., 2008), and mixed-layer restratification due to submesoscale processes (Fox-Kemper et al., 2011). MOM6-COBALT-IND12 also includes bottom boundary layer mixing as in OM4, but the ~~efficiency~~ mixing efficiency parameter of this scheme is lowered from 0.2 in OM4 to 0.01 following Ross et al. (2023). The model explicitly resolves barotropic tidal forcing (see next section) ~~, and only~~ and low-mode internal ~~waves~~ tides are well resolved at 1/12° resolution~~, but~~ ; however, we parameterize the local dissipation of high-mode internal tides according to topographic roughness data (St. Laurent et al., 2002; Polzin, 2009). See Table 1 for a list of configuration parameters.

Table 1. Major parameters and associated values used in the physical ocean (MOM6) component of the model

Parameter	Value	Reference
Vertical coordinate	75 layer hybrid z*-isopycnal	Adcroft et al. (2019)
Baroclinic time step	600 s	
Thermodynamic and BGC time step	1800 s	
Planetary boundary layer parameterization	ePBL	Reichl and Hallberg (2018)
Submesoscale eddy front length	500 m	Fox-Kemper et al. (2011)
Biharmonic viscosity	Maximum of Smagorinsky and	
	resolution-dependent viscosities	Griffies and Hallberg (2000)
Smagorinsky coefficient	0.06	
Resolution-dependent	$0.01\Delta_x^3\,\mathrm{m}^4\mathrm{s}^{-1}$	Adcroft et al. (2019)
Bottom boundary layer mixing efficiency	0.01	Legg et al. (2006)
Background kinematic viscosity	$1.5\times10^{-5}\,\mathrm{m}^2\mathrm{s}^{-1}$	
Background diapycnal diffusivity	$1.5\times10^{-5}\,\mathrm{m}^2\mathrm{s}^{-1}$	
Boundary Conditions		
Sea level and barotropic velocities	Flather scheme	~~Flather R. (1976)~~Flather (1976)
Baroclinic velocities	Radiation scheme and nudging	Orlanski (1976) and
	(3-day inflow and 360-day outflow)	Marchesiello et al. (2001)
Temperature and salinity	Reservoirs with 9 km length scale	Ross et al. (2023)
Biogeochemical tracers	Reservoirs with 9 km outflow length scale	
	and 300 km inflow length scale	
Tidal SAL coefficient	0.094	Irazoqui Apecechea et al. (2017)
		Stepanov and Hughes (2004); Barton et al. (2022)
Opacity Scheme	3-band with chlorophyll	(Manizza, 2005)
Piston velocity for SSS relaxation	0.1667 m d^{-1}	Adcroft et al. (2019)

2.2 Physical ocean model forcing

2.2.1 Initial state, spin-up and atmospheric forcing

The ocean model was ~~run from 1980 to 2020~~ initialized using temperature and salinity from annual mean fields from the World Ocean Atlas version 2013 (WOA13; Locarnini et al., 2014; Zweng et al., 2014). Our simulations were run using the atmospheric forcing from the 1/4° horizontal resolution European Center for Medium-range Weather Forecasts reanalysis 5th generation (ERA5) at 1-hour frequency (Hersbach et al., 2020). ~~Temperature and salinity were initialized from annual mean fields from the World Ocean Atlas version 2013 (WOA13, Locarnini et al., 2014; Zweng et al., 2014)~~In the ocean model,

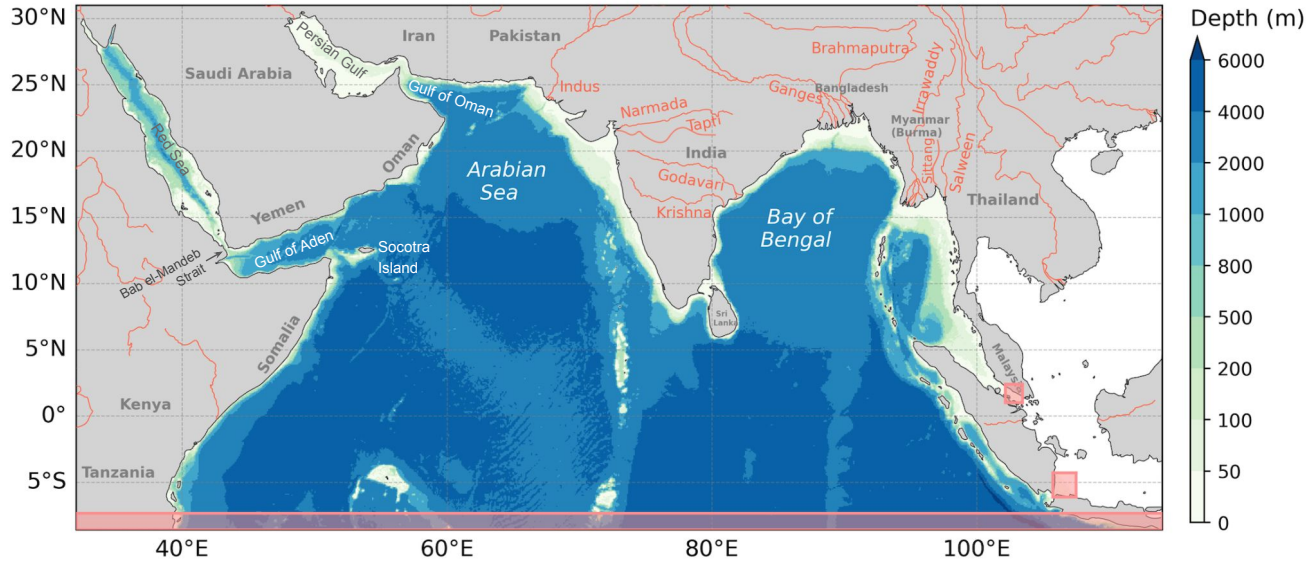

Figure 1. Domain and bathymetry of the regional Indian Ocean MOM6-COBALT-IND12. Pink shading indicates the extent of sponge layers (see ~~methods~~Section 2.2.2). Major rivers are indicated in ~~blue~~red. Socotra Island and the Bab-el-Mandeb Strait are labeled on the map.

air–sea heat fluxes were computed using the bulk algorithm of Large and Yeager (2004), which requires atmospheric input variables referenced at 10 m. As the ERA5 forcing provides near-surface temperature and humidity at 2 m, these variables were vertically adjusted to 10 m following the procedure recommended by Large and Yeager (2004), ensuring consistency with the algorithm's assumptions. The sea surface salinity (SSS) was restored to the polar science center hydrographic climatology (PHC2.1), which is based on the World Ocean Atlas 98 with data replenishment in the Arctic Ocean (Steele et al., 2001), with a piston velocity of 0.1667 m d^{-1}. ~~Our simulations were initialized after~~ We conducted a 32-year spin-up, ~~which was achieved by looping~~ consisting of four consecutive 8-year loops of the 1980 to 1987 forcing field~~. The hindcast simulation was started on January 1 1980, using~~ , and reached a well-equilibrated state with minimal linear trends of physical and biogeochemical variables (e.g., drift in SST, SSS, oxygen, nitrate, primary production and ocean surface partial pressure of carbon dioxide pCO_2 < ~0.1% for spin-up years 17-32). Using outputs from the end of the spinup simulation as initial conditions, the hindcast simulation was started on 1 January 1980 and was run from 1980 to 2020 for our analysis in this study.

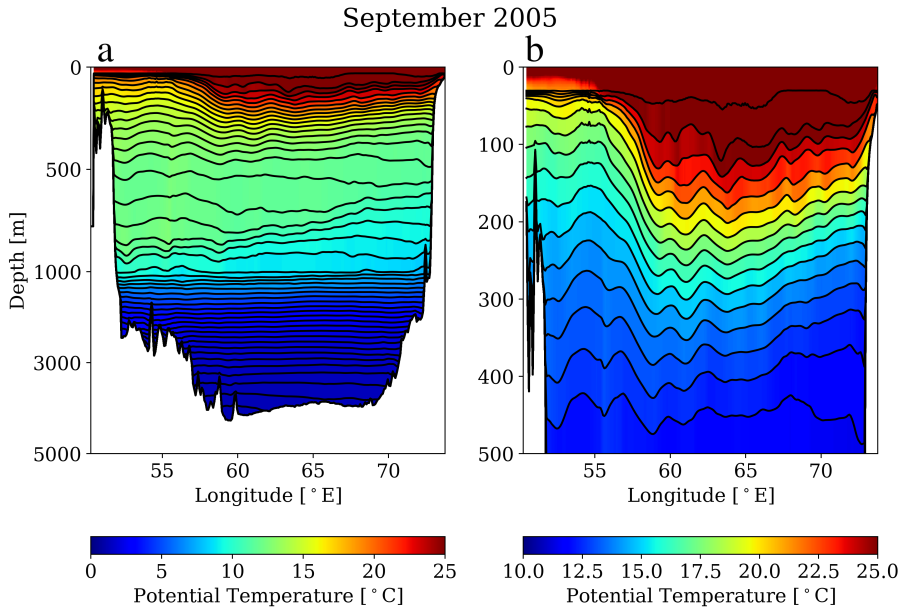

Figure 2. West-east cross-section of the Arabian Sea at 15°N showing the structure of the isopycnal vertical coordinate (contours) overlain with potential temperature (colors) in September 2005 (a) over the full column and (b) over the top 500 m. The z* layers in the upper ocean are not shown. The coordinate follows the pattern of the wind-driven upwelling along the coast of Yemen in the west, and the coastal Kelvin wave-driven upwelling along the ~~India~~ Indian coast in the east.

2.2.2 Open boundary conditions and tidal forcing

Open boundary conditions (OBC) are set using the Flather formulation for the tidal and sub-tidal sea level and barotropic velocity and the Orlanski formulation for the baroclinic velocity ~~(Flather R., 1976; Orlanski, 1976)~~(Flather, 1976; Orlanski, 1976). In addition, we nudge the boundary ~~condition data~~ values towards external forcing with a strong 3-day time-scale for baroclinic normal and tangential velocities entering the model and a weak 360-day time-scale for outgoing velocities (Marchesiello et al., 2001). The ~~OBC~~ boundary value for temperature and salinity are set using a reservoir in which the properties are evolving based on contributions from an inflow (properties outside of the domain set by an ~~OBC~~ boundary forcing file) and outflow (properties simulated inside the model domain) fluxes. Similarly to Ross et al. (2023), the inflow and outflow length scales are set to 9 km (about 1-10 day time-scale for velocities of 10^{-1} cm s^{-1}) for temperature and salinity ~~, i.e.~~(i.e., inflow and outflow have an equal contribution to the ~~OBC reservoir~~boundary reservoir). The model includes a sponge layer over 15 grid points at the southern open boundary, nudging the model to time-varying Ocean Reanalysis System 5 (ORAS5) temperature and salinity with a time-scale increasing from 12 days at the boundary to 174 days at the 15th grid point. The model also includes two sponge layers at the closed boundaries of the Malacca and Sunda Straits with a nudging to the climatological ~~WOA13~~ WOA18 data. For the Malacca Strait, temperature and salinity are nudged over 15 grid points with a ~~time scale~~ time-scale increasing

from 12 days at the strait outlet to 174 days toward the Indian Ocean. In the Sunda Strait, the nudging is over 21 grid points and the ~~time scale~~ time-scale increases from 12 days at the outlet to 336 days toward the Indian Ocean.

Ten tidal components (i.e., M2, S2, N2, K2, K1, O1, P1, Q1, Mm, and Mf) interpolated from the inversion of TOPEX/-POSEIDON crossover data TPX09 (Egbert and Erofeeva, 2002) are used to generate surface elevation and velocity forcing at the open boundary. Tidal potential forcing from the same ten components is included in the barotropic momentum equations throughout the domain, and the effects of self-attraction and loading are represented using the scalar approximation (Accad and Pekeris, 1978) with a coefficient of 0.094. Sub-tidal velocities, temperature and salinity ~~open boundary conditions~~ at the southern open boundary are from ~~monthly Ocean Reanalysis System~~ the monthly ORAS5 (Zuo et al., 2019).

2.2.3 River freshwater discharge

Freshwater discharge from rivers was ~~evaluated from~~ prescribed using the gridded daily Global Flood Awareness System (GloFAS) reanalysis version 4.0, as described by Grimaldi et al. (2022) and Harrigan et al. (2023). To ~~align~~ map the river discharge data ~~with~~ onto the MOM6-COBALT-IND12 grid, we used the GloFAS local drainage direction map to identify outlet points adjacent to the coast, as well as any chains of outlet points connected to these coastal outlets, see details in Burek et al. (2013). The streamflow at these outlet points was introduced at the surface of the nearest model coastal ocean grid cell. To ensure the riverine freshwater flux is mixed into the water column, an extra input of turbulent kinetic energy extending down to a depth of 10 meters was included at the discharge points (Tseng et al., 2016). By comparing GloFAS to published discharge observations (Jian et al., 2009; Siswanto et al., 2023), we found that GloFAS overestimated discharge in the Ganges-Brahmaputra river system, and therefore scaled down the freshwater discharge by 25% to match observations in these two rivers ~~(see Appendix Figure A1)~~(see Appendix Figure A1; Jian et al., 2009; Siswanto et al., 2023). Additionally, we found that GloFAS underestimated runoff in the Irrawaddy-Sittang river system. To correct for this bias, we applied a ~~bias correction using a linear regression~~ linear regression-based correction (see Appendix Figure A1) between the original GloFAS discharge and discharge data from the Global Runoff Data Centre ~~(GRDC; Recknagel et al., 2023)~~ (GRDC; Recknagel et al., 2023) for the Irrawaddy-Sittang regions. Finally, we manually removed discharge in the model sponge layers of the Sunda Strait and Malacca Strait.

2.3 Biogeochemical model configuration and changes specific to Indian Ocean

The ~~ocean physical~~ physical ocean model is coupled to the ~~Carbon, Ocean Biogeochemistry and Lower Trophics module version 2 (COBALTv2, Stock et al., 2014, 2020)~~COBALT v2 (Stock et al., 2014, 2020). COBALTv2 represents 33 tracers including nutrients (nitrate, phosphate, silicate, and iron), three phytoplankton groups (small, large, diazotrophs), three zooplankton groups (small, medium, large), three dissolved organic carbon pools (labile, semi-refractory and ~~refratory~~refractory), one particulate detritus pool, oxygen, and carbonate system.

Several parameters of the standard COBALTv2 model from Stock et al. (2020) were modified to match observational constraints and characteristics of the Indian Ocean and improve ~~some of the~~ model biases, including ~~the~~ a bias in the extent and volume of the ~~oxygen minimum zone~~ OMZ in the Bay of Bengal.

- Detritus sinking velocity was increased from 100 to 120 m d^{-1}, based on *in-situ* sediment trap observations indicating sinking speeds up to 160-280 m d^{-1} in the Indian Ocean (Rixen et al., 2019b).

- The burial fraction was increased (the equivalent half-saturation in the denominator of Equation 3 from Dunne et al., 2007, was reduced from 7 to 1 mmolC m^{-2} d^{-1}) . This increased the burial of ~~POC~~ particulate organic carbon from 0.013 PgC y^{-1} to 0.026 PgC y^{-1} in the tropical Indian Ocean, in better agreement with the burial of 0.028 PgC y^{-1} found in the observation-based reconstruction of LaRowe et al. (2020).

- The oxygen half-saturation for nitrification ($k_{nit,O2}$ in Stock et al., 2020) was reduced from 3.9 to 2.0 μmol O_2 kg^{-1}, based on recent observations indicating a lower oxygen threshold for ammonium oxidation in the ~~oxygen minimum zones (OMZs)~~ OMZs (Bristow et al., 2016; Peng et al., 2016; Frey et al., 2023).

- The oxygen constraint on water column denitrification was modified from $O_{2,min}/(k_{O2}+O_{2,min})$ when O_2 <0.8 μmol kg^{-1} (see Appendix A3 in Stock et al., 2020) to $O_2/(k_{O2}+O_2)$ when $O_2 < 4.0$ μmol kg^{-1}, in line with findings that the oxygen threshold below which denitrification starts is typically between 4 and 5 μmol kg^{-1} (Paulmier and Ruiz-Pino, 2009).

2.4 Biogeochemical model forcing

2.4.1 Initial state, open boundary conditions and model drift

~~Nutrients~~ For the model spin-up, nutrients (nitrate, phosphate, and silicate) and oxygen were initialized using annual means from the World Ocean Atlas 2018 ~~(WOA18, Garcia H.E. et al., 2019). Initial DIC~~(WOA18; Garcia et al., 2019). Dissolved inorganic carbon (DIC) and alkalinity were initialized using annual means from the Global Ocean Data Analysis Project version 2 (GLODAPv2), which are representative of year 2002 (Olsen et al., 2016). Other biogeochemical tracers were initialized with very low seed values of 10^{-10}. This initial value has a ~~small~~ negligible impact on the solution as most of these remaining tracers have turnover time-scales much shorter than the ~~32 years~~ 32-year spin-up duration (e.g., typically of a few days for phytoplankton), except semi-refractory dissolved organic matter (decay time-scale of 10 years). Atmospheric CO_2 forcing was taken from the global carbon budget project (Friedlingstein et al., 2022). Biogeochemical ~~OBCs are from monthly climatologies of WOA18~~ boundary values are prescribed from WOA18 monthly climatologies for nitrate, phosphate, silicate, and oxygen~~, and annual means from GLODAPv2 for~~ . For DIC and alkalinity boundary values, annual mean fields were estimated using the Empirical Seawater Property Estimation Routines (ESPER) MATLAB code (Carter et al., 2021), based on annual mean temperature and salinity from ORAS5. The OBC for biogeochemical tracers is set using the reservoir scheme (see section 2.2), with an outflow length scale of 9 km but an increased inflow length scale of 300 km, giving more weight to the solution within the model domain. This decoupling between contributions from the inflow and outflow limits the influence of the ~~OBC~~ boundary external forcing on the model domain, specifically when the ~~conditions~~ fields at the boundaries are poorly constrained such as for biogeochemical tracers. Model drift after the 32-year spin-up and over the 41 years of a ~~control~~ hindcast simulation with constant forcing is small, with linear trends $< 0.05\%$ for oxygen, nitrate, DIC, alkalinity, semi-refractory dissolved organic

nitrogen pools and integrated primary productivity (see Appendix Figure A2). The slight drift indicates that the hindcast simulation starts from a well-equilibrated initial state provided by the spin-up simulation.

2.4.2 Atmospheric deposition

The model is forced with monthly atmospheric deposition of nitrogen (wet and dry deposition of nitrate and ammonium), iron, phosphorus, and lithogenic dust derived from the archived GFDL Earth system model version 4.1 (ESM4.1) historical simulation[1] (1980–2014) and Shared Socioeconomic Pathways 5-8.5 (SSP5-8.5) scenario[2] (after 2014) (Stock et al., 2020; Horowitz et al., 2020; (2014–2020; Stock et al., 2020; Horowitz et al., 2020; Paulot et al., 2020). ESM4.1 includes interactive modules for anthropogenic and natural (e.g., biomass burning, lightning) reactive nitrogen emissions, photochemical reactions, removal of nitrogen by wet and dry deposition, as well as a land-atmosphere-ocean cycling of dust and ocean ammonia outgassing (Paulot et al., 2020; Horowitz et al., 2020). Interannual variability in ESM4.1 is not in phase with observed variability (as for any coupled Earth system model). For dry and wet deposition of oxidized and reduced nitrogen, we therefore used a 15-year moving by month average (e.g., January 2000 is an average of all Januaries between years 1993 and 2007) that retain the seasonality and long-term decadal the decadal anthropogenic increase in deposition but removed the interannual variability (see Appendix Figure A3). For iron, phsophorus phosphorus and lithogenic material deposition, we used monthly mean climatologies over the 1950-2022 period (ESM4.1 does not include the effects of fossil fuel burning etc. that would yield a significant long term trend in these fields, although it would include the smaller impact of long-term wetting / drying, wind and/or precipitation trends that we ignore here). Iron and dry lithogenic dust depositions are from ESM4.1 outputs. Phosphorus deposition was evaluated using the ESM4.1 climatology in dry lithogenic dust deposition, assuming a phosphorus content of 563 ppm in dust, of which 22% is bioavailable (see Herbert et al., 2018; Ross et al., 2023). See details about the influence of atmospheric deposition in this model in Malsang et al. (2024).

2.4.3 River biogeochemical inputs

The riverine fluxes of dissolved and particulate nutrients (nitrogen and phosphorus) are derived from the annual mean loads of inorganic and organic nitrogen and phosphorus from the Global Nutrient Export from WaterSheds2 (GlobalNEWS2), referenced to the year 2000 (Mayorga et al., 2010). We include riverine inputs of dissolved inorganic nitrogen (DIN), dissolved inorganic phosphorus (DIP), dissolved organic nitrogen (DON), dissolved organic phosphorus (DOP), and bio-available particulate organic nitrogen (PON). We do not include bio-available particulate organic phosphorus (POP) as the river input of DIP is already likely too high in GlobalNEWS2 (Jiao et al., 2023). DON and DOP are distributed among different dissolved organic pools, with 30% allocated to the labile pool, 35% to the semi-labile pool, and 35% to the semi-refractory pool (Wiegner et al., 2006). The riverine PON is assumed 100% bio-available.

The riverine input of iron is set at a value of 70 nmol kg^{-1} based on Raiswell and Canfield (2012). In the Bay of Bengal (78°E-103°E) region, the riverine DIN concentration is reduced by 80% based on coastal nitrate data collected by Krishna

[1] https://www.wdc-climate.de/ui/cmip6?input=CMIP6.CMIP.NOAA-GFDL.GFDL-ESM4.historical
[2] https://www.wdc-climate.de/ui/cmip6?input=CMIP6.ScenarioMIP.NOAA-GFDL.GFDL-ESM4.ssp585

et al. (2016). This adjustment is supported by Zhou et al. (2022) and Jiao et al. (2023), which compared several global nutrient transport models highlighting that GlobalNEWS2 tended to overestimate total nitrogen riverine inputs. The riverine flux of DIN in the Arabian Sea and the flux of other nutrients in both the Arabian Sea and Bay of Bengal are kept equal to the original values from GlobalNEWS2. The riverine inputs of DIC (0.32 mol m^{-3}) ~~,~~and alkalinity (0.42 mol equivalents of alkalinity m^{-3}) are assigned constant concentrations, consistent with those used in the GFDL-ESM4.1 Earth system model (Stock et al., 2020).

To reflect spatial differences in sediment supply, we specify riverine lithogenic concentrations based on observational data from Milliman and Farnsworth (2011). The lithogenic input from rivers was adjusted to 200 g m^{-3} for major rivers (i.e., rivers with sediment loads exceeding 10 Mt y^{-1}, e.g., Godavari, Krishna, Ganges, Brahmaputra, Irrawaddy, Sittang, Salween, Indus, Tapti and Narmada rivers~~,~~ ; see Figure 1 for rivers location) and 20 g m^{-3} for all other rivers, rather than applying a global constant of 13 g m^{-3} used for all rivers as in Stock et al. (2020). These adjustments account for the significantly higher total suspended sediment loads in these rivers (Milliman and Farnsworth, 2011; Rixen et al., 2019b), and are supported by river observations from Milliman and Farnsworth (2011) showing a broad range from 10 g m^{-3} (Muvattupuzha River) to 1,061 g m^{-3} (Ganges River). In the model, this higher lithogenic flux protects more particulate organic matter from remineralization, thereby increasing organic carbon export to the deep ocean and reducing oxygen consumption in the subsurface. This is in line with observations that underscore the significant role of lithogenic matter in reducing organic matter remineralization and accelerating carbon export in the northern Indian Ocean (Rixen et al., 2019b).

These concentrations of nutrients, DIC, alkalinity, lithogenic and organic material (constant in time) are incorporated using the GloFAS freshwater inputs and by assigning them to the nearest neighboring river mouths, with larger rivers given priority over smaller ones. Nutrient loads vary in accordance with changes in river discharges, and the baseline configuration presented in this study does not account for the fluctuations and trends in observed nutrient concentrations during the 1980-2020 model simulation period.

3 Methods for assessing model spatial and temporal variability

3.1 Physical and biogeochemical datasets

We used satellite and *in-situ* observations to assess modeled physical and biogeochemical basin-scale patterns as well as seasonal, interannual and intraseasonal variability. See Table 2 for a list of all datasets and their references.

For the basin-scale evaluation of ~~the~~ physical fields, we used Argo gridded temperature (Roemmich and Gilson, 2009), temperature and salinity from the ~~World Ocean Atlas 2018 (WOA18, Garcia H.E. et al., 2019)~~WOA18 (Garcia et al., 2019), satellite-based SST from the Optimum Interpolation SST (OISST) version ~~2~~ 2.1 (Banzon et al., 2016), sea surface height (SSH) and sea level anomaly ~~(SLA) from Aviso~~ from AVISO and distributed by the Copernicus Marine and Environment Monitoring Service (CMEMS~~) (~~; http://www.marine.copernicus.eu), the mixed layer depth ~~climatology from De Boyer Montégut et al. (2004, updated~~ ~~,~~(MLD) climatology from De Boyer Montégut et al. (2004; updated in November 2008; https://mld.ifremer.fr/Surface_Mixed_Layer_Depth.php) and ocean surface currents from the OSCAR drifter database (ESR, 2009). In addition, we used data from the

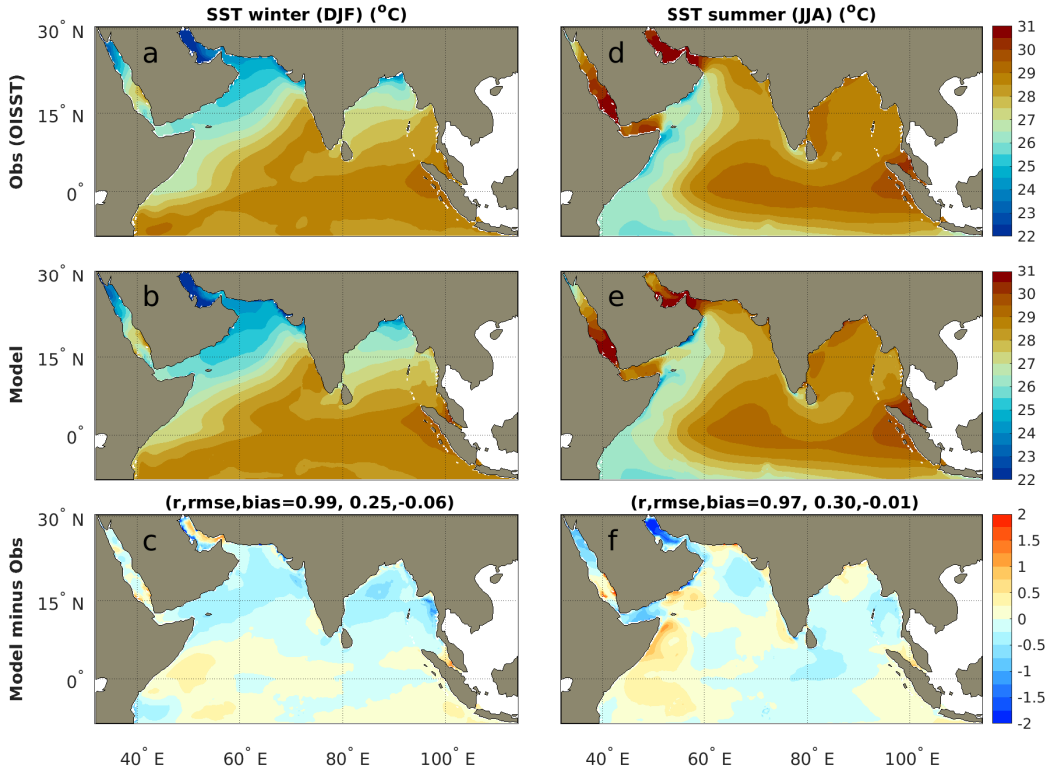

Figure 3. Sea surface temperature (SST) during (a-c) winter (December-February) and (d-f) summer (June-August) monsoons. Panels (a,d) show OISST ~~optimum interpolation from~~ observations, (b,e) show MOM6-COBALT-IND12 model and (c,f) show differences between model and observations. Correlation coefficients r, RMSE and bias between the observed and model seasonal means are indicated. See details on observations in Table 2. Model results are averaged over the 1980-2020 period.

Research Moored Array for African-Asian-Australian Monsoon Analysis and Prediction (RAMA)~~array~~, specifically from two moorings capturing the east-west contrast in the basin at 57°E, 4°S and 95°E, 5°S ~~(data downloaded from the Pacific Marine Environmenta~~ (data downloaded from the Pacific Marine Environmental Laboratory NOAA website; McPhaden et al., 2009), and observations from water mass properties at the Red Sea outflow from Sofianos et al. (2002).

For the basin-scale biogeochemical model evaluation, we used oxygen concentrations from WOA18 ~~(Garcia H.E. et al., 2019)~~ (Garcia et al., 2019) and from Bianchi et al. (2012)~~and~~ , surface chlorophyll data from the European Space Agency ocean color climate change initiative ~~(OC-CCI version 5.0)(Sathyendranath et al., 2019)~~(OC-CCI version 5.0; Sathyendranath et al., 2019) , vertical chlorophyll data from bio-Argo (Wong et al., 2020), and integrated primary productivity ~~(PP)~~ from the satellite-based Carbon-based Production Model (CbPM) algorithm, the Carbon, Absorption, and Fluorescence Euphotic-resolving (CAFE) algorithm, the Vertically Generalized Production Model (Standard-VGPM) algorithm and its alternative formulation (Eppley-VGPM), all accessed via the Ocean Productivity website (http://sites.science.oregonstate.edu/ocean.productivity/index.php).

In addition, we used *in-situ* observations compiled from a literature review including 24 studies and 351 stations (see Table 2 for references). River inputs and particulate organic and lithogenic matter in the model were evaluated using river discharge from the Global Runoff Data Center ~~(GRDC, Recknagel et al., 2023)~~(GRDC; Recknagel et al., 2023).

3.2 Analysis and evaluation metrics

We evaluated the amplitude of intraseasonal variability (ISV) using SSH temporal variability as a proxy for mesoscale eddies and planetary waves ~~(Rossby and Kelvin waves, e.g., Cheng et al., 2013)~~(Rossby and Kelvin waves; e.g., Cheng et al., 2013). Observed and simulated SSH were detrended using a linear regression and filtered using a 14-120 days band pass filter to remove the seasonal cycle, interannual variability and long-term trend, and only retain the intraseasonal timescales. The Dipole Mode Index (DMI) used to evaluate IOD phases was calculated as the SST anomalous gradient between the western equatorial Indian Ocean (50°E-70°E and 10°S-10°N) and the southeastern equatorial Indian Ocean (90°E-110°E and 10°S-0°N, Saji et al., 1999). Finally, we used three metrics throughout the study to compare model results and observations: the ~~linear~~ Pearson correlation coefficient (r) which measures the correlation between observations and model in time (for time-series) or in space (for maps), the root mean square error (RMSE, i.e., quadratic mean of model minus observations) which measures the model accuracy compared to observations, and the bias (i.e., model minus observations) which indicates if the model underestimates or overestimates the observed fields. For the validation of climatological annual and seasonal means, model outputs are averaged over the period 1980–2020. Observation-based data products are treated based on their availability: if the dataset provides climatological means (annual or seasonal), we use the provided values directly. If not, we compute climatological means over the available time span of the observational dataset (see time span in Table 2).

4 Monsoon-driven seasonality

4.1 Sea surface temperature as an indicator of seasonal dynamics

Patterns of ~~sea surface temperature (SST)~~ SST in the northern Indian Ocean follow the well described basin-scale features associated with the monsoon reversal (e.g., Schott and McCreary, 2001). MOM6-COBALT-IND12 captures seasonal SST patterns ~~particularly well, especially~~ well, notably the contrast between the vast warm pool (SST >28°C) that extends over most of the basin and the regions with colder SSTs that develop in response to seasonal variations in atmospheric and oceanic circulation (~~Figures~~ Figure 3). During the winter monsoon, the model simulates the relatively cold ~~sea surface temperatures~~ water (SST <26°C) associated with evaporative cooling in the northern Bay of Bengal, and a combination of evaporative cooling and convective mixing (~~mixed layer depths~~ MLD of 40-60 m) in the northern Arabian Sea (Figures 3a-c and 4a-c). During the summer monsoon, the model simulates the colder summer SSTs observed in wind-driven upwelling regions along the western boundary coasts (e.g., Oman, Yemen, Somalia, Kenya and Tanzania where SST <26°C), and in the weaker upwelling controlled by Kelvin wave propagation along the southwestern Indian coast (SST ~27°C~~,~~; Figure 3d-f~~,~~; see details on wave propagation in section 4.3). At the basin scale, modeled SST patterns ~~are tightly correlated~~ shows strong agreement

Table 2. Observational products used to evaluate MOM6-COBALT-IND12

Parameter	Sampling frequency	Reference dataset
Sea surface temperature	monthly optimum interpolation (1982-2020)	OISSTv2.1 includes satellites, ships, buoys, Argo floats (Banzon et al., 2016)
Mixed-layer depth	monthly climatology	De Boyer Montégut et al. (2004) - updated Nov. 2008
Surface currents	5-day averaged monthly	OSCAR drifter database (ESR, 2009)
Sea level anomaly	daily satellite-based	Copernicus (Lopez, 2018)
Ocean temperature and salinity	monthly climatologies	Wold Ocean Atlas 2018 (WOA18, Garcia H.E. et al., 2019) (WOA18, Garcia et al.,
	in-situ profiles	Wold Ocean Database 2018 (WOD18, Boyer et al., 2018)
	in-situ profiles	RAMA moorings (McPhaden et al., 2009)
Wind speed	monthly satellite	CCMP (Mears et al., 2022)
	in-situ	RAMA moorings (McPhaden et al., 2009)
Red Sea Outflow properties	in-situ sampling (1995-1996)	Sofianos et al. (2002)
Oxygen concentration	monthly climatologies	WOA18 (Garcia H.E. et al., 2019) (Garcia et al., 2019) and Bianchi et al. (2012)
Surface chlorophyll	monthly climatology	OC-CCI v5.0 (Sathyendranath et al., 2019)
River Discharge	daily/annual mean	Global Runoff Data Center (GRDC, Recknagel et al., 2023)
		Jian et al. (2009), Krishna et al. (2016)
Riverine lithogenic flux	in-situ sampling	Milliman and Farnsworth (2011)
Marine lithogenic/organic flux	in-situ sampling	Rixen et al. (2019b)
Net primary productivity	monthly satellite-based	CbPM (Westberry et al., 2008), CAFE (Silsbe et al., 2016), standard-VGPM, Eppley-VGPM (Behrenfeld and Falkowski, 1997)
	in-situ sampling (351 stations)	Saxena et al. (2023); Marra et al. (2021); Sarma et al. (2020) Löscher et al. (2020); Sarma and Dalabehera (2019) Ahmed et al. (2017); Gandhi et al. (2010, 2011) Kumar et al. (2010); Naqvi et al. (2010); Prakash et al. (2008) Prasanna Kumar et al. (2007a, b); Naqvi et al. (2006) Gauns et al. (2005); Kumar et al. (2004) Barber et al. (2001); Watts and Owens (1999); Watts et al. (1999) Savidge and Gilpin (1999); McCarthy et al. (1999) Veldhuis et al. (1997); Devassy et al. (1983) Bhattathiri et al. (1980); Radhakrishna (1978)

with observed patterns(correlation coefficient , characterized by a high correlation coefficient (r>0.97), and model SST biases are small low RMSE (0.25-0.3°C), and small biases (regional mean SST bias of 0.06-0.06°C in winter and 0.01-0.01°C in

summer for the 1980-2020 period). We note that the good agreement between observed and modeled SST is in part attributable to the strong influence of the prescribed observation-driven atmospheric surface boundary forcing that ~~control~~ controls air-sea heat fluxes in the model (e.g., temperature, wind~~etc. , see Methods).~~ ; see section 2). In addition, a comparison between ERA5 and Cross-Calibrated Multi-Platform (CCMP) wind products demonstrates that ERA5 wind forcing effectively captures the seasonal cycle and spatial distribution of the summer and winter monsoons (Appendix Figure A4).

The model captures the seasonal contrast in MLD between the Arabian Sea and the Bay of Bengal, with deeper mixed layers in the Arabian Sea and shallower layers in the Bay of Bengal during both winter and summer (Figure 4). The MLD is generally deeper in summer than in winter. The spatial patterns, including the locations of local MLD maxima, are broadly consistent with observational data. Quantitatively, the basin-wide correlation values are similar between the two seasons, although the RMSE is larger in summer (8.09 m) than in winter (7.00 m). One possible contributor to the larger summer bias is the enhanced wind forcing during the monsoon season (see Figure A4), which intensifies turbulent mixing and deepens the mixed layer. At the same time, the MOM6 model includes the mixed layer eddy (MLE) parameterization of Fox-Kemper et al. (2011), which represents restratification driven by baroclinic eddies within the mixed layer. This restratification process may also be more active in summer, potentially leading to an overcorrection that offsets vertical mixing too strongly. The interaction between intensified wind-driven mixing and enhanced restratification may thus contribute to the larger MLD bias observed in summer compared to winter.

4.2 Seasonal reversal of upper ocean circulation

MOM6-COBALT-IND12 ~~simulates the~~ reproduces the observed seasonal reversal of the main current systems~~as observed by~~ , as confirmed by comparison with the updated OSCAR drifters database (arrows on Figure 4). In the Equatorial band, these seasonal changes include the shift from an eastward transport by the Northeast Monsoon Current (~~Equator-10~~Equator to 10°N) and westward transport by the South Equatorial Countercurrent (5°~~S-Equator~~S to Equator) in winter, to a mostly westward transport by the the Southwest Monsoon Current in summer (~~Equator-10~~Equator to 10°N, Figure 4). MOM6-COBALT-IND12 also simulates the summer strengthening and reversal of the western boundary Somali Current system and its extension northward along the Arabian Peninsula (Figure 4). In the following, we compare the simulated and observed seasonal evolution of this western boundary system~~focusing~~ , with a focus on the characteristics that are most relevant to the biogeochemical response, and refer the reader to prior work for a more in-depth description of its dynamics (e.g., Schott and McCreary, 2001; Wirth et al., 2002; Brandt et al., 2003; Sengupta et al., 2001; Beal and Donohue, 2013; Beal et al., 2013; Vic et al., 2014; Wang et al., 2018).

Figure 5 compares the simulated and observed seasonal evolution of the western boundary system. MOM6-COBALT-IND12 simulates relatively well the observed climatological evolution of the Somali Current. Before the summer monsoon (April), the Somali Current is relatively weak and flows northward along the western boundary, crossing the Equator in both observations and model. At the onset of the summer monsoon (June), the Somali Current intensifies, and separates at around 4°N into a northward alongshore current and an eastward flow that loops back across the equator and feeds the South Equatorial Countercurrent, a feature also known as the Southern Gyre (Beal et al., 2013). Simultaneously, a quasi-stationary anticyclonic

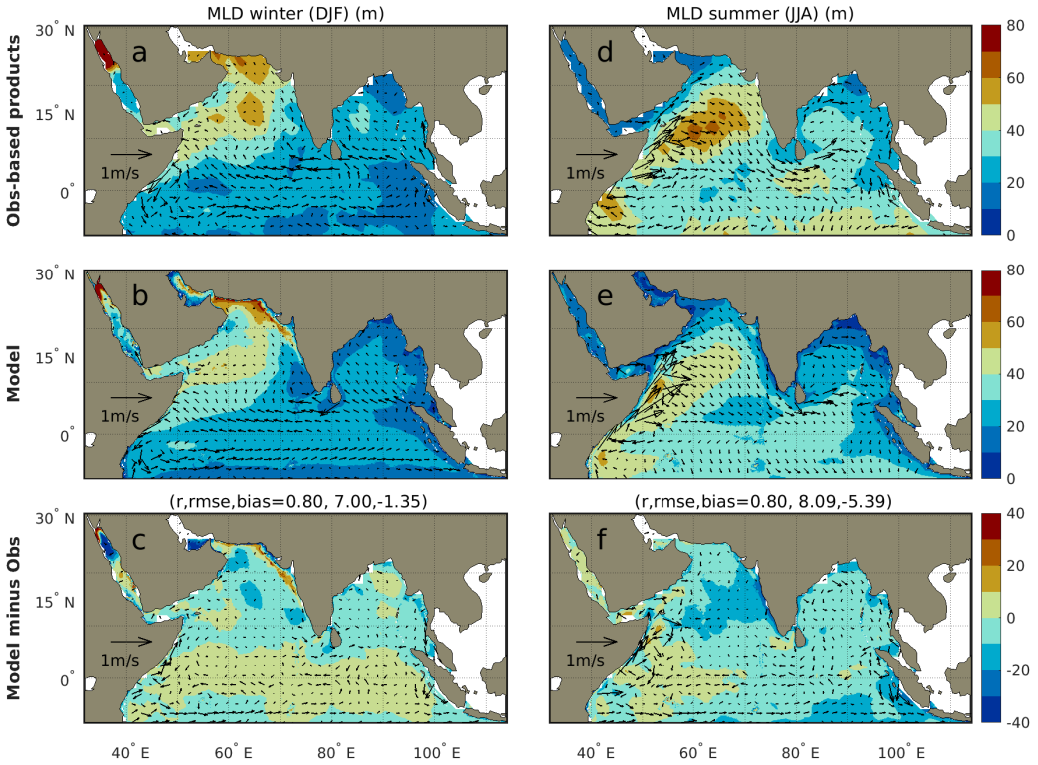

Figure 4. Seasonal mean mixed layer depth (MLD) and surface currents during a-c) winter (December-February) and d-f) summer (June-August) monsoons. Panels (a,d) ~~Observations~~ show observations, (b,e) show MOM6-COBALT-IND12 model and (c,f) show differences between model and observations. Correlation coefficients r, RMSE and bias between the observed and model seasonal MLD means are indicated. Observations are an update of De Boyer Montégut et al. (2004) for MLD and the OSCAR drifters database for surface currents (see Table 2). Model results are averaged over the 1980-2020 period.

mesoscale gyre called the Great Whirl develops at about 10°N (Figure 5). As the southwest monsoon progresses (August), the Great Whirl intensifies, becoming one of the largest and most energetic coherent vortices in the world ocean~~, and a third~~ . A smaller anticyclonic mesoscale eddy, the Socotra Eddy, also develops east of Socotra Island at this time (Figure 5). The structure of the Great Whirl at its peak is relatively similar in the model and shipboard and mooring observations, with an horizontal footprint of ∼500 km, a vertical extent of ∼1000 m, meridional currents of about 1 m s^{-1} at the surface and 0.1 m s^{-1} at 1000 m depth ~~(Figures 5 and 6 and observations reported in Schott and McCreary, 2001; Beal and Donohue, 2013)~~ (Figures 5 and 6 and observations reported in Schott and McCreary, 2001; Beal and Donohue, 2013). Finally, during the fall intermonsoon (October), the gyre system decays, and by the winter monsoon (December), the surface signature of the Great Whirl and Socotra Eddy are not visible (~~Figures~~ Figure 5).

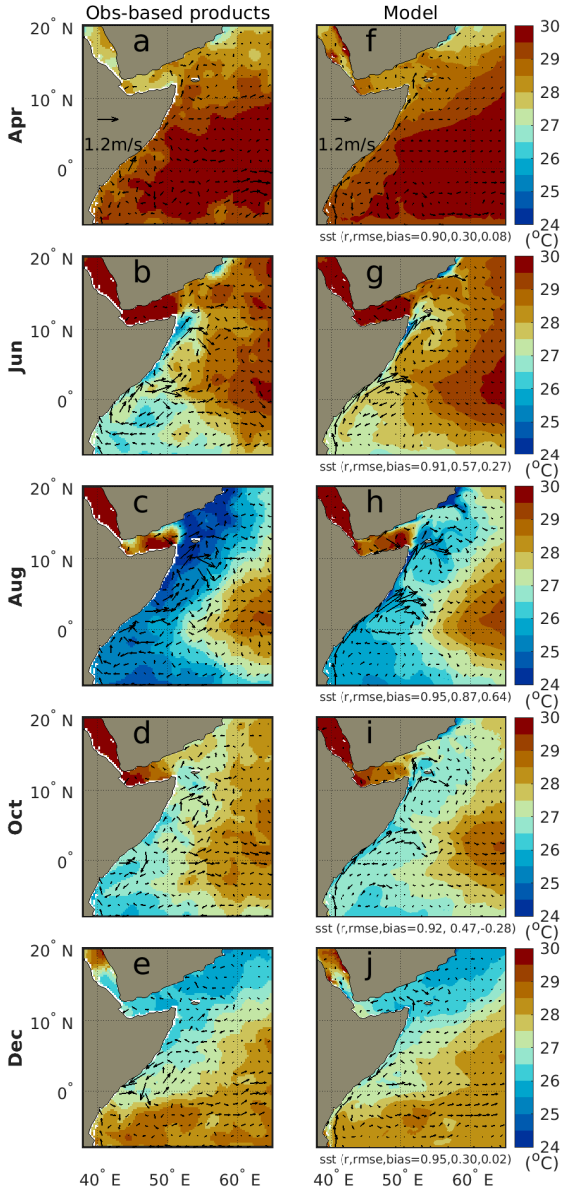

Figure 5. Climatological evolution of the western boundary Somali Current system showing SST (colors) and surface currents (vectors) in observation-based ~~data~~ products (~~left column~~a-e) and MOM6-COBALT-IND12 (~~right column~~f-j). ~~Data~~ Observation-based products are from OISSTv2.1 satellite for SST and the OSCAR drifters database for surface currents (see Table 2). Correlation coefficients r, RMSE and bias between the observed and modeled SST means are indicated.

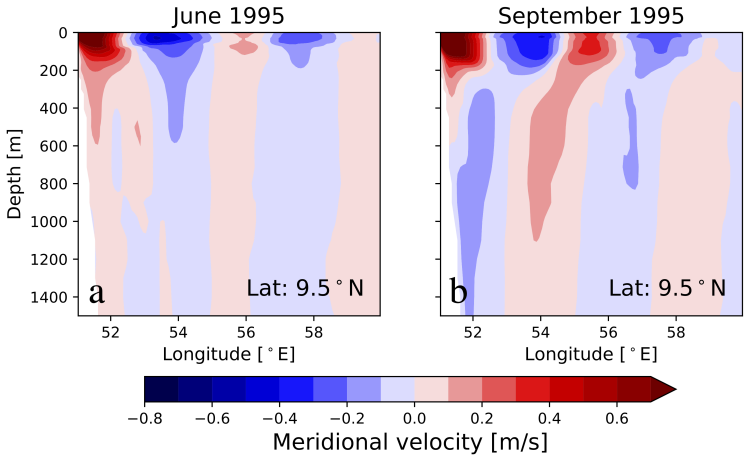

Figure 6. West-east depth section of meridional velocities across the Great Whirl in (a) June and (b) September 1995 in the MOM6-COBALT-IND12. These sections ~~can be compared~~ are comparable to observations from Beal and Donohue (2013) (see their Figure 2). Positive velocities are northward.

4.3 Coastal upwelling and downwelling

Patterns in sea level anomaly ~~(SLA)~~ can be used as a proxy for coastal seasonal upwelling (negative anomalies) and downwelling (positive anomalies) motions (Figure 7a-d). In summer, the model reproduces the amplitude and patterns of wind-driven upwelling along the western Arabian Sea (e.g., Oman, Yemen and Somalia), and western Bay of Bengal (eastern India) coasts (Figure 7b,d~~,~~; correlation coefficient r = 0.91~~,~~; RMSE = 0.02 m). We note that the latter upwelling has little influence on SST in both observations and models (Figure 3) due to the strong near-surface stratification imposed by high freshwater inputs in the Bay of Bengal, and hence the strong atmospheric control on SST in this region (e.g., Shetye et al., 1991; Shenoi et al., 2002). In winter, SLA patterns largely mirror summertime patterns due to the reversal of the winds and ocean circulation, with downwelling motions (positive SLA) that develop along the western Arabian Sea coasts and the western Bay of Bengal (Figure 7a-d). This pattern is also well captured by the model (Figure 7a,c~~,~~; correlation coefficient r = 0.93~~,~~; RMSE = 0.02 m).

Wind-driven upwelling and downwelling are strongly modulated by the seasonal propagation of coastal Kelvin waves around the rim of the northern Indian Ocean (e.g., McCreary et al., 1993; Yang et al., 1998; Nienhaus et al., 2012; Vinayachandran et al., 2021). We examine the evolution of these coastal waves following changes in SLA along the Equatorial and coastal wave guides using the review and description provided in Pearson et al. (2022). Modeled coastal SLA patterns remarkably capture the timing and amplitude of the observed patterns, starting with the equatorial upwelling Kelvin waves triggered by wind changes in the summer and winter monsoons (arrows for waves I and II), and the equatorial downwelling Kelvin waves triggered during the spring and fall intermonsoons (arrows for waves III and IV on Figure 7e-f). These successive wave trains travel east and then counter-clockwise around the Bay of Bengal and the Arabian Sea. The model also captures the summer upwelling and winter downwelling waves excited in the northwestern Bay of Bengal (arrow for waves V and VI) and at the

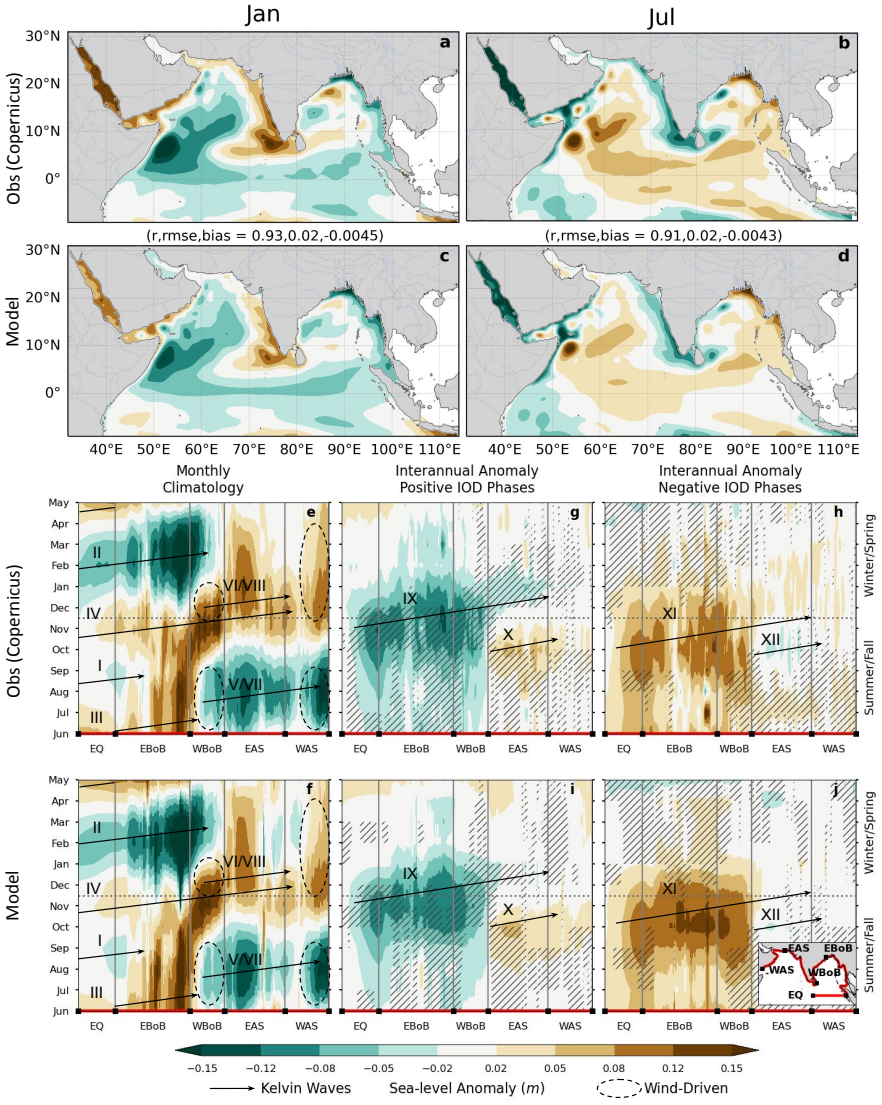

Figure 7. Coastal upwelling/downwelling inferred from sea level anomalies (SLA, in m) from satellite observations and ~~in~~ MOM6-COBALT-IND12: (a-d) January and July climatological maps (1993–2020 data and model average, (e-f) Hovmüller of seasonal SLA (1993–2020 data and model average, and (g-j) Hovmüller interannual SLA (seasonal cycle removed) for positive IOD (g,i) and negative IOD (h,j) composites. In panels e-j, the x-axis follows the equatorial and coastal wave guides (red line in inset) starting at the equator (EQ), counterclockwise around the eastern and western Bay of Bengal (EBoB/WBoB) and around the eastern and western Arabian Sea (EAS/WAS). Upwelling (negative SLA) and downwelling (positive SLA) are indicated by circles when wind-driven and by arrows when wave-driven (approximate wave speed of 2.4 m/s consistent with theoretical first baroclinic mode Kelvin waves~~,~~; roman numerals used in text). Unhatched/hatched regions indicate where the IOD anomaly reinforces/opposes the seasonal signal. Satellite SLA is from Copernicus (see Table 2).

tip of India (arrows for waves VII and VIII), reinforcing the wind-driven summer upwelling and winter downwelling (dashed circles) that develop in the western Bay of Bengal and eastern Arabian Sea (Figure 7e-f). See further details in Pearson et al. (2022) and references herein.

4.4 Sea surface salinity and river plumes

The model reproduces the main observed patterns of ~~sea surface salinity (SSS~~ SSS (Figure 8a-f), including the high SSS (SSS >34 psu) in the Arabian Sea where evaporation exceeds precipitation and riverine runoff, and the much fresher (SSS <34 psu) Bay of Bengal where precipitation and runoff exceed evaporation~~(correlation r>~~. Performance metrics indicate that the simulation achieves a strong spatial correlation (0.95~~and regional RMSE < 0.7, Figure 8 a-f~~ 0.96) and a small regional RMSE (0.53-0.71). It also reproduces the seasonality of SSS associated with the monsoon, in particular the extent of the surface ~~fresh water~~ freshwater plumes (SSS <~~31~~31psu) associated with the river discharge in the Bay of Bengal. Riverine runoff in the Bay of Bengal is lowest during the dry winter monsoon and spring intermonsoon, and peaks during the summer monsoon and early fall intermonsoon, with discharges up to 1.5×10^5 m^3 s^{-1} in the Ganges-Brahmaputra river system and 0.4×10^5 m^3 s^{-1} in the Irrawaddy-Sittang river systems for which we have observed time-series (Figure 8g-h). The runoff product used to force the model reproduces the seasonality of the Ganges-Brahmaputra and the Irrawaddy-Sittang river systems (GloFAS was modified based on runoff observations in this system~~, see Methods~~; see Section 2.2.3). As a result, the observed and simulated freshwater plumes are confined to the river mouths in late spring when runoff is lowest (April), and extend 200 to 500 km offshore in summer when runoff peaks (August), before being stretched out alongshore in the northern and western Bay of Bengal by horizontal transport in fall and winter (December~~,~~ ; Figure 8c). The seasonality of SSS and the impact of river discharge are more limited in the Arabian Sea. The GloFAS runoff product captures the discharge of one of the main river ~~system~~ systems for which we have direct observations, i.e., the ~~Narmada Tapti rivers(~~Narmada-Tapti rivers, with simulated values of 86.95 km^3 y^{-1} ~~in GloFAS and~~ compared to 75.31 km^3 y^{-1} ~~in~~ reported by Krishna et al. (2016), and MOM6-COBALT-IND12 reproduces the range of salinity observed on the shelf at the river mouth (Figure 8a-f).

4.5 Seasonal plankton bloom dynamics

The northern Indian Ocean is characterized by two blooming seasons associated with the summer and winter monsoons that can be identified from surface chlorophyll ~~(Chl> 0.5 mg m^{-3}, Figure 9 a-e; e.g., Lévy et al., 2007)~~(Chl> 0.5 mg m^{-3}; Figure 9a-e; e.g., Lévy e . In the Arabian Sea, MOM6-COBALT-IND12 simulates the winter bloom (Figure 9a-c), which develops in response to nutrient supply by convective mixing (~~mixed layer depths~~ MLD of 40-80 m~~,~~ ; Figure 4) and eddy vertical turbulent transport (Resplandy et al., 2011); it also simulates the summer bloom (Figure 9d-f) associated with the western and eastern Arabian Sea coastal upwelling systems (Oman, Yemen, Somalia, southwest India~~,~~ ; see section 4.3) and a combination of horizontal and vertical eddy turbulent transport that supply ~~nutrient~~ nutrients to the central Arabian Sea (Resplandy et al., 2011). In the Bay of Bengal, ~~surface chlorophyll is generally lower and presents a weak seasonality in both observations and models, mostly due to the strong stratification and lower nutrient supply and the~~ the persistently low surface chlorophyll and its weak seasonality primarily result from strong salinity-driven stratification, which suppresses vertical nutrient supply to

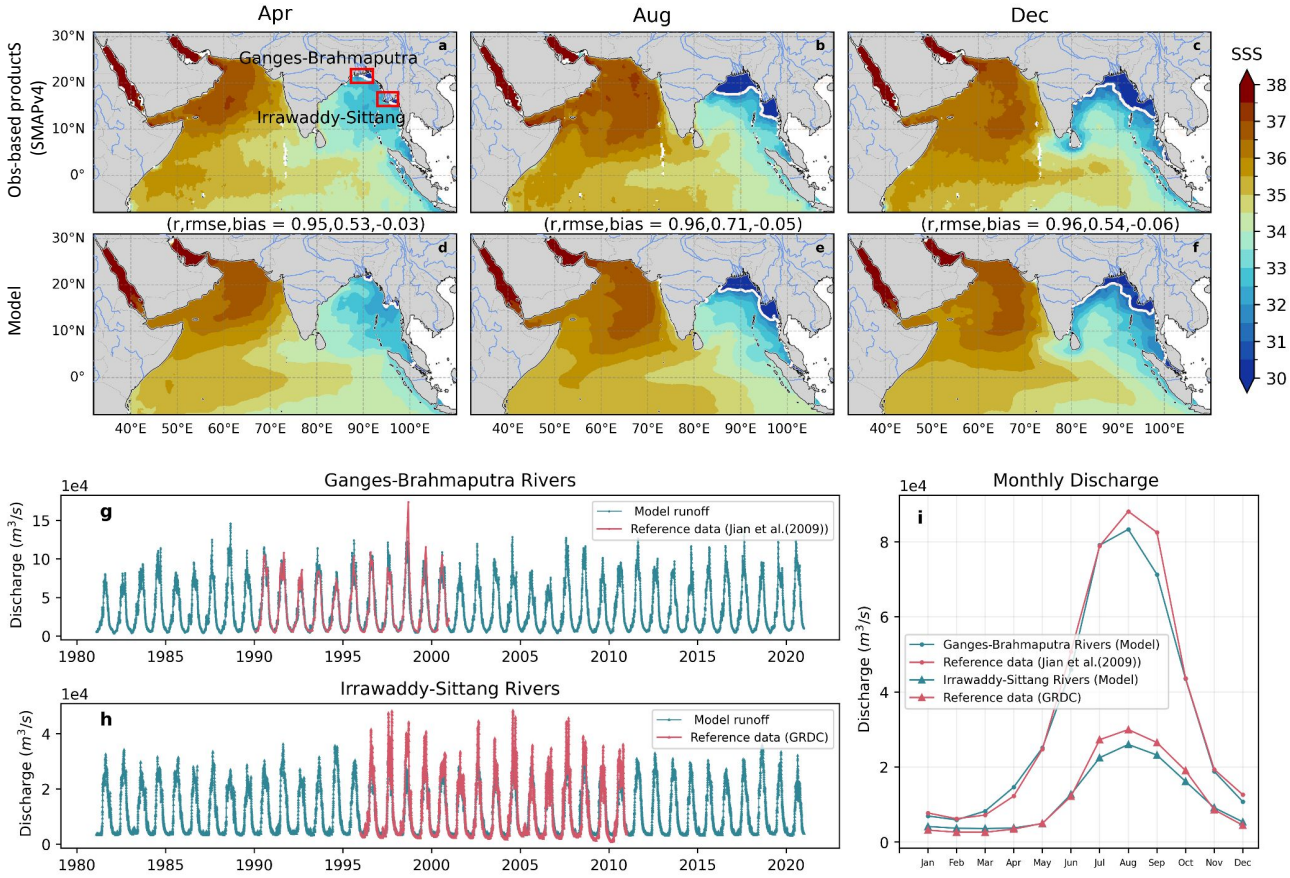

Figure 8. Seasonality in sea surface salinity (SSS) and river discharge: (a-f) Climatological SSS in April, August and December in the satellite SMAPv4 product and MOM6-COBALT-IND12 (2015-2019 period for both). White contour delimits waters with SSS < 31 psu~~)~~. (g-i) Water discharge from observations and ~~in~~ the modified GloFAS runoff product used to force MOM6-COBALT-IND12: (g) time-series of the Ganges-Brahmaputra river system, (h) time-series of the Irrawaddy-Sittang river system and (i) seasonal climatology for both systems over the period. See Table 2 for data source. A comparison of modified GloFAS to the raw GloFAS product is presented in Appendix Figure A1.

420 the mixed layer year-round (Sarma and Aswanikumar, 1991). Additionally, the presence of a subsurface chlorophyll ~~maxima (Sarma and Aswanikumar, 1991).~~

~~The model differs from~~ maximum confines most primary production below the mixed layer, further reducing surface chlorophyll levels and attenuating their seasonal variability (Sarma and Aswanikumar, 1991). The model also simulates the subsurface chlorophyll maximum captured by Argo floats in both the Arabian Sea and Bay of Bengal, with RMSE values

over the vertical ranging from 0.03 to 0.3 mg m^{-3} (Appendix Figure A5). This suggests that the model effectively represents the vertical distribution of plankton and associated subsurface biological dynamics. Overall, comparison of our model's mean bias and RMSE with values reported in previous studies suggests that our chlorophyll simulation performance falls within the median range relative to other regional biogeochemical models (Chakraborty et al., 2023; Gutknecht et al., 2016; Sunanda et al., 2024) .

The model overestimates surface chlorophyll concentrations by +0.25 to +0.75 mg m^{-3} offshore of the ~~satellite chlorophyll product offshore of~~ western boundary currents (along Somalia, Kenya, Tanzania, and Oman) and in the southern Bay of Bengal ~~where it simulates surface chlorophyll values that are higher (+0.25 to +0.75 mg m^{-3},~~ (Figure 9c-f). ~~Yet,~~ Such discrepancies might be partly attributable to uncertainties in model chlorophyll estimates arising from photoacclimation, which modulates cellular pigment content under varying light conditions (Stock et al., 2025) and/or biases in satellite-derived chlorophyll, which can differ from in-situ measurements by up to a factor of two and exhibit regional biases, especially in coastal areas (Dierssen, 2010; Sathyendranath et al., 2019; Schofield et al., 2004). Importantly, we find here that this model-satellite discrepancy has limited impact on biogeochemical fluxes. Specifically, the model captures relatively well the observed integrated ~~PP~~ primary productivity and seasonality obtained from both available *in-situ* sampling (351 stations) and satellite-based products in all regions, in particular those of the CbPM satellite ~~PP product~~primary productivity product, which is in better agreement with *in-situ* observations than the other satellite products (see Figure 10 and Kalita and Lotliker, 2023, for an evaluation of the different products). The model captures the magnitude of the double bloom productivity in the central and western Arabian Sea (about 1000-1500 mg C m^{-2} d^{-1} in ~~CAS and WAS~~Figure 10a,b,e), as well as the lower productivity observed in the Bay of Bengal (<1000 mg C m^{-2} d^{-1}~~, Figure 10a,b,e,~~; Figure 10f). The model also captures the timing of the summer bloom peak in productivity in the eastern Arabian Sea (EAS) and Somali upwelling (SOM), although the magnitude of modeled ~~PP~~ primary productivity might be underestimated in these regions (Figure 10a,c,d). The fact that the model simulates the magnitude of observed ~~PP~~ primary productivity (in carbon units) but overestimates the surface chlorophyll content suggests that it might overestimate the contribution of large phytoplankton~~(high chlorophyll to carbon ratio)~~ , which is characterized by a higher chlorophyll-to-carbon ratio, compared to small phytoplankton~~(low chlorophyll to carbon ratio).~~ , characterized by a lower chlorophyll-to-carbon ratio. This overestimation of the contribution of large phytoplankton to the assemblage would explain the good match in primary productivity and bias in chlorophyll.

In MOM6-COBALT-IND12, the phytoplankton limitation factors vary spatially and seasonally for the three phytoplankton groups included in the model (small, large and diazotroph~~,~~; Figure 11). In the western Indian Ocean, the model simulates a strong seasonality: nitrogen and phosphorus are the most limiting nutrients in spring and early summer (March to May), but iron limitation becomes more prevalent towards the end of the summer bloom (September) and even persists in certain regions of the northern Arabian Sea until early winter (December) before it gets replenished by winter mixing (Figure 11). This shift to iron limitation at the end of the summer monsoon is consistent with *in-situ* observations revealing a high-nutrient, low chlorophyll regime where phytoplankton growth is limited by iron in the Arabian Sea (Measures and Vink, 1999; Naqvi et al., 2010; Moffett et al., 2015; Moffett and Landry, 2020). We note, however, that during these periods of iron limitation, growth is weakly limited by nutrients (see total nutrient limitation values >0.5 in western and nothern Arabian Sea in September and

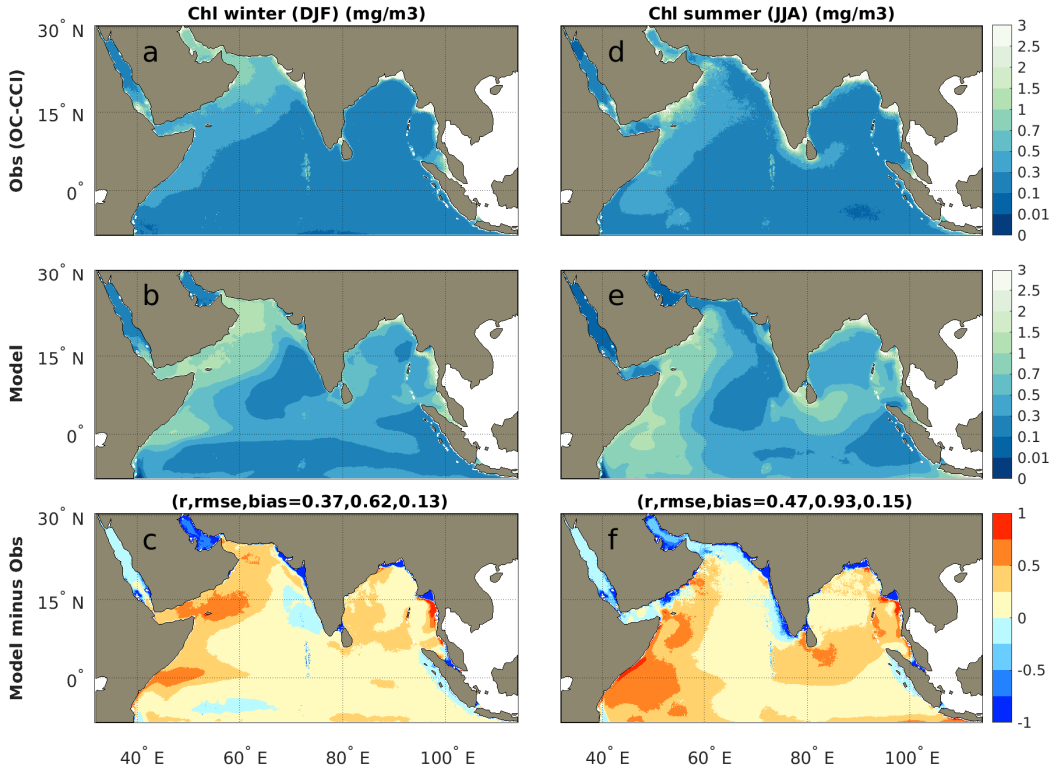

Figure 9. ~~Surface~~ Sea surface chlorophyll during (a-c) winter (December-February) and (d-f) summer (June-August) monsoons. Panels (a,d) ~~Satellite~~ show satellite observations, (b,e) show MOM6-COBALT-IND12 model and (c,f) show differences between model results and observations. Correlation coefficients r, RMSD and bias between the observed and model annual means are indicated. Chlorophyll observations are from OCI-CC satellite (see details in Table 2). Model results are averaged over the 1980-2020 period.

December in the Appendix Figure A6). In the eastern Indian Ocean, the seasonality is weaker and phytoplankton are generally limited by macronutrients (nitrogen and/or phosphorus), except in the northern Bay of Bengal where iron limitation becomes more important near river mouths that supply macronutrients in excess compared to iron (Figure 11). We note that the strong iron limitation near river mouths might be partly attributed to the way iron limitation is formulated in ~~COBLATv2~~COBALTv2. Indeed, iron limitation depends on a cell quota (rather than the ambient nutrient concentration used for macro-nutrient limitations), which requires time to establish near the river mouths. Yet, we note that the overall pattern of limitation simulated in the Bay of Bengal is consistent with incubation experiments showing a strong limitation by macronutrients in the southeastern Indian Ocean and co-limitations between macronutrients and iron in the Bay of Bengal (Twining et al., 2019).

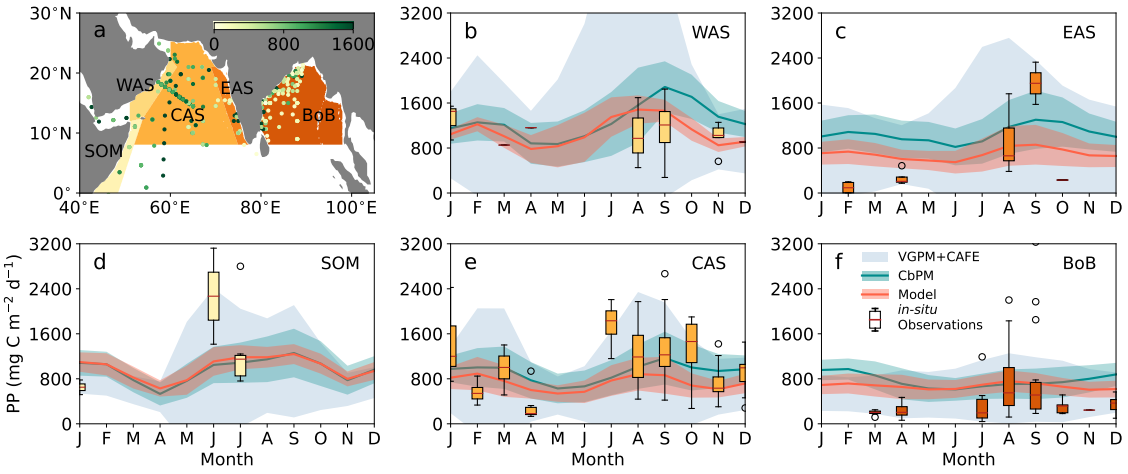

Figure 10. Seasonality in integrated primary productivity (PP). (a) maps of regions used to compare observation-based and modeled PP, showing *in-situ* observation sites with PP values in green (in mg C m^{-2} d^{-1}), (b-f) monthly climatology of PP in MOM6-COBALT-IND12 model (regional mean ± 1-sigma in dark orange), from available in-situ observations in each region (boxplots showing median, interquartile, range and outliers defined as outside of 1.5 times the interquartile range), in the CbPM satellite product (regional mean ± 1-sigma in cyan) which performs best in this region (Kalita and Lotliker, 2023), and three additional satellite products (± 1-sigma range of Standard-VGPM, Eppley-VGPM and CAFE in light blue). Regions are the western Arabian Sea (WAS), eastern Arabian Sea (EAS), Somalia coast (SOM), central Arabian Sea (CAS) and Bay of Bengal (BoB). Satellite and *in-situ* sampling observations are detailed in Table 2. Model and satellite-based climatologies are for the available observation period of 2003-2020.

5 Ocean interior, ventilation pathways and oxygen minimum zones

5.1 Ocean vertical structure and thermocline ventilation pathways

Observed subsurface temperature and salinity (300 m to 700 m average) reveal the signature of the main water masses that ventilate the thermocline in the Indian Ocean (Figure 12a,d). The Red Sea and Persian Gulf overflows contribute ~~to~~ warm and salty waters (>13°C and >35.6 psu) ~~in~~ to the Gulf of Aden and Gulf of Oman in the Arabian Sea, respectively (You and Tomczak, 1993). In contrast, the ~~northeastern Arabian (You and Tomczak, 1993). Incontrast, The~~ Indonesian Throughflow (ITF) and the water masses formed in the southern subtropical and subpolar regions (e.g., mode waters ~~,~~ and central waters) contribute relatively cold and fresh subsurface waters (<8°C and <35 psu) in the south of the domain, before being mixed and transported westward by the Southern Equatorial Current system ~~before~~ and flowing northward and crossing the Equator along the African continent (You, 1997; Schott et al., 2004; Sprintall et al., 2009; McCreary et al., 2013; Nagura and McPhaden, 2018). Finally, intermediate temperature and salinity in the Bay of Bengal (about 10°C and 35 psu) arise from the relatively weak thermocline ventilation~~(the Bay of Bengal is a shadow zone of thermocline ventilation)~~, mostly maintained by the eastward transport from the Arabian Sea and Equatorial region.

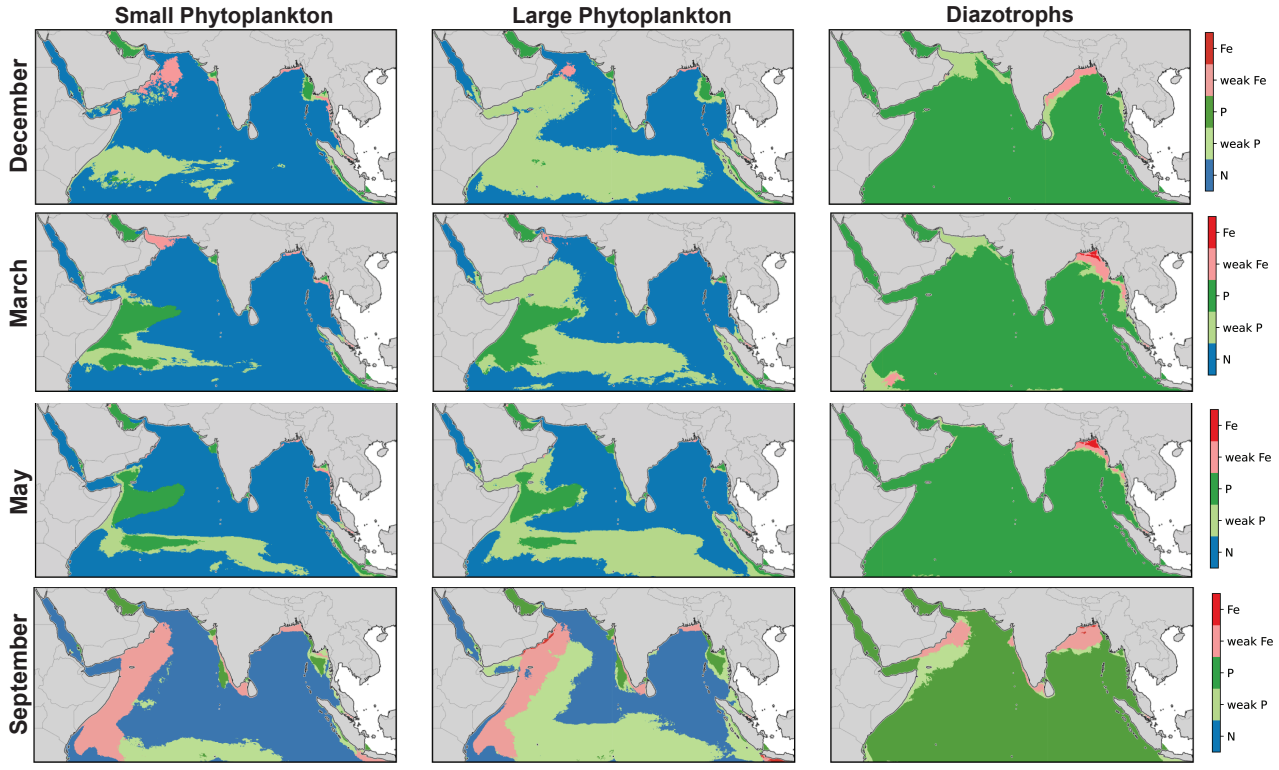

Figure 11. Climatological surface nutrient limitation (nitrogen N, phosphorus P and iron Fe) in MOM6-COBALT-IND12 for small phytoplankton, large phytoplankton and diazotrophs in December, March, May and September. Weak P (weak Fe) limitations indicate where P (Fe) is limiting but by a small amount relative to N or Fe (P) are near co-limiting (i.e., near co-limitation with difference between limitation factors < 0.25). Model climatology is ~~for~~ based on the 1980-2020 period.

MOM6-COBALT-IND12 reproduces the observed patterns in subsurface temperature and salinity in most of the basin (correlation coefficient r>0.99 and RMSE of 0.33°C and 0.07 psu). Specifically, the model simulates the contrast between the warm and salty waters in the northeastern Arabian Sea, the cold and ~~fresh waters~~ freshwaters along the model southern boundary, and the waters with intermediate temperature and salinity in the Bay of Bengal (Figure 12). The largest departures are found in the northern Arabian Sea where the model is biased cold and fresh (local bias between -0.8 and -0.3 °C and -0.4 to -0.1 psu~~,~~; Figure 12), suggesting that the Persian Gulf overflow is not as well simulated as other pathways.

We further examine ventilation pathways using vertical sections in the eastern Indian Ocean, the Gulf of Oman and the Arabian Sea (Figures 13 and 14). In the eastern Indian Ocean (at 90°E), the model reproduces the observed vertical structure, including the intermediate salinity found in the subsurface Bay of Bengal and the influence of fresher ITF waters in the southern part of the domain (at ∼1000 m depth and latitudes <5°S~~,~~; Figure 13). We note that the model only extends to 8°S, and therefore does not fully resolve the ITF centered at 5-10°S nor the Southern Equatorial Current at 10-20°S, but

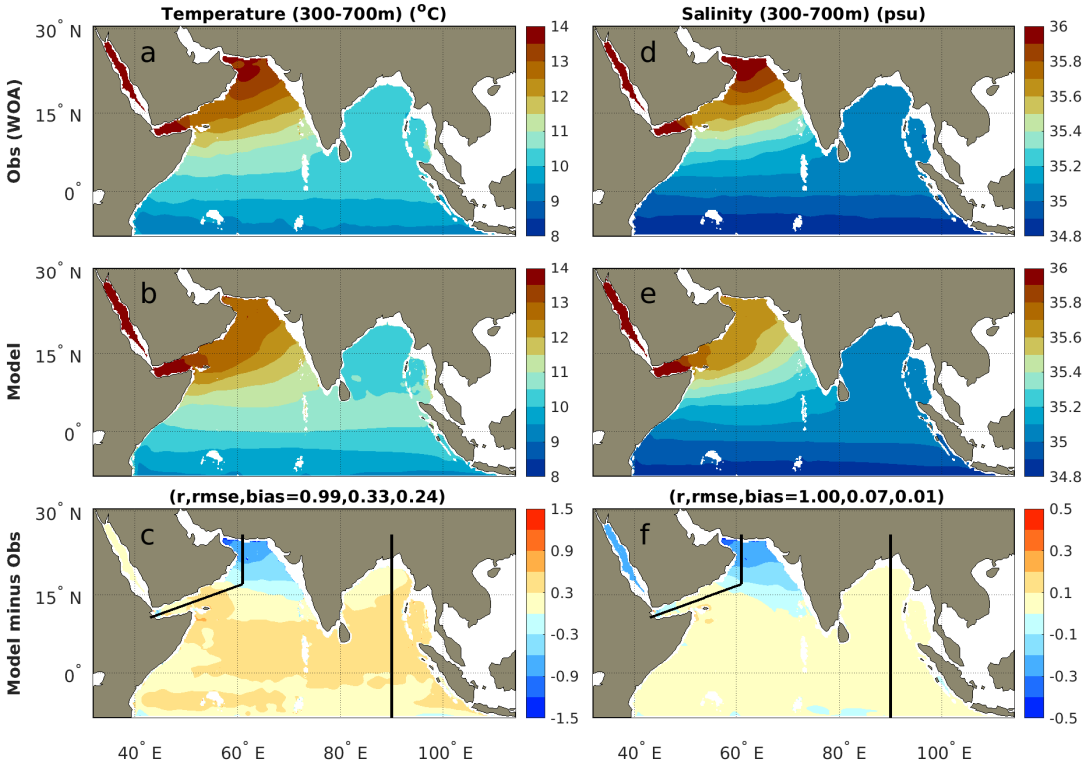

Figure 12. Annual mean subsurface (300-700 m depth) temperature and salinity in (a,d) observations, (b,e) MOM6-COBALT-IND12 model and (c,f) differences between model results and observations. Correlation coefficients r, RMSE and bias between the observed and model annual means are indicated. Temperature and salinity observations are from WOA18. Model results are averaged over the 1980-2020 period. Black lines indicate depth sections shown in Figures 13 and 14.

receives contributions from ITF waters and southern waters through the ~~boundary condition~~open boundary. The model presents, ~~however,~~ a slight bias in the vertical structure of the Bay of Bengal, with slightly colder and fresher near-surface waters and slightly warmer and saltier subsurface waters with a small influence on the stratification in the region (Figure 13c,f).

In the Gulf of Oman, observations show the plume of salty and warm Red Sea overflow waters (RSOW) that ~~flows~~ flow into the Gulf of Aden at a depth of 400-1000 m (>12°C and >36 psu~~,~~; Figure 14a,d). The model simulates the depth range of the plume but the lower part of the plume is biased salty and warm (local bias of 1 to 2°C and 0.2 to 0.8 psu~~,~~; Figure 14). This bias in the RSOW plume could come from biases in the source waters that overflow at the Bab-El-Mandeb Strait upstream, or from the misrepresentation of the plume mixing along the pathway. At the Bab-El-Mandeb Strait, we find that the model simulates remarkably well the volume transport of the three water masses flowing in and out of the Red Sea (Figure 15a). Specifically, the model simulates the observed outflow of RSOW that peaks in winter and drastically slows down in summer, the reversal of surface waters flowing into the Red Sea in winter and out of the Red Sea in summer, as well as the inflow of Gulf of Aden

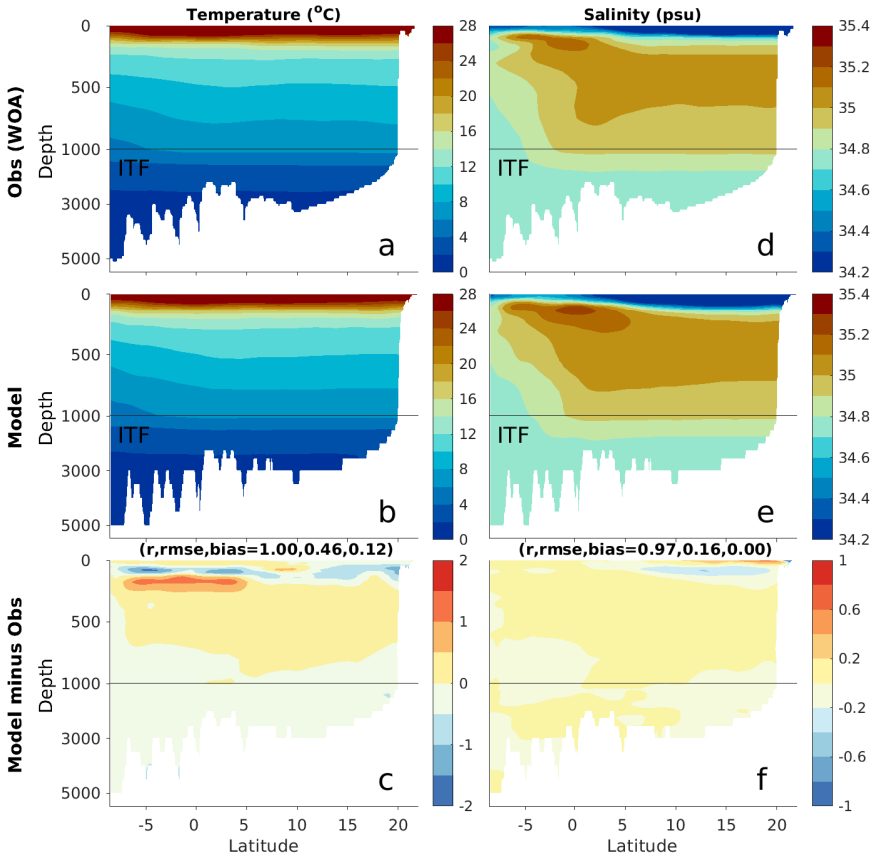

Figure 13. Depth section of annual mean temperature and salinity at 90°E in (a,d) observations, (b,e) MOM6-COBALT-IND12 model and (c,f) differences between model results and observations. Correlation coefficients r, RMSE and bias between the observed and model annual means are indicated. See location of section on Figure 12. Temperature and salinity observations are from the WOA18 (Table 2). Model results are averaged over the 1980-2020 period. Indonesian Througflow waters (ITF) are indicated.

intermediate waters (GAIW) that only takes place in summer. The model, however, shows a bias in the density of these water masses, ~~in particular in summer during which~~ particularly in summer when simulated RSOW are lighter and surface waters (and to some extent GAIW, although observations are sparse) are denser than observed (Figure 15b). This suggests there is insufficient mixing between the RSOW plume waters and the lighter (colder/fresher) waters above. This hypothesis is also supported by the structure of the temperature and salinity biases along the depth section showing a dipole of too salty / too warm waters in the lower part of the plume (800-1000 m depth) and slightly too fresh / too cold waters in the upper part of the plume (400-800 m depth~~,~~; Figure 14c,f). This bias is, however, confined to the plume in the Gulf of Aden, and seems to have a relatively small influence on the vertical structure further downstream, explaining the good agreement in subsurface temperature and salinity in the southwestern Arabian Sea (Figure 12).

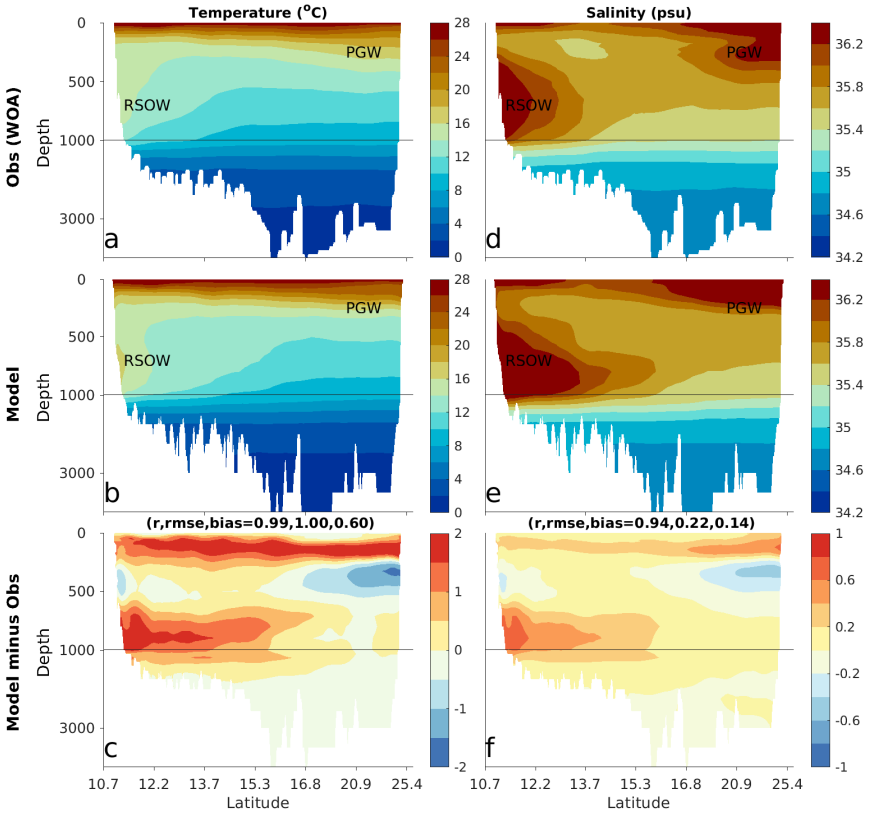

Figure 14. Depth section of annual mean temperature and salinity in the Gulf of Oman (southwest to northeast) and the Arabian Sea (south-north at 61°E) in (a,d) observations, (b,e) MOM6-COBALT-IND12 model and (c,f) differences between model results and observations. See location of section on Figure 12. Correlation coefficients r, RMSE and bias between the observed and model annual means are indicated. Temperature and salinity observations are from the WOA18 (Table 2). Model results are averaged over the 1980-2020 period. Persian Gulf Waters (PGW) and Red Sea Overflow Waters (RSOW) are indicated.

In the northern Arabian Sea, observations show that Persian Gulf waters (PGW) flow into the Arabian Sea at about 200-400 m depth (Figure 14). In MOM6-COBALT-IND12, however, PGW are too warm, too light and therefore enter the northern Arabian Sea at a too shallow ~~depth~~ depths of 100-200 m, leading to a cold/fresh bias at 200-400 m depth where PGW are located in observations and a warm-salty bias above (Figure 14). This trapping of the PGW close to the surface significantly changes the vertical structure of the northern Arabian Sea by reducing the stratification in the upper 200 m in the northern Arabian Sea.

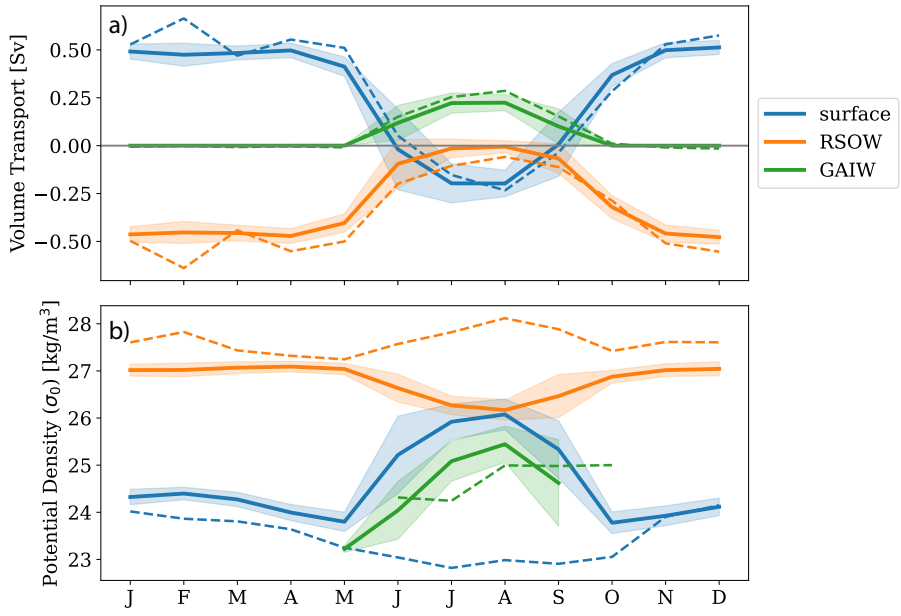

Figure 15. Seasonal evolution of the (a) volume transport and (b) potential density at the Bab-El-Mandeb Strait (between the Red Sea and the Gulf of Aden) in observations (dashed) and the model (solid). The three water masses are surface waters, Gulf of Aden Intermediate Waters (GAIW) and Red Sea Outflow Waters (RSOW). Observations and water mass detection method using flow direction are from Sofianos et al. (2002, see Table 2). Positive transport is into the Red Sea, negative transport into the Gulf of Aden. Model is averaged over 1980-2020. See details on water masses in ~~Methods~~Section 3.1.

5.2 Subsurface oxygen and oxygen minimum zones

Observed subsurface oxygen concentrations show the extent of the two ~~oxygen minimum zones (OMZ)~~ OMZs located in the Arabian Sea and Bay of Bengal (Figure 16). In the Arabian Sea, averaged subsurface oxygen concentrations (300-700 m) are lower than 10 μmol kg^{-1} in most of the region and reach suboxic values (<5 μmol kg^{-1}) around 15-20°N. In the Bay of Bengal, the OMZ is less intense with averaged subsurface concentrations of 10-20 μmol kg^{-1} and no suboxia. The equatorial subsurface is better oxygenated, but still characterized by relatively low averaged oxygen subsurface concentrations of 50-100 μmol kg^{-1} (Figure 16). Highest concentrations are found in the southwestern part, where the western boundary current supplies oxygen ~~originateing from the southern pathway~~ originating from the Southern Gyre and ITF (transported via the ~~Southern~~ South Equatorial Current).

The MOM6-COBALT-IND12 model reproduces the observed large scale patterns of subsurface oxygen (~~basin scale~~ basin-scale correlation coefficient r = 0.94 and RMSE = 16 μmol kg^{-1}~~,~~; Figure 16a). The largest biases are found in the eastern (down to -30 μmol kg^{-1}) and western (up to +40 μmol kg^{-1}) north equatorial band where the gradients in oxygen are strong. In this region, the model shows a high oxygen bias near the base of the thermocline (500–1000 m), coinciding with a low nitrate bias (not shown). This pattern points to either a misrepresentation of biological remineralization at depth or an

inaccurate representation of the relative contribution of the water masses forming the Central Waters supplying oxygen to this region. These waters originate from a blend of the ITF waters and southern-sourced Mode Waters. Previous studies have demonstrated that oxygen distribution in this region is highly sensitive to the relative contribution between these two sources (Ditkovsky et al., 2023). However, the scarcity of direct observations in this region limits our ability to conclusively attribute the model bias to either mechanism.

Yet, the most biogeochemically relevant bias is probably the overestimation of the extent and ~~degree~~ intensity of suboxic conditions in the northern Bay of Bengal, where the local difference in ~~model vs. observations of~~ modeled versus observed oxygen concentration ranges from -20 to -10 μmol kg^{-1}~~that leads to~~ , reflecting a much larger extent of suboxia in the model than in observations (Figure 16a). We evaluate the model ability to reproduce the volume of the OMZ as a function of the oxygen threshold chosen to define its boundary (i.e., volume bounded by oxygen concentrations from 5 to 150 μmol kg^{-1}, Figure 16b). At the basin scale, MOM6-COBALT-IND12 reproduces relatively well the observed OMZ volumes defined by thresholds above 30 μmol kg^{-1}, in particular the volume of hypoxic waters delimited by 60 μmol kg^{-1} (approximately 1×10^{16} m^3) and the volume of low oxygenated waters delimited by 100 μmol kg^{-1} (approximately 2×10^{16} m^3~~,~~; Figure 16b). ~~The~~ In contrast, the model overestimates the volume of suboxic waters delimited by 5 μmol kg^{-1} (0.17×10^{16} m^3 vs. 0.06×10^{16} m^3 in Bianchi et al. (2012) observations), mostly because of the large suboxic volume simulated in the Bay of Bengal (0.10×10^{16} m^3 vs. 0.00×10^{16} m^3 in observations~~,~~; Figure 16b). ~~In contrast~~Meanwhile, the volume of suboxic waters in the Arabian Sea is well represented (0.07×10^{16} m^3 vs. 0.06×10^{16} m^3). Finally, we note that the good match between observed and modeled hypoxic volumes is favored by the partial compensation of small biases in the Arabian Sea (model volume about 0.14×10^{16} m^3 lower than in observations) and the Bay of Bengal (model volume about 0.06×10^{16} m^3 higher than in observations~~,~~; Figure 16b).

6 Intraseasonal variability

We quantify the intraseasonal variability (ISV) in the surface ocean circulation using the intraseasonal standard deviation of the sea level anomaly (~~SLA, see Methods~~see Section 3.2). This diagnostic captures variability linked to all dynamical processes varying on intraseasonal time-scales, which includes mesoscale eddies and filaments, as well as meandering jets and planetary waves (Rossby and Kelvin waves). These intraseasonally varying features are key to the transport and mixing of physical and biogeochemical tracers, such as nutrients and oxygen, and to the onset and spatial extent of the seasonal phytoplankton blooms in the Indian Ocean (e.g., Resplandy et al., 2011, 2012; Lachkar et al., 2016; Rixen et al., 2020; Pearson et al., 2022; Vinayachandran et al., 2021)

Satellite observations show two hotspots where the intraseasonal variability in SLA exceeds 5 cm and can reach values higher than 10 cm (Figure 17a). The first hotspot is in the western Arabian Sea offshore Somalia and the Arabian Peninsula, where the high energy dynamics of the western boundary current and the presence of upwelling systems and complex coastal topography (capes/headland) promote the formation of large mesoscale eddies such as the Great Whirl ~~, Socotra Eddy and Southern Gyre~~ and Socotra Eddy (see section 4.2), and filaments extending from the Arabian Peninsula into the central Arabian Sea (e.g.,

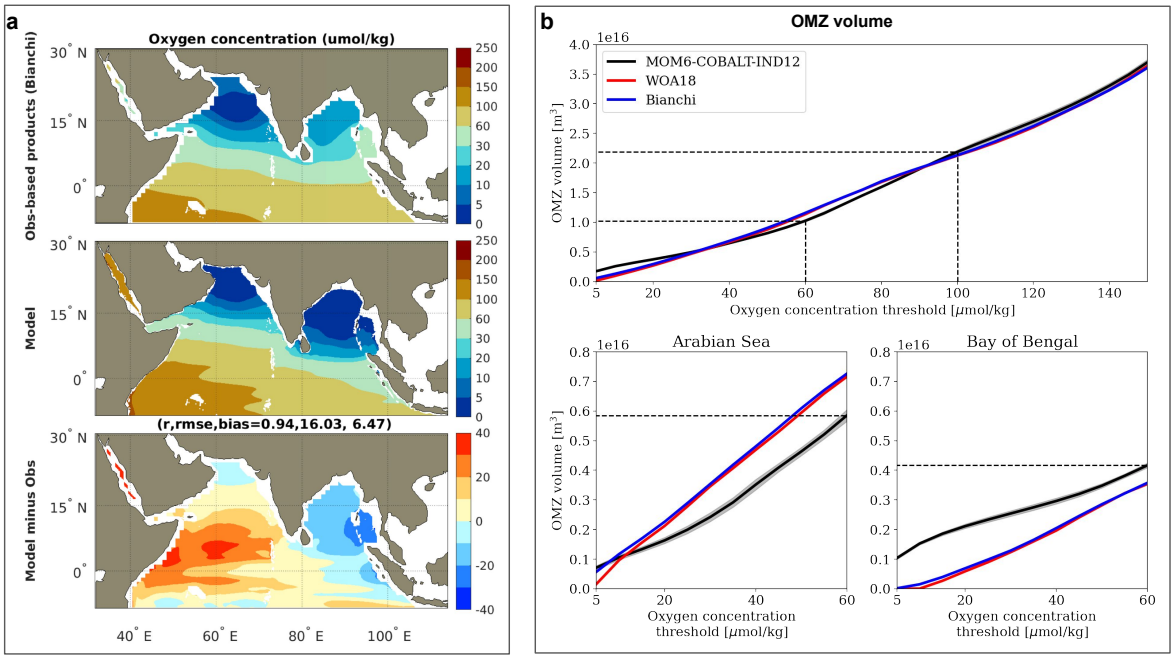

Figure 16. (a) Annual mean subsurface (300-700 m depth) oxygen concentrations in observations (top row, Bianchi et al., 2012), MOM6-COBALT-IND12 (middle row) and differences between model results and observations (bottom row). Correlation coefficients r, RMSE and bias between the observed and model annual means are indicated. (b) Observed and simulated ocean volume within a certain oxygen concentration threshold in the model domain (top row), the Arabian Sea and the Bay of Bengal (bottom row). Observations from Bianchi et al. (2012, in blue) and WOA18 (in red) differ mostly on the volume at low oxygen values. Grey shading indicates the 1-sigma model interannual variability. Model results are for the 1980-2020 period.

Beal and Donohue, 2013; Resplandy et al., 2011; Brandt et al., 2003; Wang et al., 2018). The second hotspot covers the central and western Bay of Bengal and extends south of Sri Lanka, and has been attributed to mesoscale eddies and Rossby waves generated in the coastal eastern Bay of Bengal that propagate westward into the central and western Bay of Bengal (Sengupta et al., 2001, 2007; Cheng et al., 2013). MOM6-COBALT-IND12 simulates the locations of the two hotspots of highest ISV in the western Arabian Sea and western Bay of Bengal, but the amplitude tends to be weaker than observed, with typical values of 3-8 cm in the model ~~vs.~~ versus 4-12 cm in the observations (Figure 17).

Other regions of relatively high observed ISV (>3 cm) include the mouths of major rivers, such as the Ganges-Brahmaputra, Irrawaddy-Sittang and Narmada-Tapti river systems (see Figure 1 for rivers location), coastal ocean waters along the eastern Bay of Bengal and eastern Arabian Sea, and the 5°N-10°N band in both the Arabian Sea and Bay of Bengal (Figure 17). ISV at the river mouths and the coastal ocean can largely be attributed to the ISV in river freshwater discharge

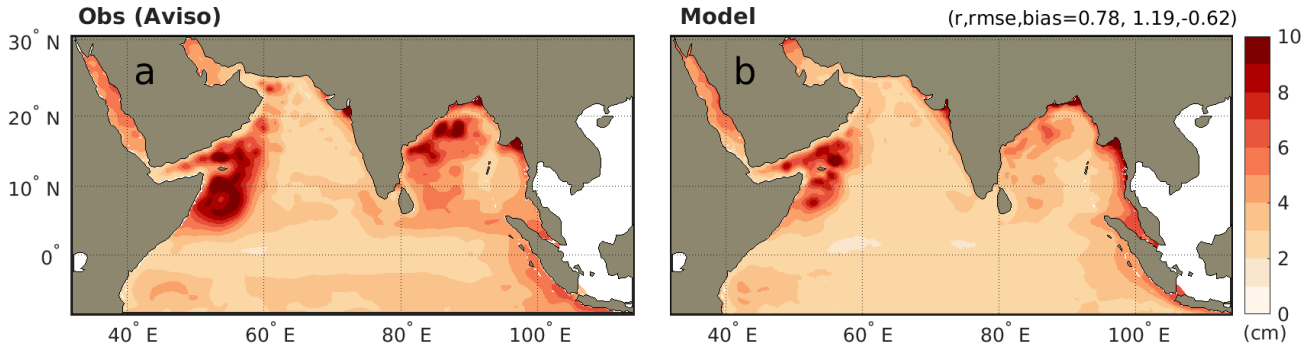

Figure 17. Intraseasonal variability (includes mesoscale eddy activity and wave-driven variability) quantified by the intraseasonal standard deviation of the sea level anomaly (SLA) in (a) ~~Aviso~~ AVISO satellite observations ~~,~~and (b) MOM6-COBALT-IND12. SLA over the 1994-2017 period was detrended using a linear regression and filtered using a 14-120 days band-pass filter.

~~(up to 50% of seasonal variability amplitude for the Ganges for instance, Jian et al., 2009)~~(up to 50% of seasonal variability amplitude for , tidal forcing and the propagation of coastal Kelvin waves (e.g., Nienhaus et al., 2012). MOM6-COBALT-IND12 reproduces relatively well the observed ISV in the coastal ocean and part of the ISV at river mouths. Finally, the intraseasonal variability in the 5°N-10°N band, which reaches 3 to 5 cm in the satellite-based estimate in response to the westward propagation of Rossby waves (Bruce et al., 1994; Shankar and Shetye, 1997; Vialard et al., 2009; Cheng et al., 2017), is also underestimated in the model (1-3 cm~~,~~; Figure 17). These underestimations might indicate the current spatial resolution of the model (1/12°) may still be insufficient for resolving these processes.

Figure 18 illustrates the influence of eddies and filaments on surface chlorophyll and phytoplankton production and their seasonality in the Arabian Sea, specifically in the first hotspot of ISV described above (western Arabian Sea and central Arabian Sea). The model reproduces ~~remarkably well~~ the fine-scale features structuring the winter and summer blooms. During the winter monsoon, fine-scale eddies (~ 20-50 km in diameter) shape the bloom occurring in the northern and central Arabian Sea (Figure 18a,b,e,f). This is consistent with the results of Resplandy et al. (2011), which showed that these fine-scale eddies ~~sustained~~ sustain the bloom by ~~transporting vertically and supplying nutrients~~ vertically transporting nutrients to the euphotic zone during early winter and by locally re-stratifying and alleviating light limitation during late winter when convection occurs (see section 4.2 and Figure 4 for mixed layer seasonality). During the summer monsoon, surface chlorophyll is highest in the coastal upwelling regions of Oman and Somalia in the early phase of the bloom (Figure 18c,g) and then extends offshore in long filaments wrapped around mesoscale eddies in the central Arabian Sea and around the Great Whirl in the late phase of the bloom (Figure 18d,h). The structure of the bloom here is also consistent with ~~Resplandy et al. (2011)~~ the findings of Resplandy et al. (2011), which showed that eddy-induced vertical transport supplied most of the nutrients in coastal waters during the early stage of the summer upwelling, while horizontal transport by filaments supplied nutrients to the central Arabian Sea. We note that the shape of the winter and summer eddies and filaments is well captured by the model, although their exact

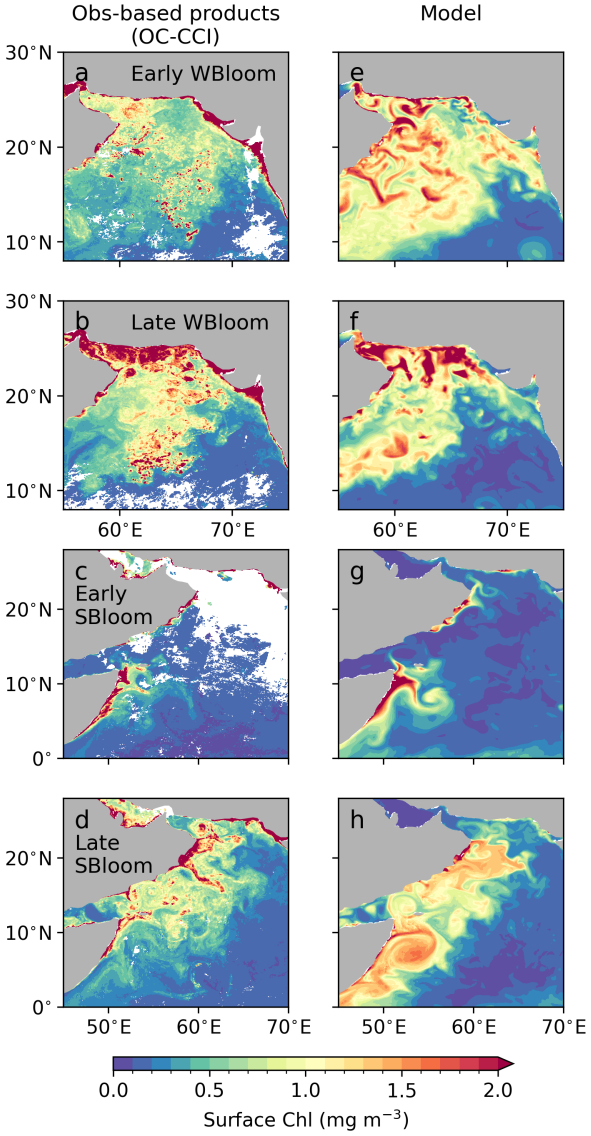

Figure 18. Fine-scale structures (eddies, filaments) revealed by surface chlorophyll in the OC-CCI ~~satelite~~ satellite product (~~left~~a-d) and the MOM6-COBALT-IND12 model (~~right~~e-h). Snapshots are for (a,e) early winter bloom (WBloom, Jan. 29, 2014), (b,f) late WBloom (Mar. 10, 2014), (c,g) early summer bloom (SBloom, Jun. 6, 2011) and (d,h) late SBloom (Oct. 4, 2011). OC-CCI images are 8-day composites and model images are 7-day averages (e-h).

location might not be the same. Indeed, we expect the model to reproduce the statistics of mesoscale structures (e.g., eddies and filaments) for a given season and region, but not necessarily their exact position. We also note that simulated surface chlorophyll concentrations are ~~higher~~ biased high in the model, in particular during the late summer monsoon (Figure 18d,h).

This is in line with the finding that chlorophyll is overestimated in the model, although primary productivity appears to be well simulated, likely due to the high contribution of large phytoplankton with high ~~chlorophyll to carbon~~ chlorophyll-to-carbon ratio (see section 4.5 and Figures 9,10).

7 Interannual Indian Ocean Dipole

The model reproduces the amplitude and zonal pattern of SST changes expected in response to the Interannual ~~Indian Ocean Dipole (IOD ,~~ IOD (r > 0.9~~, ;~~ Figure 19b-e~~, see panel ;~~ see Figure 19a for timing of positive and negative IOD phases). This includes the strong SST response in the eastern equatorial Indian Ocean, offshore Java and Sumatra, where the surface cools by -0.5 to -1°C during positive IODs and warms by +0.5 to +1°C during negative IODs~~;~~ , as well as the weaker response in the eastern and central equatorial Indian Ocean, where the ocean surface warms by +0.2 to +0.5°C during positive IODs and cools by -0.2 to -0.5°C during negative IODs. This SST signature of IODs is associated with anomalous winds and changes in thermocline depth along the equator (Saji et al., 1999; Webster et al., 1999; Currie et al., 2013). During positive IODs, easterly wind anomalies in the central Indian Ocean shallow the thermocline in the east and generate anomalously cold eastern SSTs. In the west these wind anomalies, in conjunction with Rossby waves, deepen the thermocline and produce anomalously warm western SSTs. During negative IODs, anomalous westerly winds lead to the ~~opposed~~ opposite east/west pattern in SST and thermocline depth. These SST signatures develop in boreal summer, peak in fall, and decay through winter.

Figure 20 focuses on this zonal contrast introduced by the IOD~~by comparing~~ , through a comparison of observed and modeled interannual anomalies in SST and thermocline depth at two equatorial Indian Ocean sites: one eastern mooring offshore Sumatra (95°E, 5°S) and one western mooring in the Seychelles-Chagos thermocline ridge (57°E, 4°S). We use observations from the *in-situ* ~~Research Moored Array for African-Asian-Australian Monsoon Analysis and Prediction (RAMA)~~ RAMA that we complement with ~~satellite SST (OISST)~~ OISST data and Argo float-based thermocline depth (see Table 2). MOM6-COBALT-IND12 reproduces particularly well the timing and amplitude of interannual variations in SST (r of 0.78-0.90 with RAMA and 0.75-0.79 with OISST) and in thermocline depth (r of 0.75-0.82 with RAMA and 0.73-0.84 with Argo) at both RAMA stations (Figure 20), including the asymmetry in the response between IOD phases (Hong et al., 2008b, a; Cai et al., 2013; Nakazato et al., 2021). At the eastern station, the thermocline deepens by 20-30 m and SSTs increase by +0.5 to +1°C during negative IODs~~, while~~ . In contrast, the thermocline only shallows by 10-20 m and SSTs generally decrease by less than -0.5°C during positive IODs, except during the strong positive IOD of 2019 during which SSTs cooled by more than 1.5°C in both observations and models. The model also captures interannual variations observed at the western station ~~(note that~~ Figure 20. While IOD-driven variability is ~~captured~~ present at the western mooring~~but~~ , its influence is likely weaker compared to other sources of variability~~at the western site), i.e. deeper thermocline /~~ . Nevertheless, the model reproduces the associated variabilities, including a deeper thermocline and cooler SSTs during negative IODs, and shallower thermocline ~~/~~ and warmer SSTs during positive IODs (Figure 20).

The wind anomalies associated with the IOD also produce equatorially trapped Kelvin waves that travel east towards Sumatra and Java, impinge on their coasts and continue traveling counterclockwise around the rim of the northern Indian Ocean, thereby

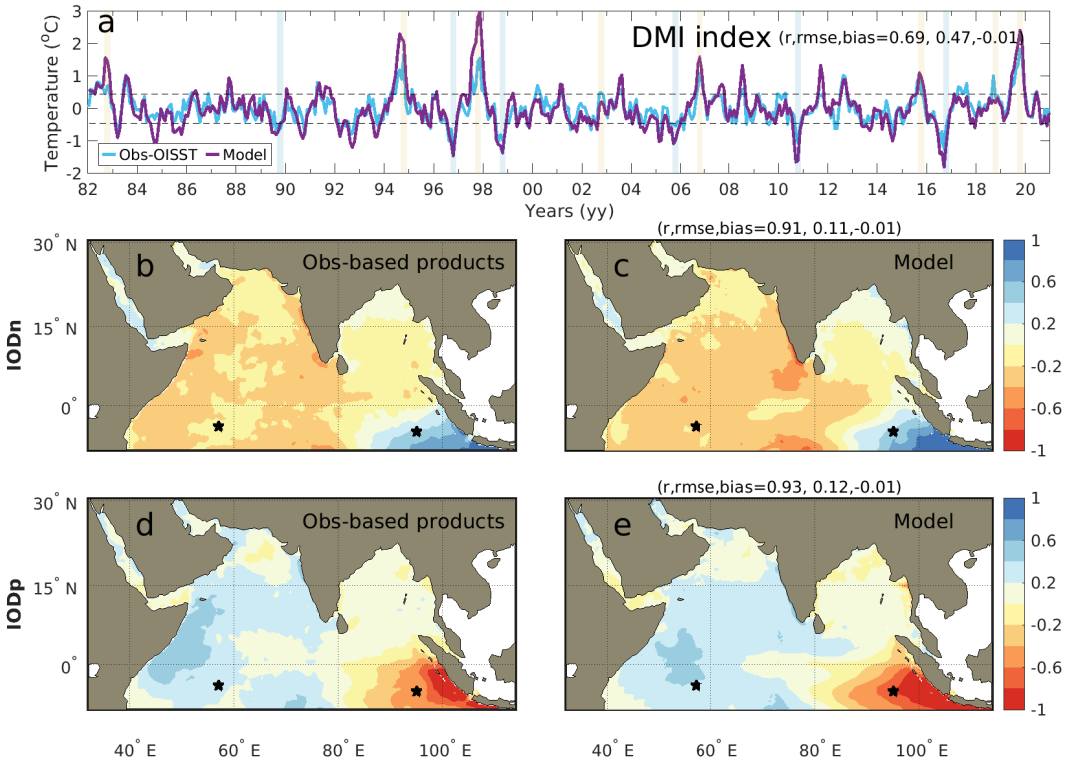

Figure 19. Interannual variability associated with the Indian Ocean Dipole (IOD). (a) Dipole mode index (DMI) which quantifies the intensity of the IOD phases; (b,c) SST composites during IOD negative phases (IODn) in observations and MOM6-COBALT-IND12 model; (d,e) SST composite during IOD positive phases (IODp) in observations and MOM6-COBALT-IND12 model. Composites are for September-to-November months of positive (1982, 1994, 1997, 2002, 2006, 2015, 2018, 2019) and negative (1989, 1996, 1998, 2005, 2010, 2016) IODs. SST observations are from OISSTv2.1 (see Table 2). Black stars indicate the positions of two Research Moored Array for African-Asian-Australian Monsoon Analysis and Prediction (RAMA) moorings used in Figure 20.

modulating the seasonal upwelling/downwelling motions described in section 4.3 above (see details on coastal Kelvin wave modulation by IOD in Aparna et al., 2012; Suresh et al., 2018; Pearson et al., 2022). As shown in Figure 7, the model reproduces the coastal SLA interannual anomalies associated with IOD phases. In particular, it simulates the upwelling anomaly observed between September and January during positive IOD phases along the coasts of the Bay of Bengal (arrows for waves IX and X; SLA internanual anomalies of -12 to -5 cm), and the downwelling anomaly observed during negative IOD phases (~~same months,~~ arrows for waves XI and XII, same months; SLA internanual anomalies of +5 to +12 cm~~,~~; Figure 7). The model also simulates the weaker ~~and opposed in sign SLA anomalies~~ SLA anomalies of opposite sign (compared to the Bay of Bengal) observed along the coasts of the Arabian Sea (SLA interannual downwelling anomaly of +2 to +5 cm during positive IODs, and upwelling anomaly of -2 to 0 cm during negative IODs~~,~~; Figure 7).

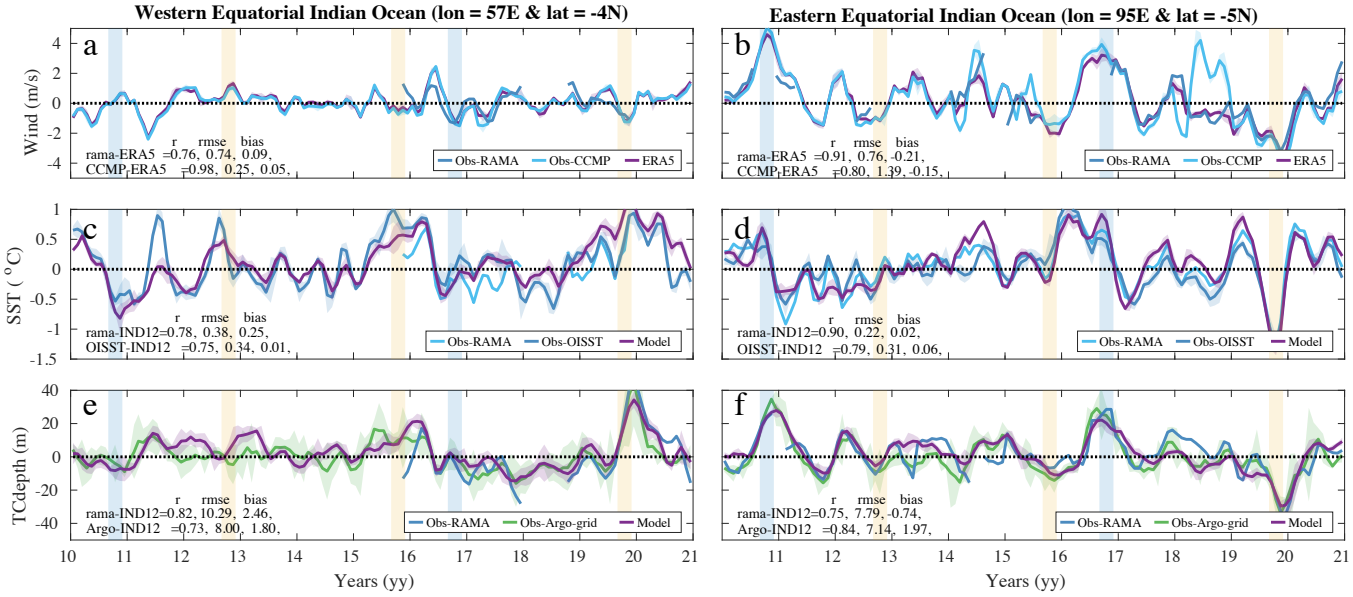

Figure 20. Interannual variability associated with the Indian Ocean Dipole (IOD) at two RAMA moorings in western (~~left column~~a,c,e: 57°E, 4°S) and eastern (~~right column~~b,d,f: 90°E, 5°S) equatorial Indian Ocean. ~~Top row~~panels (a,b): zonal wind stress from observations (RAMA mooring and CCMP satellite) and the ERA5 reanalysis used to force MOM6-COBALT-IND12; ~~middle row~~(c,d): SST in observations (RAMA moorings and OISSTv2.1) and in MOM6-COBALT-IND12; ~~bottom row~~(e,f): thermocline depth (TCdepth) is calculated as ~~XXX~~the depth of the 20 °C isotherm. Positive and negative IODs are indicated by orange and blue shading. Correlation coefficients r, RMSE and bias between the observed and reanalysis or model time-series are indicated in each panel. Positions of the two RAMA moorings are shown by black stars in Figure 19.

IOD phases are associated with biogeochemical signatures visible at the basin scale in satellite ocean color observations (Murtugudde and Busalacchi, 1999; Wiggert et al., 2009; Currie et al., 2013). Figure 21 compares composites of integrated primary productivity ~~(PP)~~ anomalies from the CbPM satellite and MOM6-COBALT-IND12 in boreal fall (September-November). Negative IOD phases are characterized by negative ~~PP~~ primary productivity anomalies in the eastern equatorial Indian Ocean (-150 to -300 mg C m^{-2} d^{-1} offshore Sumatra~~,~~; Figure 21a) due to the depressed thermocline and associated nutricline and weaker ~~upwelling~~/upwelling-favorable wind (Figure 20), and positive ~~PP~~ primary productivity anomalies in the western equatorial Indian Ocean (+50 to +150 mg C m^{-2} d^{-1} offshore Somalia) due to the shallower thermocline ~~/~~and nutricline (Figure 20). Negative IODs are also associated with strong positive ~~PP~~ primary productivity anomalies around the tip of India (> +200 mg C m^{-2} d^{-1}) associated with the wave-driven shoaling of the thermocline ~~/~~and nutricline (Figure 7) and positive anomalies in most of the Arabian Sea (Figure 21a). The response to positive IODs mirrors the response of negative IODs in the equatorial Indian Ocean, with positive anomalies observed in the eastern equatorial Indian Ocean and negative anomalies in the western equatorial Indian Ocean and around the tip of India (Figure 21b). We note, however, that the ~~PP anomaly~~ primary productivity anomalies in the northern and central Arabian Sea are positive ~~in~~ during both negative and positive ~~IODs~~IOD phases. The

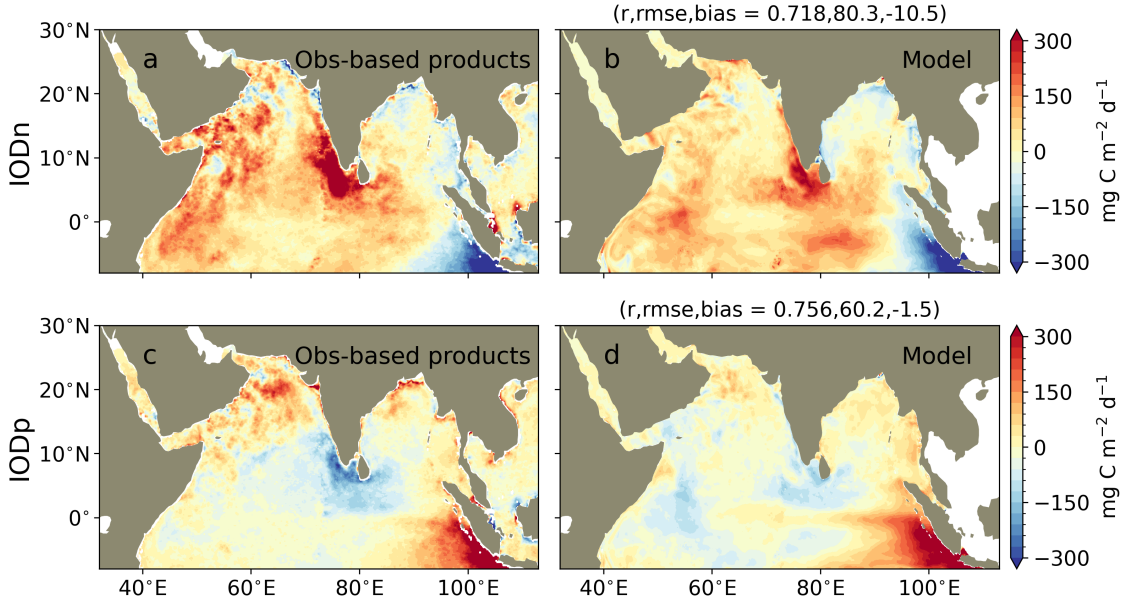

Figure 21. Integrated net primary productivity (PP) anomaly associated with the Indian Ocean Dipole (IOD). September-to-November PP composites during (a-b) IOD negative phases (IODn) and (c-d) IOD positive phases (IODp) in ~~observations~~ observation-based product and MOM6-COBALT-IND12. Composites are for ~~September-to-~~ September to November months available in CbPM satellite product for positive (2002, 2006, 2015, 2018, 2019) and negative (2005, 2010, 2016) IODs (see Table 2 for details on data).

model captures remarkably well the pattern and sign of the observed ~~PP~~ primary productivity anomalies during both negative and positive IODs (correlation coefficient r > 0.7), although the amplitude of the anomaly is slightly lower in the model than in the CbPM satellite product (RMSE of 60 to 80 mg C m^{-2} d^{-1}, bias of -1.5 to -10.5 mgC m^{-2} d^{-1}~~,~~; Figure 21c-d). ~~The amplitude of the PP~~ On the one hand, the model–observation discrepancy in primary productivity anomaly amplitude may stem from weak nutrient variability associated with the shallow MLD. On the other hand, the amplitude of the primary productivity anomalies obtained from satellite products ~~are, however,~~ remains uncertain. For instance, the ~~PP~~ primary productivity anomaly composites obtained from another satellite product (CAFE) show similar patterns but with an amplitude that is about half of the CbPM satellite product (~~Figures 21and ?? panels aand~~ Figure 21a,c and Appendix Figure Aa,c). The amplitude of the anomaly in the model ~~essentially sits in~~ sits between the two satellite products (RMSE of 60-80 mg C m^{-2} d^{-1} in both cases and absolute bias between -10.5 and +24 mg C m^{-2} d^{-1}~~, see Figures 21 and ??).~~ ; see Figure 21 and Appendix Figure A). Given the discrepancies among observational datasets, the model likely provides a reasonable estimate of primary productivity variability. Nevertheless, additional in situ observations are needed to more accurately constrain the true primary productivity response to the IOD.

8 Discussion and conclusions

We developed a regional ocean biogeochemical model at In this study, we configured, customized, and validated a high-resolution (1/12° horizontal resolution) regional ocean biogeochemical model (MOM6-COBALT-IND12 v1.0) that captures most key features of for the northern Indian Ocean. Specifically, we adjusted river discharge rates and nutrient loadings in the Bay of Bengal according to observational constraints, significantly improving simulations of river plume dynamics and surface salinity. Additionally, we enhanced lithogenic particle fluxes from rivers, adjusted detritus sinking rate, and refined the parameterization of the nitrogen cycle, resulting in better representations of subsurface oxygen distributions and suboxic conditions. These improvements collectively allow the model to capture most key aspects of biogeochemical and physical processes in the northern Indian Ocean dynamics.

At the basin scale, the MOM6-COBALT-IND12 model simulates the contrast between the Arabian Sea – characterized by high evaporation, inflow from the saline marginal seas (Red Sea and Persian Gulf) and high upper ocean salinity – and the Bay of Bengal – characterized by high precipitation, high river runoffs and low upper ocean salinity. On seasonal time-scales, the model captures the monsoonal reversal in ocean circulation, including the development of the Great Whirl and wind-driven summer coastal upwelling systems along the western boundary, the winter convective mixing in the northern Arabian Sea, as well as the propagation of upwelling and downwelling coastal Kelvin waves along the equatorial waveguide and the rim of the northern Indian Ocean. On intraseasonal time-scales, the model also reproduces the hotspots of variability associated with eddies, filaments and planetary waves, and on interannual time-scales the east-west variability in the thermocline introduced by the Indian Ocean Dipole (IOD). IOD. This strong physical performance likely stems from the effective parameterizations of surface heat and momentum fluxes, combined with well-constrained surface forcing fields derived from ERA5 reanalysis.

The good agreement between observed and modeled physical features largely explains the model's ability to reproduce the provides a foundation for accurately simulating the ocean biogeochemical and biological response. This includes the intensity and timing of the seasonal blooms triggered by monsoonal circulation changes and modulated by intraseasonal features such as eddies and filaments, and interannual IOD phases. Specifically, the model reproduces the summer bloom associated with coastal upwelling systems and their extension offshore in mesoscale filaments, as well as the winter bloom associated with convective mixing and modulated by fine-scale eddies (Lévy et al., 2007; Resplandy et al., 2011, 2012; Mahadevan, 2016; Lachkar et al., 2016; Rixen . It (Lévy et al., 2007; Resplandy et al., 2011, 2012; Mahadevan, 2016; Lachkar et al., 2016; Rixen et al., 2019a; Vinayachandran et al., 20 . These biogeochemical improvements reflect the targeted model development efforts outlined above. The model also captures the patterns and amplitude of the phytoplankton changes expected in response to the IOD positive and negative phases. This includes the modulation of the production in the equatorial region, the Arabian Sea and around the tip of India, although we note these patterns are difficult to generalize to all IOD events, as illustrated by Wiggert et al. (2009) who found a very different response in surface chlorophyll between the positive IOD phases of 1997 and 2006. . As illustrated by Wiggert et al. (2009), the chlorophyll responses vary with IOD intensity-for instance, concentrations in the Arabian Sea decreased during the 1997 event but increased during the 2006 event.

The comparison (Appendix Figure A8) between MOM6-COBALT-IND12 and the global model of Liao et al. (2020) demonstrates that the regional model more realistically captures high-frequency variability in SSH, mesoscale dynamics, meandering jets, and planetary waves (Rossby and Kelvin waves). These features significantly influence nutrient and oxygen transport and

mixing, as well as the timing and spatial patterns of seasonal phytoplankton blooms across the Indian Ocean. Our regional configuration also notably improves the representation of marginal sea outflows, particularly from the Red Sea, where global models typically overestimate overflow strength. Furthermore, targeted parameter adjustments–including river discharge, nutrient load, detritus sinking rate, and nitrogen cycle parameterization–improve dissolved oxygen simulations in both the Arabian Sea and the Bay of Bengal. Collectively, these refinements, substantially improve the accuracy and reliability of physical and biogeochemical processes simulated by our regional model.

During the ~~development~~ setup and customization of the MOM6-COBALT-IND12 v1.0 model, we identified a series of physical and biogeochemical parameters and forcings that influenced the model simulation and led to a significant improvement of the results (see details in section 2). One of the ~~factor~~ factors that influenced our results ~~was~~ were river discharge and nutrient loadings, especially in the Bay of Bengal which hosts major river systems such as the Ganges, Brahmaputra, Irrawaddy and Sittang rivers. A first version of the model used the river inputs from the Japanese 55-year Reanalysis ~~(JRA-55, Kobayashi et al., 2015)~~ (JRA55-do, Kobayashi et al., 2015) instead of the modified GloFAS product presented in this study. ~~We, however,~~ However, we found systematic biases in the timing, amplitude and variability of the riverine discharge in ~~JRA~~JRA55-do. These biases include a systematic delay of 1-2 months in the annual maximum discharge and a lower intraseasonal variability (~~Figure Appendix~~ Appendix Figure A1), which led to biases in river plume dynamics and ~~sea surface salinity~~ SSS in the northern Bay of Bengal and the eastern Arabian Sea, in line with observations showing that riverine discharge timing and variability are critical to salinity patterns and plume dynamics Li et al. (2021). In addition to river discharge, we modified nutrient loadings to match available observational constraints which was important to reproduce productivity patterns in the coastal Bay of Bengal. We note that the influence of riverine inputs could be further improved by accounting for the anthropogenic increase in riverine nutrient supply (MOM6-COBALT-IND12 v1.0 includes nutrient inputs equivalent to year 2000 from Mayorga et al., 2010), which would likely introduce a long-term trend in coastal primary productivity and oxygen concentrations in the vicinity of large river systems.

While ~~this~~ the MOM6-COBALT-IND12 v1.0 configuration is remarkably successful at capturing many of the features and observed variability of the northern Indian Ocean, there are still some areas where there is potential for improvement. The main model bias is the larger horizontal extent and volume of suboxia (oxygen concentrations < 5 μmol kg^{-1}) simulated in the Bay of Bengal. This bias is a well known limitation of ocean and Earth system models in this region (e.g., Bopp et al., 2013; Schmidt and Eggert, 2016; Ditkovsky et al., 2023). The advective supply of oxygen to the thermocline in the Bay of Bengal is ~~a shadow zone, where ventilation and oxygen supply by ocean circulation are expected to be weak, but~~ weak, but we expect low oxygen demand to prevent the formation of suboxic waters. However, the subsurface oxygen biological demand is likely too high in the model. Notably, this bias in oxygen in the Bay of Bengal was larger in a prior version of the model~~but part of it~~, and was mitigated by adjusting some of the model parameters. A first set of changes focused on riverine lithogenic fluxes. The increased influx of riverine lithogenic material by an order of magnitude for major rivers and about 50% for small rivers protects more particulate organic matter from remineralization due to the ballasting effect, significantly reducing oxygen consumption in the water column. A higher total river input of lithogenic material in the Bay of Bengal resulted in a greater reduction in oxygen consumption compared to the Arabian Sea. A second set of changes focused on detritus sinking velocities

and burial. The detritus sinking velocity was increased by 20% to match sediment trap observations in the region (Rixen et al., 2019b) and the fraction of material that reach the ocean floor and is buried was also increased to match the observation-based reconstruction of ~~LaRowe et al. (2020)~~LaRowe et al. (2020). These modifications reduced remineralization and oxygen consumption in the subsurface and at depth, further reducing the bias in the size and volume of the Bay of Bengal OMZ, while having a relatively small impact on the Arabian Sea OMZ core where oxygen is entirely depleted. The impact of these modifications are consistent with findings from Luo et al. (2024) and Al Azhar et al. (2017), who showed that fast-sinking detritus reduced oxygen consumption and shrank OMZs, expanding oxygenated regions at the OMZ boundaries. A third set of modifications focused on the representation of nitrogen cycling in low oxygen environments. These changes allowed ~~for instance~~ denitrification at oxygen concentrations up to 4 μmol kg^{-1} ~~(instead of 0.8 μmol kg^{-1}, Paulmier and Ruiz-Pino, 2009)~~ (instead of 0.8 μmol kg^{-1}; Paulmier and Ruiz-Pino, 2009), which would promote the use of nitrate for oxidation instead of oxygen and therefore reduce oxygen consumption in suboxic environments. ~~Yet, these three set of changes were not sufficient to~~

The three sets of changes described above did not entirely remove the ~~bias in oxygen concentration in~~ model low oxygen bias in the Bay of Bengal. One limitation of the COBALTv2 biogeochemical model is that it only includes one sinking detritus, which limits our ability to reproduce spatial contrasts in detritus sinking speed. ~~Rixen et al. (2019b)~~ Rixen et al. (2019b) showed that detritus sinking velocities are indeed higher in the Bay of Bengal due to the ballasting effect of riverine mineral particles. In addition, ~~Al Azhar et al. (2017)~~ Al Azhar et al. (2017) showed that simulating this contrast between the Arabian Sea where detritus are sinking relatively slowly and the Bay of Bengal where detritus are sinking faster improved the representation of the OMZs in an ocean model. Looking ahead, adding multiple detritus pools with different sinking velocity might be a way to improve the OMZ in the Bay of Bengal. Despite these model limitations, it is important to note that uncertainties remain regarding the strength of suboxia in the Bay of Bengal. Recent observations from Argo floats and ship-based in situ measurements have reported lower oxygen concentrations in the Bay of Bengal than those presented in the WOA dataset, including nanomolar-level oxygen conditions (Bristow et al., 2017; Udaya Bhaskar et al., 2021). These findings suggest that the true extent and intensity of hypoxia in the Bay of Bengal remain uncertain, making it difficult to definitively assess the magnitude of the model bias in this region.

In addition to the ~~oxygen minimum zones~~OMZs, another area that we are considering for future work is the high bias in surface chlorophyll concentration simulated in the model compared to satellite products, in particular ~~in~~ near and offshore summer upwelling systems. An extensive compilation of *in-situ* primary productivity measurements shows that the model successfully captures the seasonality in productivity. This strongly suggests that the bias is limited to the phytoplankton chlorophyll content without influencing its carbon content. This bias in chlorophyll is likely due to an overestimation of the contribution of large phytoplankton (higher chlorophyll to carbon ratio) compared to small phytoplankton (lower chlorophyll to carbon ratio), and is therefore expected to have a relatively small impact on nutrient uptake by phytoplankton and oxygen consumption associated with the remineralization of the organic matter in the water column. This bias in chlorophyll content might be mitigated in the future when using the COBALT version 3 biogeochemical module which incorporates four phytoplankton groups instead of three, including a medium size class that allows for a smoother transition from small to large, and accounts for photoaccli-

mation and photoadaptation which is critical in simulating chlorophyll ~~(Stock et al., 2024)~~(Stock et al., 2025). While this bias complicates comparisons between model and satellite chlorophyll data, it is primarily confined to chlorophyll and has a limited impact on the model's ability to represent regional nutrient, carbon, and oxygen dynamics key to marine ecosystems.

With these results, we are confident that MOM6-COBALT-IND12 is an effective and versatile model to tackle applications in physical and biogeochemical oceanography, as well as applications to marine resources and management on timescales of weeks to decades in northern Indian Ocean. This configuration is particularly well-suited for evaluating the impacts of natural variability and anthropogenic activities on key environmental variables that influence marine resources. One key application is evaluating the risk of coastal hypoxia——an increasingly pressing issue for local populations and the blue economy, including fisheries, in the region (Naqvi et al., 2009; Vallivattathillam et al., 2017; Pearson et al., 2022; Naqvi, 2021, 2022). Despite its importance, coastal hypoxia is often only marginally addressed in global studies, which focus primarily on hypoxia events in Europe and North America (Breitburg et al., 2018; Deutsch et al., 2024). MOM6-COBALT-IND12 is ideally suited to investigate the physical and biological drivers of coastal hypoxia in the northern Indian Ocean, as well as their spatio-temporal variability. This capability is essential for predicting hypoxic events and informing effective management strategies to safeguard marine ecosystems and coastal economies.

Code availability. The source code for the model components is available at https://doi.org/10.5281/zenodo.14184011 (Liao et al., 2024a). The model parameter files and preprocessed forcing data used for the Indian Ocean configuration have been archived at https://doi.org/10.5281/zenodo.14171404 (Liao et al., 2024b). MOM6 is developed openly, with its Git repositories hosted at https://github.com/mom-ocean/MOM6 and https://github.com/NOAA-GFDL/MOM6. These platforms enable users to obtain the latest and experimental versions of the source code, report issues, and contribute new features.

Data availability. The model output analyzed in this study is available at https://doi.org/10.5281/zenodo.14183131 (Yang et al., 2024).

Author contributions. Conceptualization: LR. Data curation: EL, FY, YZ. Formal analysis: EL, FY, YZ, SD, MM, LR. Funding acquisition: LR, CS. Investigation: EL, FY, YZ, SD, MM, LR. Methodology: EL, JP, SD, FY, YZ, ACR, RH, CS, LR. Software: EL, JP, SD, FY, YZ, ACR, MM, RH, CS. Supervision: LR, RH, CS. Visualization: EL, FY, YZ, SD, MM. Writing – original draft: LR. Writing – review and editing: LR, SD, FY, YZ, CS, RH.

Competing interests. No competing interests

Acknowledgements. This work was supported by the NOAA Climate Program Office Award No. NA21OAR4310119, and the High Meadows Environmental Institute Climate, Chemistry and Life in the Indian Ocean Initiative and the NSF CAREER award no. 2042672. The bio-Argo data were collected and made freely available by the International Argo Program and the national programs that contribute to it. (https://argo.ucsd.edu, https://www.ocean-ops.org). The Argo Program is part of the Global Ocean Observing System.

Appendix A: Supplementary Figures

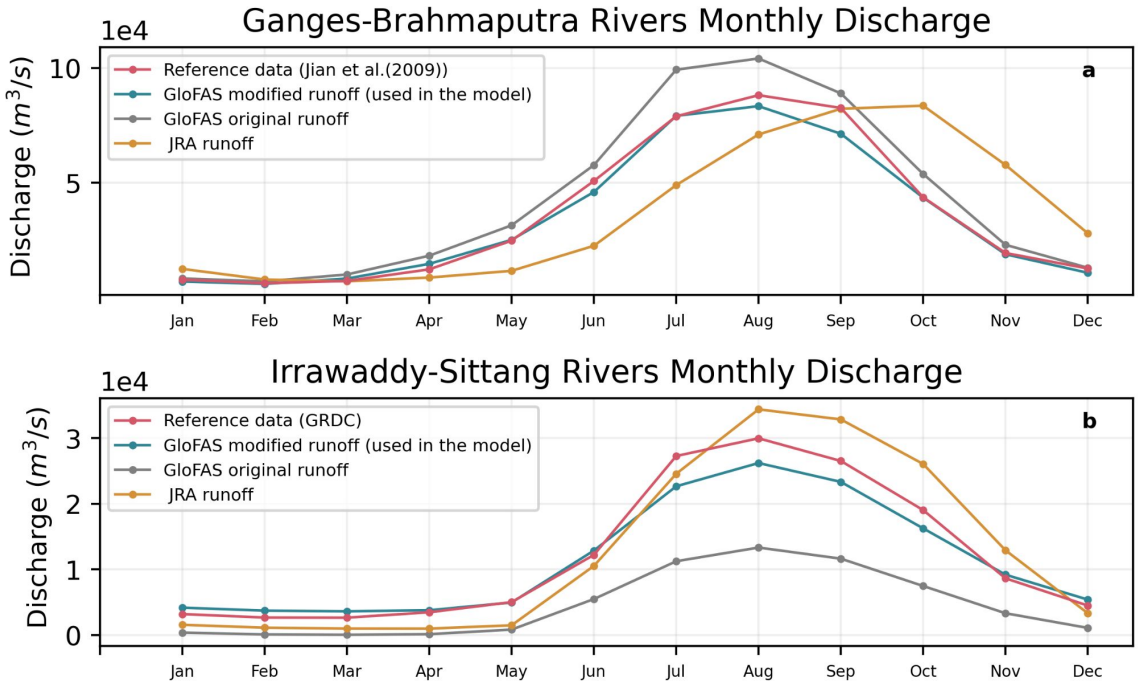

Figure A1. Water discharge in the (a) Ganges-Brahmaputra and (b) Irrawaddy-Sittang river systems from observations (red), the raw GloFAS-ERA5 runoff product (grey, Harrigan et al., 2023, 2020), the modified GloFAS-ERA5 runoff product used to force MOM6-COBALT-IND12 (teal, $0.75 \times$ GloFAS-ERA5m^3/s for Ganges-Brahmaputra and $1.7 \times$ GloFAS-ERA5 $+ 3564\,\mathrm{m}^3/\mathrm{s}$ for Irrawaddy-Sittang), and in the JRA55-do reanalysis (orange, Tsujino et al., 2018). Observations are from Jian et al. (2009) for Ganges-Brahmaputra and Recknagel et al. (GRDC, 2023) for Irrawaddy-Sittang. We note that the raw GloFAS-ERA5 can overestimates or underestimate the discharge compared to observations, while JRA55-do presents a systematic 1-2 months delay in the timing of the seasonal peak runoff.

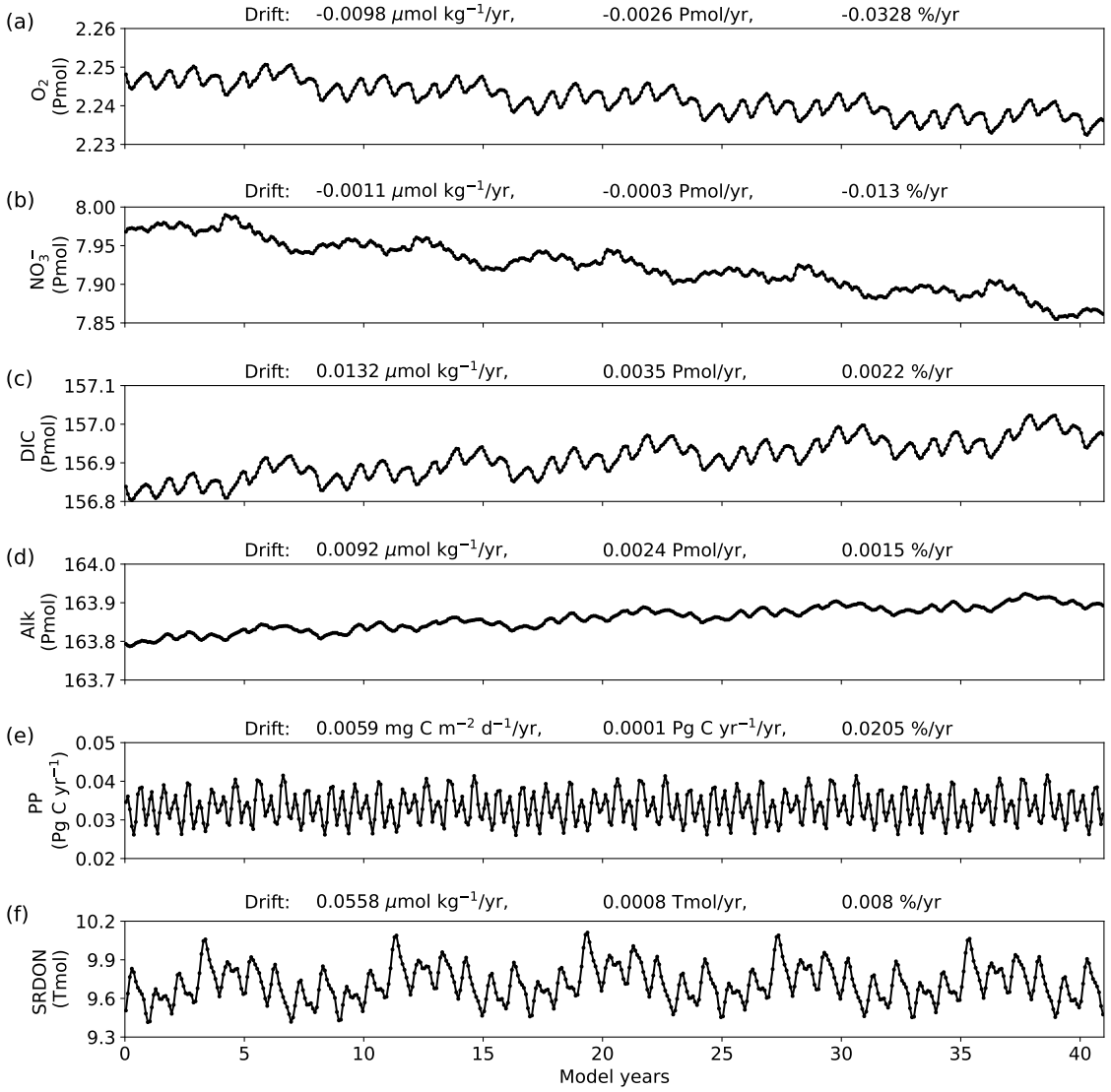

Figure A2. Model ~~time-series~~ time series and drift evaluated as the linear trend after the ~~32 year~~ 32-year spin-up in the control simulation with constant forcing: (a) total oxygen (O_2), (b) total nitrate (NO_3^-), (c) total dissolved inorganic carbon (DIC), (d) total alkalinity (Alk), (e) total vertically integrated primary productivity (PP) and (f) total semi-refractory dissolved organic nitrogen (SRDON). Drifts are indicated above each panel and are all $< 0.05\%$.

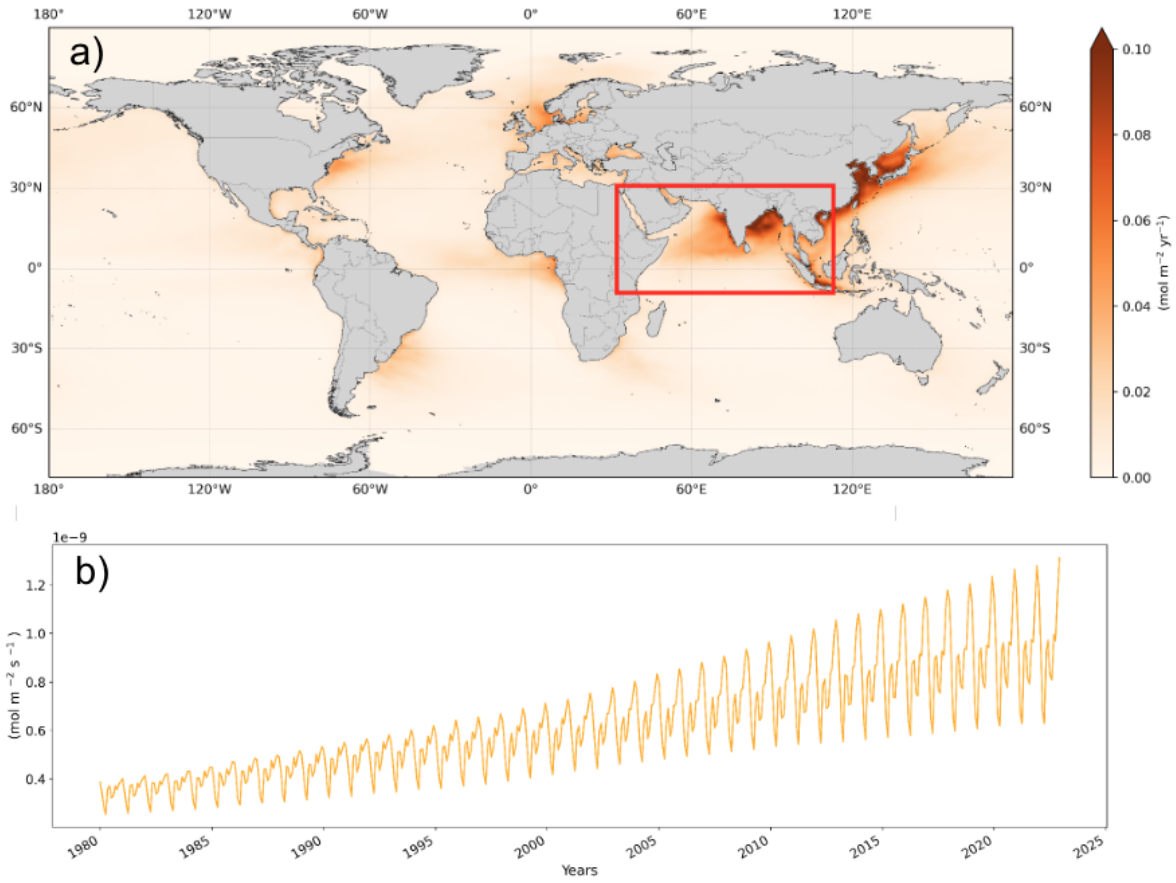

Figure A3. Atmospheric deposition of nitrogen from the earth system model ESM4.1 used to force MOM6-COBALT-IND12: (a) spatial distribution in year 2020, and (b) temporal evolution averaged over the model domain ~~calucalted~~ calculated using a 15-year monthly moving average (see ~~methods~~Section 2.4.2).

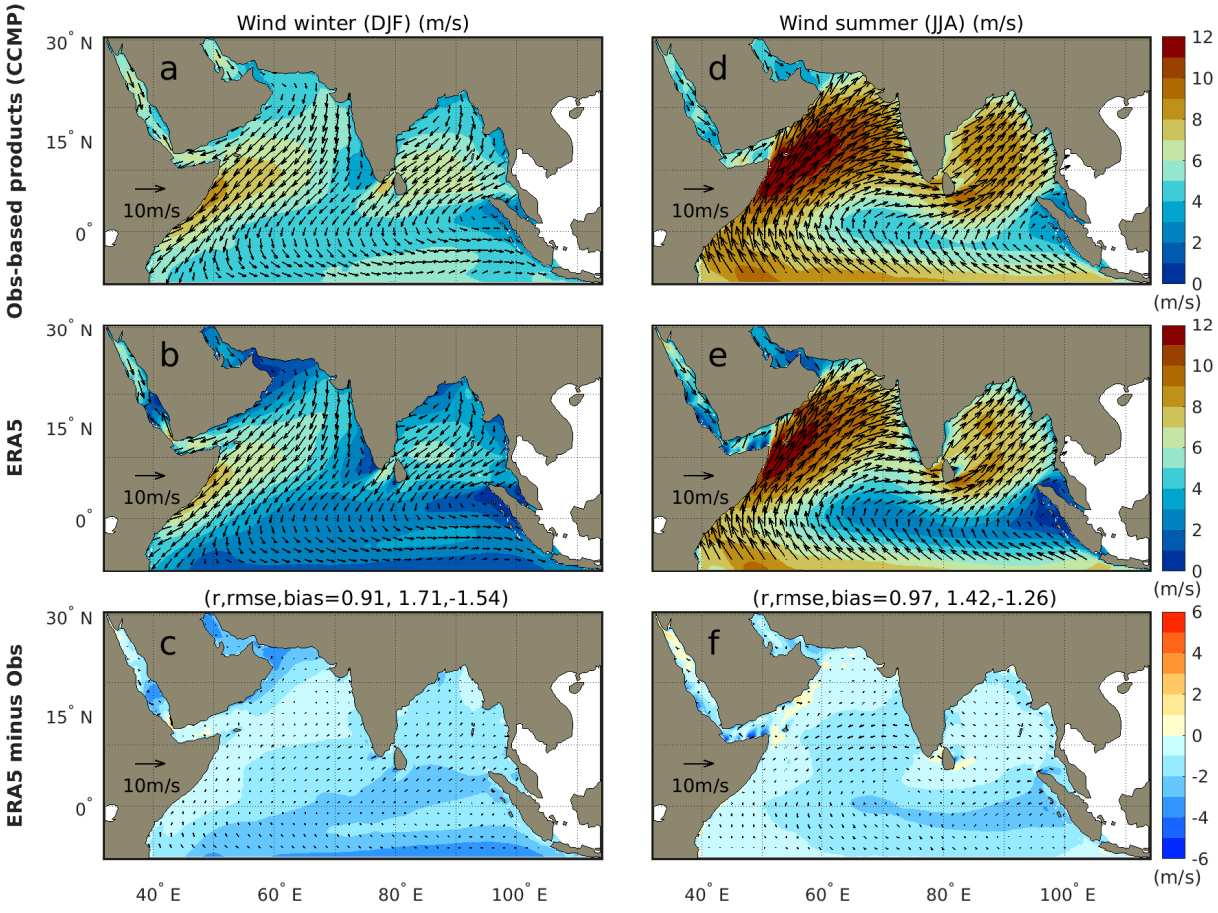

Figure A4. Surface wind (10m) during (a-c) winter (December-February) and (d-f) summer (June-August) monsoons. Panels (a,d) show Cross-Calibrated Multi-Platform (CCMP) satellite observation-based product, (b,e) show ERA5 data product and (c,f) show differences between ERA5 and CCMP. Correlation coefficients r, RMSD and bias between the data and model seasonal means are indicated. Wind observational data is from CCMP satellite (see details in Table 2). CCMP and ERA5 results are averaged over the 1993-2020 period.

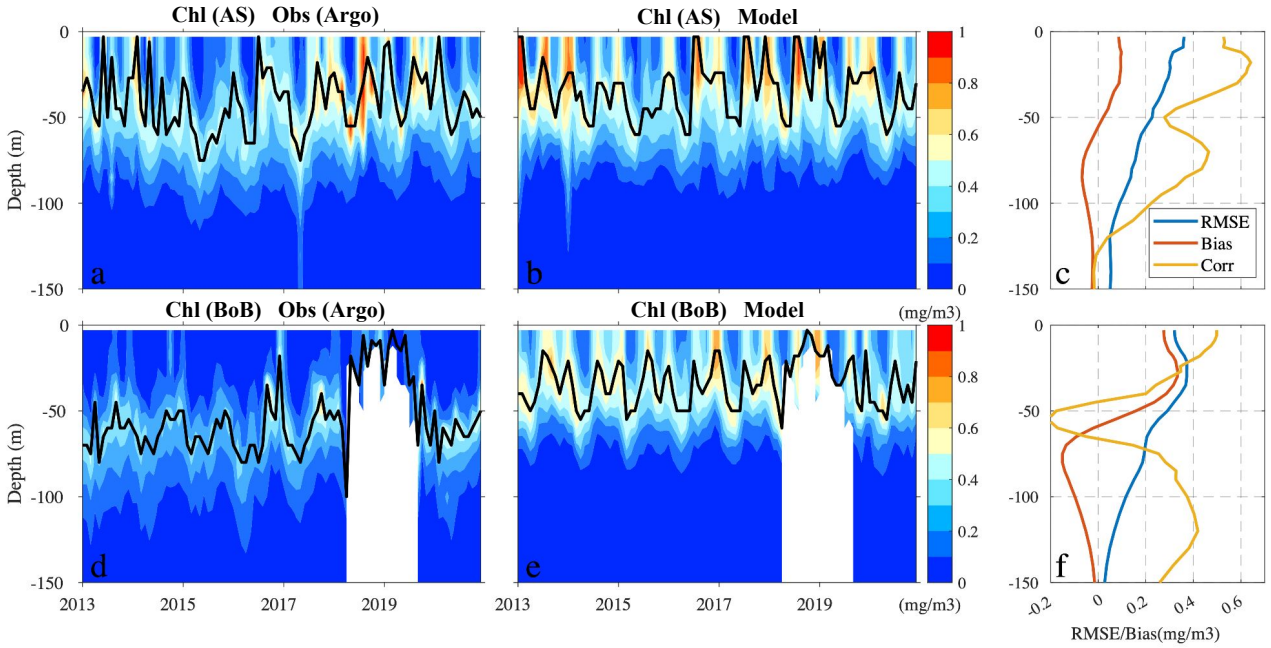

Figure A5. Comparison of observed and modeled vertical chlorophyll profiles in the Arabian Sea (a-c) and Bay of Bengal (d-f) using Argo float observations and model output. Panels (a,d) show Argo-derived chlorophyll concentrations; (b,e) show model-simulated chlorophyll concentrations; (c,f) show depth profiles of root mean square error (RMSE), bias, and correlation coefficient between model and Argo observations. In panels a-b and d-e, the black contour line indicates the depth of the subsurface chlorophyll maximum (SCM). Chlorophyll concentrations are shown in mg m^{-3}.

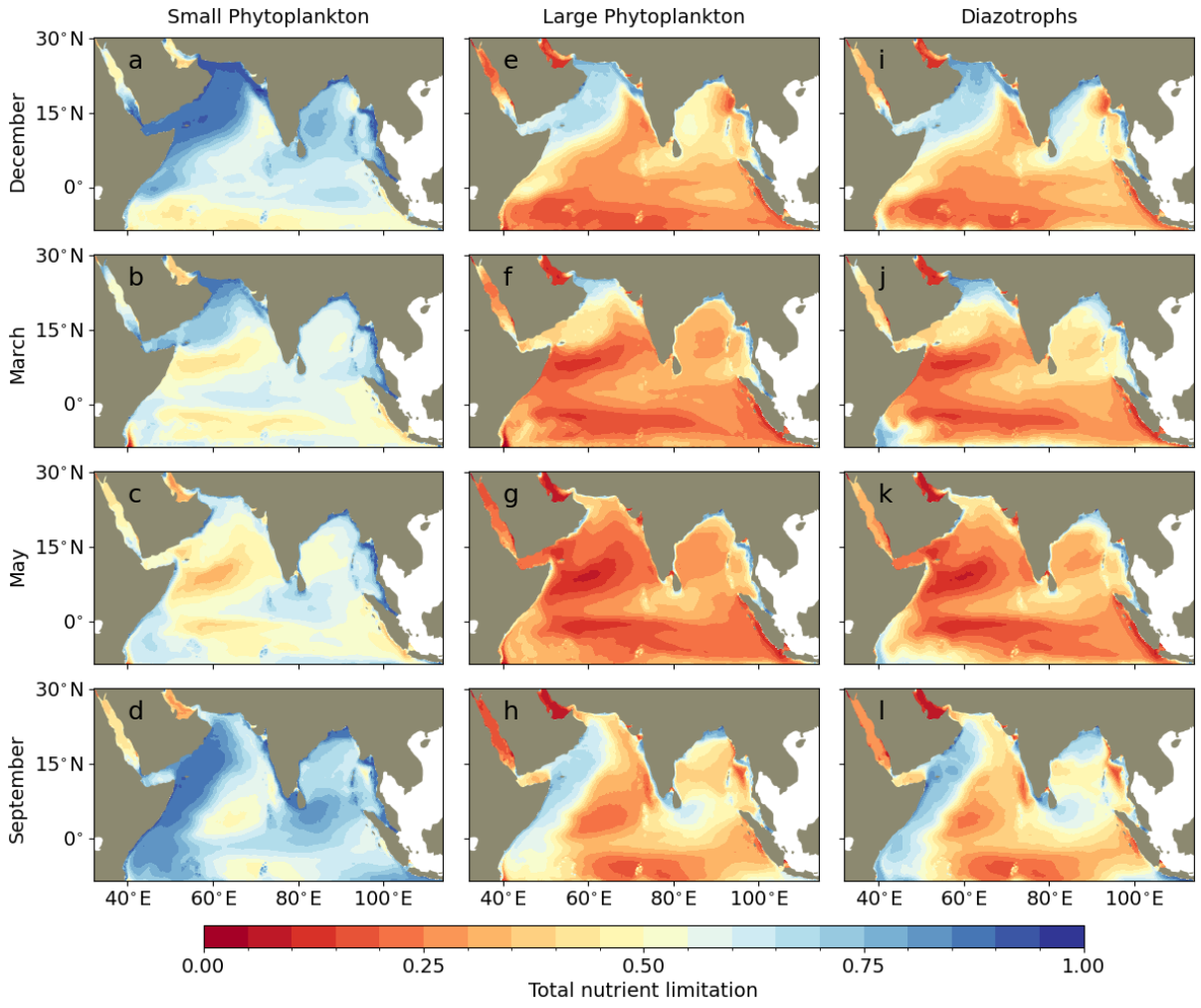

Figure A6. Climatological surface total nutrient limitation (nitrogen N, phosphorus P and iron Fe) following Liebig's Law of the Minimum in MOM6-COBALT-IND12 for small phytoplankton, large phytoplankton and diazotrophs in December, March, May and September. Model climatology is for 1980-2020. A value of 1 indicates no growth limitation by nutrients, whereas a value of 0 indicates complete growth limitation by nutrients.

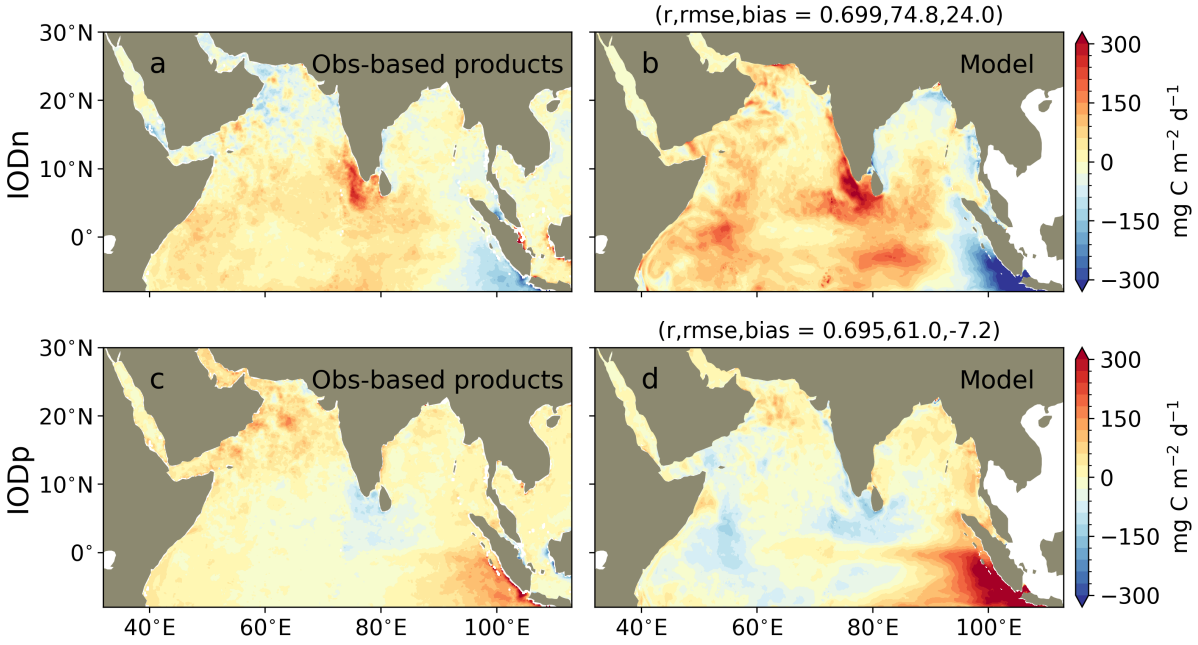

Integrated net primary productivity (PP) anomaly associated with the Indian Ocean Dipole (IOD). September-to-November PP composites during a-b) IOD negative phases and c-d) IOD positive phases in ~~observations~~ observation-based product and MOM6-COBALT-IND12. Composites are for ~~September-to- November~~ September-to-November months available in the CAFE satellite product for positive (2002, 2006, 2015, 2018, 2019) and negative (2005, 2010, 2016) IODs (see Table ~~2~~ 2 for details on data). Panels a and c of this figure showing the CAFE satellite product can be compared to Figure ~~21 a~~ 21a and ~~c~~ 21c showing the same composites but for the CbPM satellite product.

Integrated net primary productivity (PP) anomaly associated with the Indian Ocean Dipole (IOD). September-to-November PP composites during a-b) IOD negative phases and c-d) IOD positive phases in ~~observations~~ observation-based product and MOM6-COBALT-IND12. Composites are for ~~September-to- November~~ September-to-November months available in the CAFE satellite product for positive (2002, 2006, 2015, 2018, 2019) and negative (2005, 2010, 2016) IODs (see Table ~~2~~ 2 for details on data). Panels a and c of this figure showing the CAFE satellite product can be compared to Figure ~~21 a~~ 21a and ~~c~~ 21c showing the same composites but for the CbPM satellite product.

Figure A7. ~~Water discharge in the a) Ganges-Brahmaputra and b) Irrawaddy-Sittang river systems from observations (red), the raw GloFAS-ERA5 runoff product (grey, Harrigan et al., 2023, 2020), the modified GloFAS-ERA5 runoff product used to force MOM6-COBALT-IND12 (teal, $0.75 \times$ GloFAS-ERA5 m^3/s for Ganges-Brahmaputra and $1.7 \times$ GloFAS-ERA5 $+ 3564$ m^3/s for Irrawaddy-Sittang), and in the JRA55-do reanalysis (orange, Tsujino et al., 2018). Observations are from Jian et al. (2009) for Ganges-Brahmaputra and Recknagel et al. (GRDC, 2023) for Irrawaddy-Sittang. We note that the raw GloFAS-ERA5 can overestimates or underestimate the discharge compared to observations, while JRA55-do presents a systematic 1-2 months delay in the timing of the seasonal peak runoff.~~

Integrated net primary productivity (PP) anomaly associated with the Indian Ocean Dipole (IOD). September-to-November PP composites during a-b) IOD negative phases and c-d) IOD positive phases in ~~observations~~ observation-based product and MOM6-COBALT-IND12. Composites are for ~~September-to- November~~ September-to-November months available in the CAFE satellite product for positive (2002, 2006, 2015, 2018, 2019) and negative (2005, 2010, 2016) IODs (see Table ~~2~~ 2 for details on data). Panels a and c of this figure showing the CAFE satellite product can be compared to Figure ~~21 a~~ 21a and ~~c~~ 21c showing the same composites but for the CbPM satellite product.

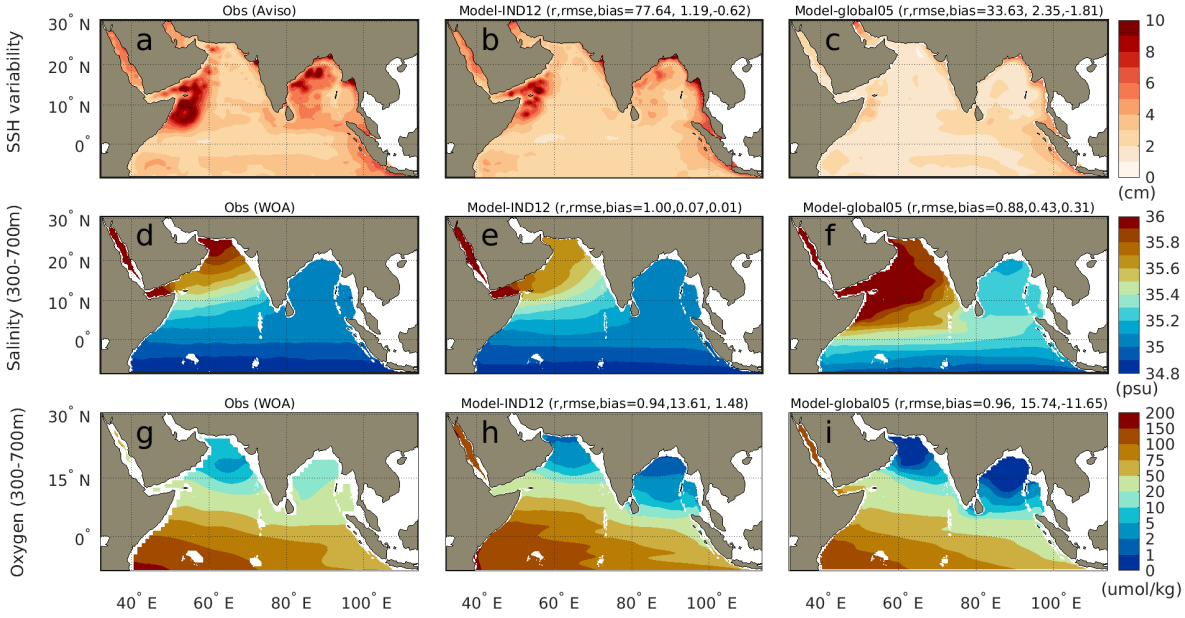

Figure A8. Comparison of sea level anomaly intraseasonal variability, subsurface salinity, and subsurface dissolved oxygen between observational products, the regional MOM6-COBALT-IND12 model (labeled as Model-IND12), and the global MOM6-COBALT configuration at 0.5° resolution (labeled as Model-global05). Panels (a–c) show the standard deviation of SLA representing intraseasonal variability (cm); panels (d–f) show the mean salinity averaged over 300–700 m depth (psu); and panels (g–i) show the mean dissolved oxygen averaged over 300–700 m depth. Comparison statistics—correlation coefficient (r), root mean square error (RMSE), and bias—are shown in parentheses. SLA intraseasonal variability is computed as the standard deviation of linearly detrended SLA, filtered using a 14–120 day band-pass filter.

References

2020, G. B. C. G.: The GEBCO_2020 Grid - a continuous terrain model of the global oceans and land., https://doi.org/10.5285/A29C5465-B138-234D-E053-6C86ABC040B9, 2020.

Accad, Y. and Pekeris, C. L.: Solution of the tidal equations for the M_2 and S_2 tides in the world oceans from a knowledge of the tidal potential alone, Philosophical Transactions of the Royal Society of London. Series A, Mathematical and Physical Sciences, 290, 235–266, https://doi.org/10.1098/rsta.1978.0083, 1978.

Adcroft, A., Anderson, W., Balaji, V., Blanton, C., Bushuk, M., Dufour, C. O., Dunne, J. P., Griffies, S. M., Hallberg, R., Harrison, M. J., Held, I. M., Jansen, M. F., John, J. G., Krasting, J. P., Langenhorst, A. R., Legg, S., Liang, Z., McHugh, C., Radhakrishnan, A., Reichl, B. G., Rosati, T., Samuels, B. L., Shao, A., Stouffer, R., Winton, M., Wittenberg, A. T., Xiang, B., Zadeh, N., and Zhang, R.: The GFDL Global Ocean and Sea Ice Model OM4.0: Model Description and Simulation Features, Journal of Advances in Modeling Earth Systems, 11, 3167–3211, https://doi.org/10.1029/2019MS001726, 2019.

Ahmed, A., Gauns, M., Kurian, S., Bardhan, P., Pratihary, A., Naik, H., Shenoy, D. M., and Naqvi, S.: Nitrogen fixation rates in the eastern Arabian Sea, Estuarine, Coastal and Shelf Science, 191, 74–83, https://doi.org/10.1016/j.ecss.2017.04.005, 2017.

Al Azhar, M., Lachkar, Z., Lévy, M., and Smith, S.: Oxygen Minimum Zone Contrasts Between the Arabian Sea and the Bay of Bengal Implied by Differences in Remineralization Depth, Geophysical Research Letters, 44, 2017GL075 157, https://doi.org/10.1002/2017GL075157, 2017.

Anjaneyan, P., Kuttippurath, J., Hareesh Kumar, P. V., Ali, S. M., and Raman, M.: Spatio-temporal changes of winter and spring phytoplankton blooms in Arabian sea during the period 1997–2020, Journal of Environmental Management, 332, 117 435, https://doi.org/https://doi.org/10.1016/j.jenvman.2023.117435, 2023.

Aparna, S. G., McCreary, J. P., Shankar, D., and Vinayachandran, P. N.: Signatures of Indian Ocean Dipole and El Niño–Southern Oscillation events in sea level variations in the Bay of Bengal, Journal of Geophysical Research: Oceans, 117, 2012JC008 055, https://doi.org/10.1029/2012JC008055, 2012.

Arakawa, A. and Lamb, V. R.: Computational Design of the Basic Dynamical Processes of the UCLA General Circulation Model, in: Methods in Computational Physics: Advances in Research and Applications, vol. 17, pp. 173–265, Elsevier, https://doi.org/10.1016/B978-0-12-460817-7.50009-4, 1977.

Banse, K., Naqvi, S. W. A., Narvekar, P. V., Postel, J. R., and Jayakumar, D. A.: Oxygen minimum zone of the open Arabian Sea: variability of oxygen and nitrite from daily to decadal timescales, Biogeosciences, 11, 2237–2261, https://doi.org/10.5194/bg-11-2237-2014, 2014.

Banzon, V., Smith, T. M., Chin, T. M., Liu, C., and Hankins, W.: A long-term record of blended satellite and in situ sea-surface temperature for climate monitoring, modeling and environmental studies, Earth System Science Data, 8, 165–176, https://doi.org/10.5194/essd-8-165-2016, publisher: Copernicus GmbH, 2016.

Barber, R. T., Marra, J., Bidigare, R. C., Codispoti, L. A., Halpern, D., Johnson, Z., Latasa, M., Goericke, R., and Smith, S. L.: Primary productivity and its regulation in the Arabian Sea during 1995, Deep Sea Research Part II: Topical Studies in Oceanography, 48, 1127–1172, https://doi.org/10.1016/S0967-0645(00)00134-X, 2001.

Barton, K. N., Pal, N., Brus, S. R., Petersen, M. R., Arbic, B. K., Engwirda, D., Roberts, A. F., Westerink, J. J., Wirasaet, D., and Schindelegger, M.: Global Barotropic Tide Modeling Using Inline Self-Attraction and Loading in MPAS-Ocean, Journal of Advances in Modeling Earth Systems, 14, e2022MS003 207, https://doi.org/10.1029/2022MS003207, 2022.

Beal, L. M. and Donohue, K. A.: The Great Whirl: Observations of its seasonal development and interannual variability, Journal of Geophysical Research: Oceans, 118, 1–13, https://doi.org/10.1029/2012JC008198, 2013.

Beal, L. M., Hormann, V., Lumpkin, R., and Foltz, G. R.: The Response of the Surface Circulation of the Arabian Sea to Monsoonal Forcing, Journal of Physical Oceanography, 43, 2008–2022, https://doi.org/10.1175/JPO-D-13-033.1, 2013.

Behrenfeld, M. J. and Falkowski, P. G.: Photosynthetic rates derived from satellite-based chlorophyll concentration, Limnology and Oceanography, 42, 1–20, https://doi.org/10.4319/lo.1997.42.1.0001, 1997.

Bhattathiri, P., Devassy, V., and Radhakrishna, K.: Primary production in the Bay of Bengal during August 1978, Mahasagar-Bulletin of the National Institute of Oceanography, 13(4), 315–323, https://doi.org/http://drs.nio.org/drs/handle/2264/6858, 1980.

Bianchi, D., Dunne, J. P., Sarmiento, J. L., and Galbraith, E. D.: Data-based estimates of suboxia, denitrification, and N $_2$ O production in the ocean and their sensitivities to dissolved O $_2$: DATA-BASED SUBOXIA AND DENITRIFICATION, Global Biogeochemical Cycles, 26, n/a–n/a, https://doi.org/10.1029/2011GB004209, 2012.

Bopp, L., Resplandy, L., Orr, J. C., Doney, S. C., Dunne, J. P., Gehlen, M., Halloran, P., Heinze, C., Ilyina, T., Séférian, R., Tjiputra, J., and Vichi, M.: Multiple stressors of ocean ecosystems in the 21st century: projections with CMIP5 models, Biogeosciences, 10, 6225–6245, https://doi.org/10.5194/bg-10-6225-2013, 2013.

Boyer, T. P., Baranova, O. K., Coleman, C., Garcia, H. E., Grodsky, S. A., Locarnini, R. A., Mishonov, A. V., Paver, C., Reagan, J. R., Seidov, D., Smolyar, I. V., and Zweng, M. M.: World Ocean Database 2013, in: NOAA Atlas, vol. 87, NESDIS, Silver Spring, MD, a. mishonov, technical ed. edn., 2018.

Brandt, P., Dengler, M., Rubino, A., Quadfasel, D., and Schott, F.: Intraseasonal variability in the southwestern Arabian Sea and its relation to the seasonal circulation, Deep Sea Research Part II: Topical Studies in Oceanography, 50, 2129–2141, https://doi.org/10.1016/S0967-0645(03)00049-3, 2003.

Breitburg, D., Levin, L. A., Oschlies, A., Grégoire, M., Chavez, F. P., Conley, D. J., Garçon, V., Gilbert, D., Gutiérrez, D., Isensee, K., Jacinto, G. S., Limburg, K. E., Montes, I., Naqvi, S. W. A., Pitcher, G. C., Rabalais, N. N., Roman, M. R., Rose, K. A., Seibel, B. A., Telszewski, M., Yasuhara, M., and Zhang, J.: Declining oxygen in the global ocean and coastal waters, Science, 359, eaam7240, https://doi.org/10.1126/science.aam7240, 2018.

Bristow, L. A., Dalsgaard, T., Tiano, L., Mills, D. B., Bertagnolli, A. D., Wright, J. J., Hallam, S. J., Ulloa, O., Canfield, D. E., Revsbech, N. P., and Thamdrup, B.: Ammonium and nitrite oxidation at nanomolar oxygen concentrations in oxygen minimum zone waters, Proceedings of the National Academy of Sciences of the United States of America, 113, 10 601–10 606, https://www.jstor.org/stable/26471635, publisher: National Academy of Sciences, 2016.

Bristow, L. A., Callbeck, C. M., Larsen, M., Altabet, M. A., Dekaezemacker, J., Forth, M., Gauns, M., Glud, R. N., Kuypers, M. M. M., Lavik, G., Milucka, J., Naqvi, S. W. A., Pratihary, A., Revsbech, N. P., Thamdrup, B., Treusch, A. H., and Canfield, D. E.: N 2 production rates limited by nitrite availability in the Bay of Bengal oxygen minimum zone, Nature Geoscience, 10, 24–29, https://doi.org/10.1038/ngeo2847, number: 1 Publisher: Nature Publishing Group, 2017.

Bruce, J. G., Johnson, D. R., and Kindle, J. C.: Evidence for eddy formation in the eastern Arabian Sea during the northeast monsoon, Journal of Geophysical Research: Oceans, 99, 7651–7664, https://doi.org/10.1029/94JC00035, 1994.

Burek, P., Van der Knijff, J., and De Roo, A.: LISFLOOD, distributed water balance and flood simulation model :revised user manual 2013, JRC78917, Publications Office of the European Union, LU, https://data.europa.eu/doi/10.2788/24982, 2013.

Cai, W., Zheng, X.-T., Weller, E., Collins, M., Cowan, T., Lengaigne, M., Yu, W., and Yamagata, T.: Projected response of the Indian Ocean Dipole to greenhouse warming, Nature Geoscience, 6, 999–1007, https://doi.org/10.1038/ngeo2009, 2013.

Cai, W., Yang, K., Wu, L., Huang, G., Santoso, A., Ng, B., Wang, G., and Yamagata, T.: Opposite response of strong and moderate positive Indian Ocean Dipole to global warming, Nature Climate Change, 11, 27–32, https://doi.org/10.1038/s41558-020-00943-1, 2021.

Carter, B. R., Bittig, H. C., Fassbender, A. J., Sharp, J. D., Takeshita, Y., Xu, Y.-Y., Álvarez, M., Wanninkhof, R., Feely, R. A., and Barbero, L.: New and updated global empirical seawater property estimation routines, Limnology and Oceanography: Methods, 19, 785–809, https://doi.org/https://doi.org/10.1002/lom3.10461, 2021.

Chakraborty, K., Rose, L., Bhattacharya, T., Ghosh, J., Ghoshal, P. K., and Akhand, A.: Primary Productivity Dynamics in the Northern Indian Ocean: An Ecosystem Modeling Perspective, pp. 169–190, Springer International Publishing, Cham, https://doi.org/10.1007/978-3-031-34467-1_8, 2023.

Chelton, D. B., Deszoeke, R. A., Schlax, M. G., El Naggar, K., and Siwertz, N.: Geographical variability of the first baroclinic Rossby radius of deformation, Journal of Physical Oceanography, 28, 433–460, http://journals.ametsoc.org/doi/abs/10.1175/1520-0485(1998)028%3C0433:GVOTFB%3E2.0.CO%3B2, 1998.

Cheng, X., Xie, S.-P., McCreary, J. P., Qi, Y., and Du, Y.: Intraseasonal variability of sea surface height in the Bay of Bengal, Journal of Geophysical Research: Oceans, 118, 816–830, https://doi.org/10.1002/jgrc.20075, _eprint: https://onlinelibrary.wiley.com/doi/pdf/10.1002/jgrc.20075, 2013.

Cheng, X., McCreary, J. P., Qiu, B., Qi, Y., and Du, Y.: Intraseasonal-to-semiannual variability of sea-surface height in the astern, equatorial Indian Ocean and southern Bay of Bengal, Journal of Geophysical Research: Oceans, 122, 4051–4067, https://doi.org/10.1002/2016JC012662, _eprint: https://onlinelibrary.wiley.com/doi/pdf/10.1002/2016JC012662, 2017.

Currie, J. C., Lengaigne, M., Vialard, J., Kaplan, D. M., Aumont, O., Naqvi, S. W. A., and Maury, O.: Indian Ocean Dipole and El Niño/Southern Oscillation impacts on regional chlorophyll anomalies in the Indian Ocean, Biogeosciences, 10, 6677–6698, https://doi.org/10.5194/bg-10-6677-2013, 2013.

Dalpadado, P., Arrigo, K. R., Van Dijken, G. L., Gunasekara, S. S., Ostrowski, M., Bianchi, G., and Sperfeld, E.: Warming of the Indian Ocean and its impact on temporal and spatial dynamics of primary production, Progress in Oceanography, 198, 102 688, https://doi.org/10.1016/j.pocean.2021.102688, 2021.

De Boyer Montégut, C., Madec, G., Fischer, A. S., Lazar, A., and Iudicone, D.: Mixed layer depth over the global ocean: An examination of profile data and a profile-based climatology, Journal of Geophysical Research: Oceans, 109, 2004JC002 378, https://doi.org/10.1029/2004JC002378, 2004.

Deutsch, C., Ferrel, A., Seibel, B., Pörtner, H.-O., and Huey, R. B.: Climate change tightens a metabolic constraint on marine habitats, Science, 348, 1132–1135, https://doi.org/10.1126/science.aaa1605, 2015.

Deutsch, C., Penn, J. L., and Lucey, N.: Climate, Oxygen, and the Future of Marine Biodiversity, Annual Review of Marine Science, 16, 217–245, https://doi.org/10.1146/annurev-marine-040323-095231, 2024.

Devassy, V., Bhattathiri, P., and Radhakrishna, K.: Primary production in the Bay of Bengal during August 1977, Mahasagar-Bulletin of the National Institute of Oceanography, 16, https://doi.org/http://drs.nio.org/drs/handle/2264/6553, 1983.

Dierssen, H. M.: Perspectives on Empirical Approaches for Ocean Color Remote Sensing of Chlorophyll in a Changing Climate, Proceedings of the National Academy of Sciences of the United States of America, 107, 17 073–17 078, https://doi.org/10.1073/pnas.0913800107, 2010.

Ditkovsky, S., Resplandy, L., and Busecke, J.: Unique ocean circulation pathways reshape the Indian Ocean oxygen minimum zone with warming, Biogeosciences, 20, 4711–4736, https://doi.org/10.5194/bg-20-4711-2023, publisher: Copernicus GmbH, 2023.

do Rosário Gomes, H., Goes, J. I., Matondkar, S. P., Parab, S. G., Al-Azri, A. R., and Thoppil, P. G.: Blooms of Noctiluca miliaris in the Arabian Sea—An in situ and satellite study, Deep Sea Research Part I: Oceanographic Research Papers, 55, 751–765, https://doi.org/10.1016/j.dsr.2008.03.003, 2008.

Dunne, J. P., Sarmiento, J. L., and Gnanadesikan, A.: A synthesis of global particle export from the surface ocean and cycling through the ocean interior and on the seafloor, Global Biogeochemical Cycles, 21, GB4006, https://doi.org/10.1029/2006GB002907, 2007.

Egbert, G. D. and Erofeeva, S. Y.: Efficient Inverse Modeling of Barotropic Ocean Tides, Journal of Atmospheric and Oceanic Technology, 19, 183–204, https://doi.org/10.1175/1520-0426(2002)019<0183:EIMOBO>2.0.CO;2, 2002.

ESR: OSCAR third degree resolution ocean surface currents, https://doi.org/10.5067/OSCAR-03D01, 2009.

Flather, R.: A Tidal Model of the North-West European Continental Shelf, Memoires de la Societe Royale des Sciences de Liege, 10, 141–164, 1976.

Flather R.: A Tidal Model of the North-West European Continental Shelf., Mem. Soc. R. Sci. Liege., 10, 141–164, 1976.

Fox-Kemper, B., Danabasoglu, G., Ferrari, R., Griffies, S., Hallberg, R., Holland, M., Maltrud, M., Peacock, S., and Samuels, B.: Parameterization of mixed layer eddies. III: Implementation and impact in global ocean climate simulations, Ocean Modelling, 39, 61–78, https://doi.org/10.1016/j.ocemod.2010.09.002, 2011.

Frey, C., Sun, X., Szemberski, L., Casciotti, K. L., Garcia-Robledo, E., Jayakumar, A., Kelly, C. L., Lehmann, M. F., and Ward, B. B.: Kinetics of nitrous oxide production from ammonia oxidation in the Eastern Tropical North Pacific, Limnology and Oceanography, 68, 424–438, https://doi.org/10.1002/lno.12283, 2023.

Friedlingstein, P., Jones, M. W., O'Sullivan, M., Andrew, R. M., Bakker, D. C. E., Hauck, J., Le Quéré, C., Peters, G. P., Peters, W., Pongratz, J., Sitch, S., Canadell, J. G., Ciais, P., Jackson, R. B., Alin, S. R., Anthoni, P., Bates, N. R., Becker, M., Bellouin, N., Bopp, L., Chau, T. T. T., Chevallier, F., Chini, L. P., Cronin, M., Currie, K. I., Decharme, B., Djeutchouang, L. M., Dou, X., Evans, W., Feely, R. A., Feng, L., Gasser, T., Gilfillan, D., Gkritzalis, T., Grassi, G., Gregor, L., Gruber, N., Gürses, , Harris, I., Houghton, R. A., Hurtt, G. C., Iida, Y., Ilyina, T., Luijkx, I. T., Jain, A., Jones, S. D., Kato, E., Kennedy, D., Klein Goldewijk, K., Knauer, J., Korsbakken, J. I., Körtzinger, A., Landschützer, P., Lauvset, S. K., Lefèvre, N., Lienert, S., Liu, J., Marland, G., McGuire, P. C., Melton, J. R., Munro, D. R., Nabel, J. E. M. S., Nakaoka, S.-I., Niwa, Y., Ono, T., Pierrot, D., Poulter, B., Rehder, G., Resplandy, L., Robertson, E., Rödenbeck, C., Rosan, T. M., Schwinger, J., Schwingshackl, C., Séférian, R., Sutton, A. J., Sweeney, C., Tanhua, T., Tans, P. P., Tian, H., Tilbrook, B., Tubiello, F., van der Werf, G. R., Vuichard, N., Wada, C., Wanninkhof, R., Watson, A. J., Willis, D., Wiltshire, A. J., Yuan, W., Yue, C., Yue, X., Zaehle, S., and Zeng, J.: Global Carbon Budget 2021, Earth System Science Data, 14, 1917–2005, https://doi.org/10.5194/essd-14-1917-2022, publisher: Copernicus GmbH, 2022.

Gandhi, N., Ramesh, R., Srivastava, R., Sheshshayee, M. S., Dwivedi, R. M., and Raman, M.: Nitrogen Uptake Rates during Spring in the NE Arabian Sea, International Journal of Oceanography, 2010, 1–10, https://doi.org/10.1155/2010/127493, 2010.

Gandhi, N., Singh, A., Ramesh, R., and Sheshshayee, M. S.: Nitrogen Sources for new production in the northeast Indian Ocean, International Journal of Oceanography, pp. 55–67, https://doi.org/10.1142/9789814355353_0004, 2011.

Garcia, H., Boyer, T., Baranova, O., Locarnini, R., Mishonov, A., Grodsky, A., Paver, C., Weathers, K., Smolyar, I., Reagan, J., Seidov, D., and Zweng, M.: World Ocean Atlas 2018: Product Documentation, Tech. rep., NOAA Atlas, A. Mishonov, Technical Ed., 2019.

Garcia H.E., Boyer T.P., Baranova O.K., Locarnini R.A., Mishonov A.V., Grodsky A., Paver C.R., Weathers K.W., Smolyar I.V., Reagan J.R., Seidov D., and Zweng M.M.: World Ocean Atlas 2018: Product Documentation., A. Mishonov, Technical Ed., NOAA Atlas, 2019.

Gauns, M., Madhupratap, M., Ramaiah, N., Jyothibabu, R., Fernandes, V., Paul, J. T., and Prasanna Kumar, S.: Comparative accounts of biological productivity characteristics and estimates of carbon fluxes in the Arabian Sea and the Bay of Bengal, Deep Sea Research Part II: Topical Studies in Oceanography, 52, 2003–2017, https://doi.org/10.1016/j.dsr2.2005.05.009, 2005.

Greaser, S. R., Subrahmanyam, B., Trott, C. B., and Roman-Stork, H. L.: Interactions Between Mesoscale Eddies and Synoptic Oscillations in the Bay of Bengal During the Strong Monsoon of 2019, Journal of Geophysical Research: Oceans, 125, e2020JC016 772, https://doi.org/10.1029/2020JC016772, _eprint: https://onlinelibrary.wiley.com/doi/pdf/10.1029/2020JC016772, 2020.

Gregg, W. W. and Rousseaux, C. S.: Global ocean primary production trends in the modern ocean color satellite record (1998–2015), Environmental Research Letters, 14, 124 011, https://doi.org/10.1088/1748-9326/ab4667, 2019.

Griffies, S. M. and Hallberg, R. W.: Biharmonic friction with a Smagorinsky-like viscosity for use in large-scale eddy-permitting ocean models, Monthly Weather Review, 128, 2935–2946, http://journals.ametsoc.org/doi/abs/10.1175/1520-0493(2000)128%3C2935:BFWASL%3E2.0.CO;2, 2000.

Grimaldi, S., Salamon, P., Disperati, J., Zsoter, E., Russo, C., Ramos, A., Carton De Wiart, C., Barnard, C., Hansford, E., Gomes, G., and Prudhomme, C.: River discharge and related historical data from the Global Flood Awareness System. v4.0, https://doi.org/10.24381/CDS.A4FDD6B9, 2022.

Gutknecht, E., Reffray, G., Gehlen, M., Triyulianti, I., Berlianty, D., and Gaspar, P.: Evaluation of an operational ocean model configuration at 1/12° spatial resolution for the Indonesian seas (NEMO2.3/INDO12) – Part 2: Biogeochemistry, Geosci. Model Dev., 9, 1523–1543, https://doi.org/10.5194/gmd-9-1523-2016, gMD, 2016.

Hallberg, R.: Using a resolution function to regulate parameterizations of oceanic mesoscale eddy effects, Ocean Modelling, 72, 92–103, https://doi.org/10.1016/j.ocemod.2013.08.007, 2013.

Hallberg, R. and Adcroft, A.: Reconciling estimates of the free surface height in Lagrangian vertical coordinate ocean models with mode-split time stepping, Ocean Modelling, 29, 15–26, https://doi.org/10.1016/j.ocemod.2009.02.008, 2009.

Harrigan, S., Zsoter, E., Alfieri, L., Prudhomme, C., Salamon, P., Wetterhall, F., Barnard, C., Cloke, H., and Pappenberger, F.: GloFAS-ERA5 operational global river discharge reanalysis 1979–present, Earth System Science Data, 12, 2043–2060, https://doi.org/10.5194/essd-12-2043-2020, publisher: Copernicus GmbH, 2020.

Harrigan, S., Zsoter, E., Cloke, H., Salamon, P., and Prudhomme, C.: Daily ensemble river discharge reforecasts and real-time forecasts from the operational Global Flood Awareness System, Hydrology and Earth System Sciences, 27, 1–19, https://doi.org/10.5194/hess-27-1-2023, publisher: Copernicus GmbH, 2023.

Helm, K. P., Bindoff, N. L., and Church, J. A.: Observed decreases in oxygen content of the global ocean, Geophysical Research Letters, 38, L23 602, https://doi.org/10.1029/2011GL049513, 2011.

Herbert, R. J., Krom, M. D., Carslaw, K. S., Stockdale, A., Mortimer, R. J. G., Benning, L. G., Pringle, K., and Browse, J.: The Effect of Atmospheric Acid Processing on the Global Deposition of Bioavailable Phosphorus From Dust, Global Biogeochemical Cycles, 32, 1367–1385, https://doi.org/10.1029/2018GB005880, 2018.

Hersbach, H., Bell, B., Berrisford, P., Hirahara, S., Horányi, A., Muñoz-Sabater, J., Nicolas, J., Peubey, C., Radu, R., Schepers, D., Simmons, A., Soci, C., Abdalla, S., Abellan, X., Balsamo, G., Bechtold, P., Biavati, G., Bidlot, J., Bonavita, M., De Chiara, G., Dahlgren, P., Dee, D., Diamantakis, M., Dragani, R., Flemming, J., Forbes, R., Fuentes, M., Geer, A., Haimberger, L., Healy, S., Hogan, R. J., Hólm, E., Janisková, M., Keeley, S., Laloyaux, P., Lopez, P., Lupu, C., Radnoti, G., de Rosnay, P., Rozum, I., Vamborg, F., Villaume, S., and Thépaut, J.-N.: The ERA5 global reanalysis, Quarterly Journal of the Royal Meteorological Society, 146, 1999–2049, https://doi.org/10.1002/qj.3803, 2020.

Hong, C.-C., Li, T., LinHo, and Kug, J.-S.: Asymmetry of the Indian Ocean Dipole. Part I: Observational Analysis, Journal of Climate, 21, 4834–4848, https://doi.org/10.1175/2008JCLI2222.1, 2008a.

Hong, C.-C., Li, T., and Luo, J.-J.: Asymmetry of the Indian Ocean Dipole. Part II: Model Diagnosis*, Journal of Climate, 21, 4849–4858, https://doi.org/10.1175/2008JCLI2223.1, 2008b.

Horowitz, L. W., Naik, V., Paulot, F., Ginoux, P. A., Dunne, J. P., Mao, J., Schnell, J., Chen, X., He, J., John, J. G., Lin, M., Lin, P., Malyshev, S., Paynter, D., Shevliakova, E., and Zhao, M.: The GFDL Global Atmospheric Chemistry-Climate Model AM4.1: Model Description and Simulation Characteristics, Journal of Advances in Modeling Earth Systems, 12, e2019MS002 032, https://doi.org/10.1029/2019MS002032, 2020.

Irazoqui Apecechea, M., Verlaan, M., Zijl, F., Le Coz, C., and Kernkamp, H.: Effects of self-attraction and loading at a regional scale: a test case for the Northwest European Shelf, Ocean Dynamics, 67, 729–749, https://doi.org/10.1007/s10236-017-1053-4, 2017.

Ito, T., Minobe, S., Long, M. C., and Deutsch, C.: Upper ocean O_2 trends: 1958–2015, Geophysical Research Letters, 44, 4214–4223, https://doi.org/10.1002/2017GL073613, 2017.

Jackson, L., Hallberg, R., and Legg, S.: A Parameterization of Shear-Driven Turbulence for Ocean Climate Models, Journal of Physical Oceanography, 38, 1033–1053, https://doi.org/10.1175/2007JPO3779.1, 2008.

Jebri, F., Jacobs, Z. L., Raitsos, D. E., Srokosz, M., Painter, S. C., Kelly, S., Roberts, M. J., Scott, L., Taylor, S. F. W., Palmer, M., Kizenga, H., Shaghude, Y., Wihsgott, J., and Popova, E.: Interannual monsoon wind variability as a key driver of East African small pelagic fisheries, Scientific Reports, 10, 13 247, https://doi.org/10.1038/s41598-020-70275-9, number: 1 Publisher: Nature Publishing Group, 2020.

Jian, J., Webster, P. J., and Hoyos, C. D.: Large-scale controls on Ganges and Brahmaputra river discharge on intraseasonal and seasonal time-scales, Quarterly Journal of the Royal Meteorological Society, 135, 353–370, https://doi.org/10.1002/qj.384, _eprint: https://onlinelibrary.wiley.com/doi/pdf/10.1002/qj.384, 2009.

Jiao, X., Zhou, J., Hu, M., Wang, M., Wu, H., Wu, K., and Chen, D.: Evaluation of three prevalent global riverine nutrient transport models, Environmental Science and Pollution Research, 30, 122 875–122 885, https://doi.org/10.1007/s11356-023-31041-2, 2023.

Kalita, R. and Lotliker, A. A.: Assessment of satellite-based Net Primary Productivity models in different biogeochemical provinces over the northern Indian Ocean, International Journal of Remote Sensing, pp. 1–20, https://doi.org/10.1080/01431161.2023.2247533, 2023.

Kobayashi, S., Ota, Y., Harada, Y., Ebita, A., Moriya, M., Onoda, H., Onogi, K., Kamahori, H., Kobayashi, C., Endo, H., Miyaoka, K., and Takahashi, K.: The JRA-55 Reanalysis: General Specifications and Basic Characteristics, Journal of the Meteorological Society of Japan. Ser. II, 93, 5–48, https://doi.org/10.2151/jmsj.2015-001, 2015.

Krishna, M., Prasad, M., Rao, D., Viswanadham, R., Sarma, V., and Reddy, N.: Export of dissolved inorganic nutrients to the northern Indian Ocean from the Indian monsoonal rivers during discharge period, Geochimica et Cosmochimica Acta, 172, 430–443, https://doi.org/10.1016/j.gca.2015.10.013, 2016.

Kumar, S., Ramesh, R., Sardesai, S., and Sheshshayee, M. S.: High new production in the Bay of Bengal: Possible causes and implications, Geophysical Research Letters, 31, 2004GL021 005, https://doi.org/10.1029/2004GL021005, 2004.

Kumar, S., Ramesh, R., Dwivedi, R. M., Raman, M., Sheshshayee, M. S., and D'Souza, W.: Nitrogen Uptake in the Northeastern Arabian Sea during Winter Cooling, International Journal of Oceanography, 2010, 1–11, https://doi.org/10.1155/2010/819029, 2010.

Kwiatkowski, L., Bopp, L., Aumont, O., Ciais, P., Cox, P. M., Laufkötter, C., Li, Y., and Séférian, R.: Emergent constraints on projections of declining primary production in the tropical oceans, Nature Climate Change, 7, 355–358, https://doi.org/10.1038/nclimate3265, 2017.

Kwiatkowski, L., Torres, O., Bopp, L., Aumont, O., Chamberlain, M., Christian, J. R., Dunne, J. P., Gehlen, M., Ilyina, T., John, J. G., Lenton, A., Li, H., Lovenduski, N. S., Orr, J. C., Palmieri, J., Santana-Falcón, Y., Schwinger, J., Séférian, R., Stock, C. A., Tagliabue, A., Takano,

Y., Tjiputra, J., Toyama, K., Tsujino, H., Watanabe, M., Yamamoto, A., Yool, A., and Ziehn, T.: Twenty-first century ocean warming, acidification, deoxygenation, and upper-ocean nutrient and primary production decline from CMIP6 model projections, Biogeosciences, 17, 3439–3470, https://doi.org/10.5194/bg-17-3439-2020, 2020.

Lachkar, Z., Smith, S., Lévy, M., and Pauluis, O.: Eddies reduce denitrification and compress habitats in the Arabian Sea, Geophysical Research Letters, 43, 9148–9156, https://doi.org/10.1002/2016GL069876, 2016.

Lachkar, Z., Lévy, M., and Smith, S.: Intensification and deepening of the Arabian Sea oxygen minimum zone in response to increase in Indian monsoon wind intensity, Biogeosciences, 15, 159–186, https://doi.org/10.5194/bg-15-159-2018, 2018.

Lachkar, Z., Lévy, M., and Smith, K. S.: Strong Intensification of the Arabian Sea Oxygen Minimum Zone in Response to Arabian Gulf Warming, Geophysical Research Letters, 46, 5420–5429, https://doi.org/10.1029/2018GL081631, 2019.

Lachkar, Z., Lévy, M., Hailegeorgis, D., and Vallivattathillam, P.: Differences in recent and future trends in the Arabian Sea oxygen minimum zone: processes and uncertainties, Frontiers in Marine Science, 10, https://www.frontiersin.org/articles/10.3389/fmars.2023.1122043, 2023.

Large, W. G. and Yeager, S. G.: Diurnal to Decadal Global Forcing For Ocean and Sea-Ice Models: The Data Sets and Flux Climatologies, Technical report, National Center for Atmospheric Research, https://doi.org/10.5065/D6KK98Q6, a, b, 2004.

LaRowe, D. E., Arndt, S., Bradley, J. A., Burwicz, E., Dale, A. W., and Amend, J. P.: Organic carbon and microbial activity in marine sediments on a global scale throughout the Quaternary, Geochimica et Cosmochimica Acta, 286, 227–247, https://doi.org/10.1016/j.gca.2020.07.017, 2020.

Legg, S., Hallberg, R. W., and Girton, J. B.: Comparison of entrainment in overflows simulated by z-coordinate, isopycnal and non-hydrostatic models, Ocean Modelling, 11, 69–97, https://doi.org/10.1016/j.ocemod.2004.11.006, 2006.

Li, G., Xie, S.-P., and Du, Y.: A Robust but Spurious Pattern of Climate Change in Model Projections over the Tropical Indian Ocean, Journal of Climate, 29, 5589–5608, https://doi.org/10.1175/JCLI-D-15-0565.1, 2016.

Li, Z., Huang, S., Zhu, X., Sun, Z., Long, Y., and Xie, H.: Short-term offshore extension of Brahmaputra-Ganges and Irrawaddy freshwater plumes to the central northern Bay of Bengal based on in situ and satellite observations, Acta Oceanologica Sinica, 40, 80–93, https://doi.org/10.1007/s13131-021-1729-y, 2021.

Liao, E., Resplandy, L., Liu, J., and Bowman, K. W.: Amplification of the Ocean Carbon Sink During El Niños: Role of Poleward Ekman Transport and Influence on Atmospheric CO2, Global Biogeochemical Cycles, 34, e2020GB006 574, https://doi.org/10.1029/2020GB006574, 2020.

Liao, E., Resplandy, L., Yang, F., Zhao, Y., Ditkovsky, S., Malsang, M., Pearson, J., Ross, A. C., Hallberg, R., and Stock, C.: Model source code for "A high-resolution physical-biogeochemical model for marine resource applications in the Northern Indian Ocean (MOM6-COBALT-IND12)", https://doi.org/10.5281/ZENODO.14184011, 2024a.

Liao, E., Resplandy, L., Yang, F., Zhao, Y., Ditkovsky, S., Malsang, M., Pearson, J., Ross, A. C., Hallberg, R., and Stock, C.: Model input for "A high-resolution physical-biogeochemical model for marine resource applications in the Northern Indian Ocean (MOM6-COBALT-IND12)", https://doi.org/10.5281/ZENODO.14171404, 2024b.

Locarnini, R. A., Mishonov, A. V., Antonov, J. I., Boyer, T. P., Garcia, H. E., Baranova, O. K., Zweng, M. M., Paver, C., Reagan, J. R., Johnson, D. R., Hamilton, M. A., and Seidov, D.: World Ocean Atlas 2013, Volume 1: Temperature., Tech. rep., S. Levitus, Ed., A. Mishonov Technical Ed.; NOAA Atlas NESDIS 73, 40 pp, 2014.

Lopez, A.: Sea level daily gridded data from satellite observations for the global ocean from 1993 to present, https://doi.org/10.24381/CDS.4C328C78, 2018.

Luo, J. Y., Stock, C. A., Dunne, J. P., Saba, G. K., and Cook, L.: Ocean Biogeochemical Fingerprints of Fast-Sinking Tunicate and Fish Detritus, Geophysical Research Letters, 51, e2023GL107 052, https://doi.org/10.1029/2023GL107052, _eprint: https://onlinelibrary.wiley.com/doi/pdf/10.1029/2023GL107052, 2024.

Lévy, M., Shankar, D., André, J.-M., Shenoi, S. S. C., Durand, F., and de Boyer Montégut, C.: Basin-wide seasonal evolution of the Indian Ocean's phytoplankton blooms, Journal of Geophysical Research, 112, https://doi.org/10.1029/2007JC004090, 2007.

Lévy, M., Resplandy, L., Palter, J. B., Couespel, D., and Lachkar, Z.: The crucial contribution of mixing to present and future ocean oxygen distribution, in: Ocean Mixing, pp. 329–344, Elsevier, https://doi.org/10.1016/B978-0-12-821512-8.00020-7, 2022.

Löscher, C. R.: Reviews and syntheses: Trends in primary production in the Bay of Bengal – is it at a tipping point?, Biogeosciences, 18, 4953–4963, https://doi.org/10.5194/bg-18-4953-2021, 2021.

Löscher, C. R., Mohr, W., Bange, H. W., and Canfield, D. E.: No nitrogen fixation in the Bay of Bengal?, Biogeosciences, 17, 851–864, https://doi.org/10.5194/bg-17-851-2020, 2020.

Mahadevan, A.: The Impact of Submesoscale Physics on Primary Productivity of Plankton, Annual Review of Marine Science, 8, 161–184, https://doi.org/10.1146/annurev-marine-010814-015912, 2016.

Malsang, M., Resplandy, L., Bopp, L., Zhao, Y., Ditkovsky, S., Yang, F., Paulot, F., and Lévy, M.: Contemporary decline in northern Indian Ocean primary production weakly offset by rising atmospheric nitrogen deposition, Frontiers in Marine Science, 11, https://doi.org/10.3389/fmars.2024.1418634, publisher: Frontiers, 2024.

Manizza, M.: Bio-optical feedbacks among phytoplankton, upper ocean physics and sea-ice in a global model, Geophysical Research Letters, 32, L05 603, https://doi.org/10.1029/2004GL020778, 2005.

Marchesiello, P., McWilliams, J. C., and Shchepetkin, A.: Open boundary conditions for long-term integration of regional oceanic models, Ocean Modelling, 3, 1–20, https://doi.org/10.1016/S1463-5003(00)00013-5, 2001.

Marra, J. F., Barber, R. T., Barber, E., Bidigare, R. R., Chamberlin, W. S., Goericke, R., Hargreaves, B. R., Hiscock, M., Iturriaga, R., Johnson, Z. I., Kiefer, D. A., Kinkade, C., Knudson, C., Lance, V., Langdon, C., Lee, Z., Perry, M. J., Smith, W. O., Vaillancourt, R., and Zoffoli, L.: A database of ocean primary productivity from the ^{14} C method, Limnology and Oceanography Letters, 6, 107–111, https://doi.org/10.1002/lol2.10175, 2021.

Mayorga, E., Seitzinger, S. P., Harrison, J. A., Dumont, E., Beusen, A. H., Bouwman, A., Fekete, B. M., Kroeze, C., and Van Drecht, G.: Global Nutrient Export from WaterSheds 2 (NEWS 2): Model development and implementation, Environmental Modelling & Software, 25, 837–853, https://doi.org/10.1016/j.envsoft.2010.01.007, 2010.

McCarthy, J. J., Garside, C., and Nevins, J. L.: Nitrogen dynamics during the Arabian Sea Northeast Monsoon, Deep Sea Research Part II: Topical Studies in Oceanography, 46, 1623–1664, https://doi.org/10.1016/S0967-0645(99)00038-7, 1999.

McCreary, J. P., Kundu, P. K., and Molinari, R. L.: A numerical investigation of dynamics, thermodynamics and mixed-layer processes in the Indian Ocean, Progress in Oceanography, 31, 181–244, https://doi.org/10.1016/0079-6611(93)90002-U, 1993.

McCreary, J. P., Yu, Z., Hood, R. R., Vinaychandran, P., Furue, R., Ishida, A., and Richards, K. J.: Dynamics of the Indian-Ocean oxygen minimum zones, Progress in Oceanography, 112-113, 15–37, https://doi.org/10.1016/j.pocean.2013.03.002, 2013.

McPhaden, M. J., Meyers, G., Ando, K., Masumoto, Y., Murty, V. S. N., Ravichandran, M., Syamsudin, F., Vialard, J., Yu, L., and Yu, W.: RAMA: The Research Moored Array for African–Asian–Australian Monsoon Analysis and Prediction*, Bulletin of the American Meteorological Society, 90, 459–480, https://doi.org/10.1175/2008BAMS2608.1, publisher: American Meteorological Society Section: Bulletin of the American Meteorological Society, 2009.

Mears, C., Lee, T., Ricciardulli, L., Wang, X., and Wentz, F.: RSS Cross-Calibrated Multi-Platform (CCMP) monthly ocean vector wind analysis on 0.25 deg grid, Version 3.0, https://doi.org/10.56236/RSS-uv1m30, institution: Remote Sensing Systems, 2022.

Measures, C. and Vink, S.: Seasonal variations in the distribution of Fe and Al in the surface waters of the Arabian Sea, Deep Sea Research Part II: Topical Studies in Oceanography, 46, 1597–1622, https://doi.org/10.1016/S0967-0645(99)00037-5, 1999.

Milliman, J. D. and Farnsworth, K. L.: River Discharge to the Coastal Ocean: A Global Synthesis, Cambridge University Press, 1 edn., https://doi.org/10.1017/CBO9780511781247, 2011.

Moffett, J. W. and Landry, M. R.: Grazing control and iron limitation of primary production in the Arabian Sea: Implications for anticipated shifts in Southwest Monsoon intensity, Deep Sea Research Part II: Topical Studies in Oceanography, 179, 104 687, https://doi.org/10.1016/j.dsr2.2019.104687, 2020.

Moffett, J. W., Vedamati, J., Goepfert, T. J., Pratihary, A., Gauns, M., and Naqvi, S. W. A.: Biogeochemistry of iron in the Arabian Sea: Biogeochemistry of iron in the Arabian Sea, Limnology and Oceanography, 60, 1671–1688, https://doi.org/10.1002/lno.10132, 2015.

Murtugudde, R. and Busalacchi, A. J.: Interannual variability of the dynamics and thermodynamics of the tropical Indian Ocean, Journal of Climate, 12, 2300–2326, http://journals.ametsoc.org/doi/abs/10.1175/1520-0442(1999)012%3C2300:IVOTDA%3E2.0.CO;2, 1999.

Nagura, M. and McPhaden, M. J.: The Shallow Overturning Circulation in the Indian Ocean, Journal of Physical Oceanography, 48, 413–434, https://doi.org/10.1175/JPO-D-17-0127.1, 2018.

Nakazato, M., Kido, S., and Tozuka, T.: Mechanisms of asymmetry in sea surface temperature anomalies associated with the Indian Ocean Dipole revealed by closed heat budget, Scientific Reports, 11, 22 546, https://doi.org/10.1038/s41598-021-01619-2, 2021.

Naqvi, S. W.: Anoxia-Related Biogeochemistry of North Indian Ocean, Geochemical Perspectives, pp. 169–287, https://doi.org/10.7185/geochempersp.11.2, 2022.

Naqvi, S. W. A.: Evidence for ocean deoxygenation and its patterns: Indian Ocean, in: Ocean deoxygenation: Everyone's problem - Causes, impacts, consequences and solutions., p. 562, Laffoley, D. & Baxter, J.M. (eds.). IUCN, Gland, Switzerland, 2019.

Naqvi, S. W. A.: Deoxygenation in Marginal Seas of the Indian Ocean, Frontiers in Marine Science, 8, 88, https://doi.org/10.3389/fmars.2021.624322, 2021.

Naqvi, S. W. A., Naik, H., Pratihary, A., D'Souza, W., Narvekar, P. V., Jayakumar, D. A., Devol, A. H., Yoshinari, T., and Saino, T.: Coastal versus open-ocean denitrification in the Arabian Sea, Biogeosciences, 3, 621–633, https://hal.archives-ouvertes.fr/hal-00297586/, 2006.

Naqvi, S. W. A., Naik, H., Jayakumar, A., Pratihary, A. K., Narvenkar, G., Kurian, S., Agnihotri, R., Shailaja, M. S., and Narvekar, P. V.: Seasonal Anoxia Over the Western Indian Continental Shelf, in: Indian Ocean Biogeochemical Processes and Ecological Variability, pp. 333–345, American Geophysical Union (AGU), https://doi.org/10.1029/2008GM000745, _eprint: https://onlinelibrary.wiley.com/doi/pdf/10.1029/2008GM000745, 2009.

Naqvi, S. W. A., Moffett, J. W., Gauns, M. U., Narvekar, P. V., Pratihary, A. K., Naik, H., Shenoy, D. M., Jayakumar, D. A., Goepfert, T. J., Patra, P. K., Al-Azri, A., and Ahmed, S. I.: The Arabian Sea as a high-nutrient, low-chlorophyll region during the late Southwest Monsoon, Biogeosciences, 7, 2091–2100, https://doi.org/10.5194/bg-7-2091-2010, 2010.

Nienhaus, M. J., Subrahmanyam, B., and Murty, V. S. N.: Altimetric Observations and Model Simulations of Coastal Kelvin Waves in the Bay of Bengal, Marine Geodesy, 35, 190–216, https://doi.org/10.1080/01490419.2012.718607, 2012.

Nuncio, M. and Kumar, S. P.: Life cycle of eddies along the western boundary of the Bay of Bengal and their implications, Journal of Marine Systems, 94, 9–17, https://doi.org/10.1016/j.jmarsys.2011.10.002, 2012.

Olsen, A., Key, R. M., van Heuven, S., Lauvset, S. K., Velo, A., Lin, X., Schirnick, C., Kozyr, A., Tanhua, T., Hoppema, M., Jutterström, S., Steinfeldt, R., Jeansson, E., Ishii, M., Pérez, F. F., and Suzuki, T.: The Global Ocean Data Analysis Project version 2 (GLODAPv2) – an

internally consistent data product for the world ocean, Earth System Science Data, 8, 297–323, https://doi.org/10.5194/essd-8-297-2016, publisher: Copernicus GmbH, 2016.

Orlanski, I.: A simple boundary condition for unbounded hyperbolic flows, Journal of Computational Physics, 21, 251–269, https://doi.org/10.1016/0021-9991(76)90023-1, 1976.

Paulmier, A. and Ruiz-Pino, D.: Oxygen minimum zones (OMZs) in the modern ocean, Progress in Oceanography, 80, 113–128, https://doi.org/10.1016/j.pocean.2008.08.001, 2009.

Paulot, F., Stock, C., John, J. G., Zadeh, N., and Horowitz, L. W.: Ocean Ammonia Outgassing: Modulation by CO_2 and Anthropogenic Nitrogen Deposition, Journal of Advances in Modeling Earth Systems, 12, e2019MS002 026, https://doi.org/10.1029/2019MS002026, 2020.

Pearson, J., Resplandy, L., and Poupon, M.: Coastlines at Risk of Hypoxia From Natural Variability in the Northern Indian Ocean, Global Biogeochemical Cycles, 36, https://doi.org/10.1029/2021GB007192, 2022.

Peng, X., Fuchsman, C. A., Jayakumar, A., Warner, M. J., Devol, A. H., and Ward, B. B.: Revisiting nitrification in the Eastern Tropical S outh P acific: A focus on controls, Journal of Geophysical Research: Oceans, 121, 1667–1684, https://doi.org/10.1002/2015JC011455, 2016.

Phillips, H. E., Tandon, A., Furue, R., Hood, R., Ummenhofer, C. C., Benthuysen, J. A., Menezes, V., Hu, S., Webber, B., Sanchez-Franks, A., Cherian, D., Shroyer, E., Feng, M., Wijesekera, H., Chatterjee, A., Yu, L., Hermes, J., Murtugudde, R., Tozuka, T., Su, D., Singh, A., Centurioni, L., Prakash, S., and Wiggert, J.: Progress in understanding of Indian Ocean circulation, variability, air–sea exchange, and impacts on biogeochemistry, Ocean Science, 17, 1677–1751, https://doi.org/10.5194/os-17-1677-2021, publisher: Copernicus GmbH, 2021.

Pinsky, M. L., Worm, B., Fogarty, M. J., Sarmiento, J. L., and Levin, S. A.: Marine Taxa Track Local Climate Velocities, Science, 341, 1239–1242, https://doi.org/10.1126/science.1239352, 2013.

Piontkovski, S. and Al-Oufi, H.: The Omani shelf hypoxia and the warming Arabian Sea, International Journal of Environmental Studies, 72, 256–264, https://doi.org/10.1080/00207233.2015.1012361, 2015.

Polzin, K. L.: An abyssal recipe, Ocean Modelling, 30, 298–309, https://doi.org/10.1016/j.ocemod.2009.07.006, 2009.

Prakash, S. and Ramesh, R.: Is the Arabian Sea getting more productive?, Current Science, 92, 667–670, http://www.iisc.ernet.in/~currsci/mar102007/667.pdf, 2007.

Prakash, S., Ramesh, R., Sheshshayee, M. S., Dwivedi, R. M., and Raman, M.: Quantification of new production during a winter *Noctiluca scintillans* bloom in the Arabian Sea, Geophysical Research Letters, 35, L08 604, https://doi.org/10.1029/2008GL033819, 2008.

Prasanna Kumar, S., Nuncio, M., Ramaiah, N., Sardesai, S., Narvekar, J., Fernandes, V., and Paul, J. T.: Eddy-mediated biological productivity in the Bay of Bengal during fall and spring intermonsoons, Deep Sea Research Part I: Oceanographic Research Papers, 54, 1619–1640, https://doi.org/10.1016/j.dsr.2007.06.002, 2007a.

Prasanna Kumar, S., Sardessai, S., Ramaiah, N., Bhosle, N., Ramaswamy, V., Ramesh, R., Sharada, M., Sarin, M. M., Sarupria, J., and Muraleedharan, U.: Bay of Bengal Process Studies (BOBPS) Final Report, Bay of Bengal process studies, Technical Report, 2007b.

Queste, B. Y., Vic, C., Heywood, K. J., and Piontkovski, S. A.: Physical controls on oxygen distribution and denitrification potential in the north west Arabian Sea, Geophysical Research Letters, https://doi.org/10.1029/2017GL076666, 2018.

Radhakrishna, K.: Primary productivity of the Bay of Bengal during March-April 1975, Indian Journal of Mrine Sciences, 7, 58–60, https://doi.org/http://nopr.niscpr.res.in/handle/123456789/39374, 1978.

Rahaman, H., Ravichandran, M., Sengupta, D., Harrison, M. J., and Griffies, S. M.: Development of a regional model for the North Indian Ocean, Ocean Modelling, 75, 1–19, https://doi.org/10.1016/j.ocemod.2013.12.005, 2014.

Raiswell, R. and Canfield, D. E.: The Iron Biogeochemical Cycle Past and Present, Geochemical Perspectives, 1, 1–220, https://doi.org/10.7185/geochempersp.1.1, 2012.

Recknagel, T., Färber, C., Plessow, H., and Looser, U.: The Global Runoff Data Centre: A building block in the chain of reproducible hydrology, https://doi.org/10.5194/egusphere-egu23-15454, 2023.

Reichl, B. G. and Hallberg, R.: A simplified energetics based planetary boundary layer (ePBL) approach for ocean climate simulations., Ocean Modelling, 132, 112–129, https://doi.org/10.1016/j.ocemod.2018.10.004, 2018.

Reichl, B. G. and Li, Q.: A Parameterization with a Constrained Potential Energy Conversion Rate of Vertical Mixing Due to Langmuir Turbulence, Journal of Physical Oceanography, 49, 2935–2959, https://doi.org/10.1175/JPO-D-18-0258.1, 2019.

Resplandy, L., Lévy, M., Madec, G., Pous, S., Aumont, O., and Kumar, D.: Contribution of mesoscale processes to nutrient budgets in the Arabian Sea, Journal of Geophysical Research, 116, C11 007, https://doi.org/10.1029/2011JC007006, 2011.

Resplandy, L., Lévy, M., Bopp, L., Echevin, V., Pous, S., Sarma, V. V. S. S., and Kumar, D.: Controlling factors of the oxygen balance in the Arabian Sea's OMZ, Biogeosciences, 9, 5095–5109, https://doi.org/10.5194/bg-9-5095-2012, 2012.

Rixen, T., Gaye, B., and Emeis, K.-C.: The monsoon, carbon fluxes, and the organic carbon pump in the northern Indian Ocean, Progress in Oceanography, 175, 24–39, https://doi.org/10.1016/j.pocean.2019.03.001, 2019a.

Rixen, T., Gaye, B., Emeis, K.-C., and Ramaswamy, V.: The ballast effect of lithogenic matter and its influences on the carbon fluxes in the Indian Ocean, Biogeosciences, 16, 485–503, https://doi.org/10.5194/bg-16-485-2019, publisher: Copernicus GmbH, 2019b.

Rixen, T., Cowie, G., Gaye, B., Goes, J., do Rosário Gomes, H., Hood, R. R., Lachkar, Z., Schmidt, H., Segschneider, J., and Singh, A.: Present past and future of the OMZ in the northern Indian Ocean, preprint, Biogeochemistry: Open Ocean, https://doi.org/10.5194/bg-2020-82, 2020.

Roemmich, D. and Gilson, J.: The 2004–2008 mean and annual cycle of temperature, salinity, and steric height in the global ocean from the Argo Program, Progress in Oceanography, 82, 81–100, https://doi.org/10.1016/j.pocean.2009.03.004, 2009.

Ross, A. C., Stock, C. A., Adcroft, A., Curchitser, E., Hallberg, R., Harrison, M. J., Hedstrom, K., Zadeh, N., Alexander, M., Chen, W., Drenkard, E. J., Du Pontavice, H., Dussin, R., Gomez, F., John, J. G., Kang, D., Lavoie, D., Resplandy, L., Roobaert, A., Saba, V., Shin, S.-I., Siedlecki, S., and Simkins, J.: A high-resolution physical–biogeochemical model for marine resource applications in the northwest Atlantic (MOM6-COBALT-NWA12 v1.0), Geoscientific Model Development, 16, 6943–6985, https://doi.org/10.5194/gmd-16-6943-2023, 2023.

Roxy, M. K., Gnanaseelan, C., Parekh, A., Chowdary, J. S., Singh, S., Modi, A., Kakatkar, R., Mohapatra, S., Dhara, C., Shenoi, S. C., and Rajeevan, M.: Indian Ocean Warming, in: Assessment of Climate Change over the Indian Region: A Report of the Ministry of Earth Sciences (MoES), Government of India, edited by Krishnan, R., Sanjay, J., Gnanaseelan, C., Mujumdar, M., Kulkarni, A., and Chakraborty, S., pp. 191–206, Springer, Singapore, https://doi.org/10.1007/978-981-15-4327-2_10, 2020.

Roy, A.: Blue Economy in the Indian Ocean: Governance Perspectives for Sustainable Development in the Region, Observer Research Foundation (ORF), Occasional Paper, No. 181, 2019.

Saji, N. H., Goswami, B. N., Vinayachandran, P. N., and Yamagata, T.: A dipole mode in the tropical Indian Ocean, Nature, 401, 360–363, https://doi.org/10.1038/43854, 1999.

Sarma, V. and Aswanikumar, V.: Subsurface chlorophyll maxima in the north-western Bay of Bengal, Journal of Plankton Research, 13, 339–352, https://doi.org/10.1093/plankt/13.2.339, 1991.

Sarma, V. and Dalabehera, H.: New and primary production in the western Indian Ocean during fall monsoon, Marine Chemistry, 215, 103 687, https://doi.org/10.1016/j.marchem.2019.103687, 2019.

Sarma, V., Chopra, M., Rao, D., Priya, M., Rajula, G., Lakshmi, D., and Rao, V.: Role of eddies on controlling total and size-fractionated primary production in the Bay of Bengal, Continental Shelf Research, 204, 104 186, https://doi.org/10.1016/j.csr.2020.104186, 2020.

Sathyendranath, S., Brewin, R., Brockmann, C., Brotas, V., Calton, B., Chuprin, A., Cipollini, P., Couto, A., Dingle, J., Doerffer, R., Donlon, C., Dowell, M., Farman, A., Grant, M., Groom, S., Horseman, A., Jackson, T., Krasemann, H., Lavender, S., Martinez-Vicente, V., Mazeran, C., Mélin, F., Moore, T., Müller, D., Regner, P., Roy, S., Steele, C., Steinmetz, F., Swinton, J., Taberner, M., Thompson, A., Valente, A., Zühlke, M., Brando, V., Feng, H., Feldman, G., Franz, B., Frouin, R., Gould, R., Hooker, S., Kahru, M., Kratzer, S., Mitchell, B., Muller-Karger, F., Sosik, H., Voss, K., Werdell, J., and Platt, T.: An Ocean-Colour Time Series for Use in Climate Studies: The Experience of the Ocean-Colour Climate Change Initiative (OC-CCI), Sensors, 19, 4285, https://doi.org/10.3390/s19194285, 2019.

Savidge, G. and Gilpin, L.: Seasonal influences on size-fractionated chlorophyll a concentrations and primary production in the north-west Indian Ocean, Deep Sea Research Part II: Topical Studies in Oceanography, 46, 701–723, https://doi.org/10.1016/S0967-0645(98)00124-6, 1999.

Saxena, H., Sahoo, D., Nazirahmed, S., Chaudhari, D., Rahi, P., Kumar, S., Benavides, M., Krishna, A. V., Sudheer, A. K., and Singh, A.: The Bay of Bengal: An Enigmatic Diazotrophic Niche, Journal of Geophysical Research: Biogeosciences, 128, e2023JG007 687, https://doi.org/10.1029/2023JG007687, 2023.

Schmidt, H., Getzlaff, J., Löptien, U., and Oschlies, A.: Causes of uncertainties in the representation of the Arabian Sea oxygen minimum zone in CMIP5 models, Ocean Science, 17, 1303–1320, https://doi.org/10.5194/os-17-1303-2021, publisher: Copernicus GmbH, 2021.

Schmidt, M. and Eggert, A.: Oxygen cycling in the northern Benguela Upwelling System: Modelling oxygen sources and sinks, Progress in Oceanography, 149, 145–173, https://doi.org/10.1016/j.pocean.2016.09.004, 2016.

Schofield, O., Arnone, R., Bissett, P., Dickey, T., Davis, C., Finkel, Z., Oliver, M., and Moline, M.: Watercolors in the Coastal Zone: What Can We See?, Oceanography, 17, 24–31, https://doi.org/10.5670/oceanog.2004.44, 2004.

Schott, F. A. and McCreary, J. P.: The monsoon circulation of the Indian Ocean, Progress in Oceanography, 51, 1–123, http://www.sciencedirect.com/science/article/pii/S0079661101000830, 2001.

Schott, F. A., Mccreary, J. P., and Johnson, G. C.: Shallow Overturning Circulations of the Tropical-Subtropical Oceans, Geophysical Monograph Series, pp. 261–304, https://doi.org/10.1029/147GM15, 2004.

Sengupta, D., Senan, R., and Goswami, B. N.: Origin of intraseasonal variability of circulation in the tropical central Indian Ocean, Geophysical Research Letters, 28, 1267–1270, https://doi.org/10.1029/2000GL012251, 2001.

Sengupta, D., Senan, R., Goswami, B. N., and Vialard, J.: Intraseasonal Variability of Equatorial Indian Ocean Zonal Currents, Journal of Climate, 20, 3036–3055, https://doi.org/10.1175/JCLI4166.1, 2007.

Shankar, D. and Shetye, S. R.: On the dynamics of the Lakshadweep high and low in the southeastern Arabian Sea, Journal of Geophysical Research: Oceans, 102, 12 551–12 562, https://doi.org/10.1029/97JC00465, 1997.

Sharma, S., Ha, K.-J., Yamaguchi, R., Rodgers, K. B., Timmermann, A., and Chung, E.-S.: Future Indian Ocean warming patterns, Nature Communications, 14, 1789, https://doi.org/10.1038/s41467-023-37435-7, number: 1 Publisher: Nature Publishing Group, 2023.

Shenoi, S. S. C., Shankar, D., and Shetye, S. R.: Differences in heat budgets of the near-surface Arabian Sea and Bay of Bengal: Implications for the summer monsoon, Journal of Geophysical Research: Oceans, 107, 5–1–5–14, https://doi.org/10.1029/2000JC000679, _eprint: https://onlinelibrary.wiley.com/doi/pdf/10.1029/2000JC000679, 2002.

Shetye, S. R., Shenoi, S. S. C., Gouveia, A. D., Michael, G. S., Sundar, D., and Nampoothiri, G.: Wind-driven coastal upwelling along the western boundary of the Bay of Bengal during the southwest monsoon, Continental Shelf Research, 11, 1397–1408, https://doi.org/10.1016/0278-4343(91)90042-5, 1991.

Silsbe, G. M., Behrenfeld, M. J., Halsey, K. H., Milligan, A. J., and Westberry, T. K.: The CAFE model: A net production model for global ocean phytoplankton, Global Biogeochemical Cycles, 30, 1756–1777, https://doi.org/10.1002/2016GB005521, 2016.

Singh, D., Ghosh, S., Roxy, M. K., and McDermid, S.: Indian summer monsoon: Extreme events, historical changes, and role of anthropogenic forcings, WIREs Climate Change, 10, e571, https://doi.org/10.1002/wcc.571, 2019.

Siswanto, E., Sarker, M. L. R., Peter, B. N., Takemura, T., Horii, T., Matsumoto, K., Taketani, F., and Honda, M. C.: Variations of phytoplankton chlorophyll in the Bay of Bengal: Impact of climate changes and nutrients from different sources, Frontiers in Marine Science, 10, https://www.frontiersin.org/articles/10.3389/fmars.2023.1052286, 2023.

Sofianos, S. S., Johns, W. E., and Murray, S. P.: Heat and freshwater budgets in the Red Sea from direct observations at Bab el Mandeb, Deep Sea Research Part II: Topical Studies in Oceanography, 49, 1323–1340, https://doi.org/10.1016/S0967-0645(01)00164-3, 2002.

Sooraj, K. P., Terray, P., and Mujumdar, M.: Global warming and the weakening of the Asian summer monsoon circulation: assessments from the CMIP5 models, Climate Dynamics, 45, 233–252, https://doi.org/10.1007/s00382-014-2257-7, 2015.

Sprintall, J., Wijffels, S. E., Molcard, R., and Jaya, I.: Direct estimates of the Indonesian Throughflow entering the Indian Ocean: 2004–2006, Journal of Geophysical Research: Oceans, 114, https://doi.org/10.1029/2008JC005257, _eprint: https://agupubs.onlinelibrary.wiley.com/doi/pdf/10.1029/2008JC005257, 2009.

Sridevi, B., Sabira, S., and Sarma, V.: Impact of ocean warming on net primary production in the northern Indian Ocean: role of aerosols and freshening of surface ocean, Environmental Science and Pollution Research, 30, 53 616–53 634, https://doi.org/10.1007/s11356-023-26001-9, 2023.

St. Laurent, L. C., Simmons, H. L., and Jayne, S. R.: Estimating tidally driven mixing in the deep ocean: ESTIMATING TIDALLY DRIVEN MIXING, Geophysical Research Letters, 29, 21–1–21–4, https://doi.org/10.1029/2002GL015633, 2002.

Steele, M., Morley, R., and Ermold, W.: PHC: A Global Ocean Hydrography with a High-Quality Arctic Ocean, Journal of Climate, 14, 2079–2087, https://doi.org/10.1175/1520-0442(2001)014<2079:PAGOHW>2.0.CO;2, 2001.

Stepanov, V. N. and Hughes, C. W.: Parameterization of ocean self-attraction and loading in numerical models of the ocean circulation, Journal of Geophysical Research: Oceans, 109, 2003JC002 034, https://doi.org/10.1029/2003JC002034, 2004.

Stock, C. A., Dunne, J. P., and John, J. G.: Global-scale carbon and energy flows through the marine planktonic food web: An analysis with a coupled physical–biological model, Progress in Oceanography, 120, 1–28, https://doi.org/10.1016/j.pocean.2013.07.001, 2014.

Stock, C. A., Dunne, J. P., Fan, S., Ginoux, P., John, J., Krasting, J. P., Laufkötter, C., Paulot, F., and Zadeh, N.: Ocean Biogeochemistry in GFDL's Earth System Model 4.1 and Its Response to Increasing Atmospheric CO2, Journal of Advances in Modeling Earth Systems, 12, e2019MS002 043, https://doi.org/10.1029/2019MS002043, 2020.

Stock, C. A., Dunne, J. P., Luo, J. Y., Ross, A. C., Oostende, N., and Zadeh, N.: Photoacclimation and Photoadaptation Sensitivity in a Global Ocean Ecosystem Model, ESS Open Archive, https://www.authorea.com/users/572239/articles/1223884-photoacclimation-and-photoadaptation-sensitivity-in-a-global-ocean-ecosystem-model, 2024.

Stock, C. A., Dunne, J. P., Luo, J. Y., Ross, A. C., Van Oostende, N., Zadeh, N., Cordero, T. J., Liu, X., and Teng, Y.-C.: Photoacclimation and Photoadaptation Sensitivity in a Global Ocean Ecosystem Model, Journal of Advances in Modeling Earth Systems, 17, e2024MS004 701, https://doi.org/10.1029/2024MS004701, 2025.

Sunanda, N., Kuttippurath, J., Peter, R., Chakraborty, K., and Chakraborty, A.: Long-Term Trends and Impact of SARS-CoV-2 COVID-19 Lockdown on the Primary Productivity of the North Indian Ocean, Frontiers in Marine Science, Volume 8 - 2021, https://doi.org/10.3389/fmars.2021.669415, 2021.

Sunanda, N., Kuttippurath, J., Chakraborty, A., and Peter, R.: Stressors of primary productivity in the north Indian ocean revealed by satellite, reanalysis and CMIP6 data, Progress in Oceanography, 219, 103 164, https://doi.org/10.1016/j.pocean.2023.103164, 2023.

Sunanda, N., Kuttippurath, J., Peter, R., and Chakraborty, A.: An atmosphere–ocean coupled model for simulating physical and biogeochemical state of north Indian Ocean: Customisation and validation, Ocean Modelling, 191, 102 419, https://doi.org/https://doi.org/10.1016/j.ocemod.2024.102419, 2024.

Suresh, I., Vialard, J., Lengaigne, M., Izumo, T., Parvathi, V., and Muraleedharan, P. M.: Sea Level Interannual Variability Along the West Coast of India, Geophysical Research Letters, 45, https://doi.org/10.1029/2018GL080972, 2018.

Séférian, R., Berthet, S., Yool, A., Palmiéri, J., Bopp, L., Tagliabue, A., Kwiatkowski, L., Aumont, O., Christian, J., Dunne, J., Gehlen, M., Ilyina, T., John, J. G., Li, H., Long, M. C., Luo, J. Y., Nakano, H., Romanou, A., Schwinger, J., Stock, C., Santana-Falcón, Y., Takano, Y., Tjiputra, J., Tsujino, H., Watanabe, M., Wu, T., Wu, F., and Yamamoto, A.: Tracking Improvement in Simulated Marine Biogeochemistry Between CMIP5 and CMIP6, Current Climate Change Reports, 6, 95–119, https://doi.org/10.1007/s40641-020-00160-0, 2020.

Tseng, Y.-h., Bryan, F. O., and Whitney, M. M.: Impacts of the representation of riverine freshwater input in the community earth system model, Ocean Modelling, 105, 71–86, https://doi.org/10.1016/j.ocemod.2016.08.002, 2016.

Tsujino, H., Urakawa, S., Nakano, H., Small, R. J., Kim, W. M., Yeager, S. G., Danabasoglu, G., Suzuki, T., Bamber, J. L., Bentsen, M., Böning, C. W., Bozec, A., Chassignet, E. P., Curchitser, E., Boeira Dias, F., Durack, P. J., Griffies, S. M., Harada, Y., Ilicak, M., Josey, S. A., Kobayashi, C., Kobayashi, S., Komuro, Y., Large, W. G., Le Sommer, J., Marsland, S. J., Masina, S., Scheinert, M., Tomita, H., Valdivieso, M., and Yamazaki, D.: JRA-55 based surface dataset for driving ocean–sea-ice models (JRA55-do), Ocean Modelling, 130, 79–139, https://doi.org/10.1016/j.ocemod.2018.07.002, 2018.

Twining, B. S., Rauschenberg, S., Baer, S. E., Lomas, M. W., Martiny, A. C., and Antipova, O.: A nutrient limitation mosaic in the eastern tropical Indian Ocean, Deep Sea Research Part II: Topical Studies in Oceanography, 166, 125–140, https://doi.org/10.1016/j.dsr2.2019.05.001, 2019.

Udaya Bhaskar, T. V. S., Sarma, V. V. S. S., and Pavan Kumar, J.: Potential mechanisms responsible for spatial variability in intensity and thickness of oxygen minimum zone in the Bay of Bengal, Journal of Geophysical Research: Biogeosciences, 126, e2021JG006 341, https://doi.org/10.1029/2021JG006341, 2021.

Vallivattathillam, P., Iyyappan, S., Lengaigne, M., Ethé, C., Vialard, J., Levy, M., Suresh, N., Aumont, O., Resplandy, L., Naik, H., and Naqvi, W.: Positive Indian Ocean Dipole events prevent anoxia off the west coast of India, Biogeosciences, 14, 1541–1559, https://doi.org/10.5194/bg-14-1541-2017, 2017.

Veldhuis, M. J., Kraay, G. W., Van Bleijswijk, J. D., and Baars, M. A.: Seasonal and spatial variability in phytoplankton biomass, productivity and growth in the northwestern Indian Ocean: the southwest and northeast monsoon, 1992–1993, Deep Sea Research Part I: Oceanographic Research Papers, 44, 425–449, https://doi.org/10.1016/S0967-0637(96)00116-1, 1997.

Vialard, J., Shenoi, S. S. C., McCreary, J. P., Shankar, D., Durand, F., Fernando, V., and Shetye, S. R.: Intraseasonal response of the northern Indian Ocean coastal waveguide to the Madden-Julian Oscillation, Geophysical Research Letters, 36, 2009GL038 450, https://doi.org/10.1029/2009GL038450, 2009.

Vic, C., Roullet, G., Carton, X., and Capet, X.: Mesoscale dynamics in the Arabian Sea and a focus on the Great Whirl life cycle: A numerical investigation using ROMS, Journal of Geophysical Research: Oceans, 119, 6422–6443, https://doi.org/10.1002/2014JC009857, 2014.

Vinayachandran, P. N. M., Masumoto, Y., Roberts, M. J., Huggett, J. A., Halo, I., Chatterjee, A., Amol, P., Gupta, G. V. M., Singh, A., Mukherjee, A., Prakash, S., Beckley, L. E., Raes, E. J., and Hood, R.: Reviews and syntheses: Physical and biogeochemical processes associated with upwelling in the Indian Ocean, Biogeosciences, 18, 5967–6029, https://doi.org/10.5194/bg-18-5967-2021, 2021.

Wang, H., McClean, J. L., Talley, L. D., and Yeager, S.: Seasonal Cycle and Annual Reversal of the Somali Current in an Eddy-Resolving Global Ocean Model, Journal of Geophysical Research: Oceans, 123, 6562–6580, https://doi.org/10.1029/2018JC013975, _eprint: https://onlinelibrary.wiley.com/doi/pdf/10.1029/2018JC013975, 2018.

Wang, Y., Zhang, F., Geng, Z., Zhang, Y., Zhu, J., and Dai, X.: Effects of Climate Variability on Two Commercial Tuna Species Abundance in the Indian Ocean, Fishes, 8, 99, https://doi.org/10.3390/fishes8020099, 2023.

Watts, L. and Owens, N.: Nitrogen assimilation and the f-ratio in the northwestern Indian Ocean during an intermonsoon period, Deep Sea Research Part II: Topical Studies in Oceanography, 46, 725–743, https://doi.org/10.1016/S0967-0645(98)00125-8, 1999.

Watts, L., Sathyendranath, S., Caverhill, C., Maass, H., Platt, T., and Owens, N.: Modelling new production in the northwest Indian Ocean region, Marine Ecology Progress Series, 183, 1–12, https://doi.org/10.3354/meps183001, 1999.

Weatherall, P., Marks, K. M., Jakobsson, M., Schmitt, T., Tani, S., Arndt, J. E., Rovere, M., Chayes, D., Ferrini, V., and Wigley, R.: A new digital bathymetric model of the world's oceans, Earth and Space Science, 2, 331–345, https://doi.org/https://doi.org/10.1002/2015EA000107, 2015.

Webster, P. J., Moore, A. M., Loschnigg, J. P., and Leben, R. R.: Coupled ocean–atmosphere dynamics in the Indian Ocean during 1997–98, Nature, 401, 356–360, https://doi.org/10.1038/43848, number: 6751 Publisher: Nature Publishing Group, 1999.

Westberry, T., Behrenfeld, M. J., Siegel, D. A., and Boss, E.: Carbon-based primary productivity modeling with vertically resolved photoacclimation, Global Biogeochemical Cycles, 22, 2007GB003 078, https://doi.org/10.1029/2007GB003078, 2008.

Wiegner, T., Seitzinger, S., Glibert, P., and Bronk, D.: Bioavailability of dissolved organic nitrogen and carbon from nine rivers in the eastern United States, Aquatic Microbial Ecology, 43, 277–287, https://doi.org/10.3354/ame043277, 2006.

Wiggert, J. D., Vialard, J., and Behrenfeld, M. J.: Basin-Wide Modification of Dynamical and Biogeochemical Processes by the Positive Phase of the Indian Ocean Dipole During the SeaWiFS Era, in: Indian Ocean Biogeochemical Processes and Ecological Variability, Geophysical Monograph Series, pp. 385–407, American Geophysical Union (AGU), https://doi.org/10.1029/2008GM000776, 2009.

Wirth, A., Willebrand, J., and Schott, F.: Variability of the Great Whirl from observations and models, Deep Sea Research Part II: Topical Studies in Oceanography, 49, 1279–1295, https://doi.org/10.1016/S0967-0645(01)00165-5, 2002.

Yang, F., Resplandy, L., Zhao, Y., Liao, E., Ditkovsky, S., Malsang, M., Pearson, J., Ross, A. C., Hallberg, R., and Stock, C.: Model output for "A high-resolution physical-biogeochemical model for marine resource applications in the Northern Indian Ocean (MOM6-COBALT-IND12)", https://doi.org/10.5281/ZENODO.14183131, 2024.

Yang, J., Yu, L., Koblinsky, C. J., and Adamec, D.: Dynamics of the seasonal variations in the Indian Ocean from TOPEX/POSEIDON sea surface height and an ocean model, Geophysical Research Letters, 25, 1915–1918, https://doi.org/10.1029/98GL01401, 1998.

You, Y.: Seasonal variations of thermocline circulation and ventilation in the Indian Ocean, Journal of Geophysical Research: Oceans, 102, 10 391–10 422, https://doi.org/10.1029/96JC03600, _eprint: https://agupubs.onlinelibrary.wiley.com/doi/pdf/10.1029/96JC03600, 1997.

You, Y. and Tomczak, M.: Thermocline circulation and ventilation in the Indian Ocean derived from water mass analysis, Deep Sea Research Part I: Oceanographic Research Papers, 40, 13–56, https://doi.org/10.1016/0967-0637(93)90052-5, 1993.

Zhou, J., Scherer, L., Van Bodegom, P. M., Beusen, A. H. W., and Mogollón, J. M.: A Comparison Between Global Nutrient Retention Models for Freshwater Systems, Frontiers in Water, 4, 894 604, https://doi.org/10.3389/frwa.2022.894604, 2022.

Zuo, H., Balmaseda, M. A., Tietsche, S., Mogensen, K., and Mayer, M.: The ECMWF operational ensemble reanalysis–analysis system for ocean and sea ice: a description of the system and assessment, Ocean Science, 15, 779–808, https://doi.org/10.5194/os-15-779-2019, 2019.

Zweng, M. M., Reagan, J. R., Antonov, J. I., Locarnini, R. A., Mishonov, A. V., Boyer, T. P., Garcia, H. E., Baranova, O. K., Johnson, D. R., Seidov, D., and Biddle, M.: World Ocean Atlas 2013, Volume 2: Salinity., Tech. rep., S. Levitus, Ed., A. Mishonov Technical Ed.; NOAA Atlas NESDIS 74, 39 pp, 2014.